



UNIVERSITÀ DEGLI STUDI DI TRIESTE
XXXIII CICLO DEL DOTTORATO DI RICERCA IN INGEGNERIA CIVILE
AMBIENTALE E ARCHITETTURA
INTERATENEO CON L'UNIVERSITÀ DEGLI STUDI DI UDINE

STUDY OF STEEL - GLASS FIBRE-REINFORCED POLYMER
(GFRP) BONDED JOINTS FOR THE DESIGN OF ANCHORAGE
SYSTEMS FOR FLAT BOTTOM GFRP TANKS SUBJECTED TO
SEISMIC ACTIONS

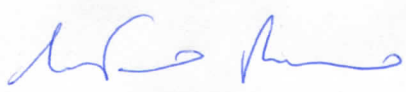
SPECIFIC SUBJECT AREA ICAR/09

Ph.D. student
Guido Tognan


Ph.D. program Coordinator
Prof. Alberto Sdegno


Thesis Supervisor

Prof. Gaetano Russo


Thesis Co-Supervisor

Prof. Margherita Pauletta



ANNO ACCADEMICO 2019-2020

Abstract

In recent years, structural adhesive bonding has gained more interest in industrial and civil engineering. The wide use of combinations of different materials, e.g. steel and Glass-Fibre Reinforced Polymer (GFRP) adhesively bonded joints, is often the only alternative structural technique to welded or bolted joints. The structures of industrial storage tanks involved in situations that require high strength and stability to aggressive fluids make wide use of GFRP. The layout of plants usually needs slender, cylindrical and flat bottom tanks. These tanks need to be anchored at their base to withstand seismic loads. An anchorage system requires to transfer anchor bolts' vertical reactions to the tank wall, through a steel hold-down lug joined to the GFRP tank shell. To date, standard codes provide solutions not involving adhesive bonding. In this research work, we propose a novel technique that uses the adhesive bonding combined with the classic overlay method, to join the steel hold-down lug to the GFRP tank wall. Preliminary, for applying the new procedure to a selected case study, we provide an introduction to the composite material mechanics, then we describe the experimental campaign we performed on two selected adhesives, through tensile, compression and shear bulk testing. Besides, we present the adopted procedure to assemble a double shear lap splice steel-GFRP joints and our modelling strategy regarding the finite element analysis of steel-GFRP joint. After calculated the tensile force to a single anchor bolt for a selected case study, taking into account the hydrodynamic actions induced by the earthquake to the tank, we perform a finite element analysis on a tank wall portion containing an anchorage. The results demonstrate the positive effects of the adhesive applied between the hold-down lug facing the tank shell's surface and the tank wall, in reducing the stresses on the joint's composite part.

Contents

Abstract	iii
Contents	v
List of Figures	ix
List of Tables	xiii
1 Introduction	1
1.1 Background information	1
1.2 The objective of the thesis	5
2 Literature review	7
2.1 Composites	7
2.2 Adhesive bonding	8
2.3 Adhesion phenomena	9
2.4 Adhesively bonded joints	11
2.5 Modelling of adhesively bonded joints	19
2.6 Seismic analysis of liquid-storage tanks	22
3 Basics of glass-fibre reinforced polymer composites	25
3.1 Introduction	25
3.2 Raw materials	26
3.2.1 Glass fibres	26
3.2.2 Polymer resins	28
3.3 Manufacturing methods	28
3.3.1 Hand lay-up	29
3.3.2 Filament winding	30
3.4 Stiffness prediction of GRFP laminates	32

3.4.1	Stress, strain and constitutive equations	32
3.5	Micromechanics of composites	36
3.6	Elastic Constants of a Lamina	39
3.6.1	Coordinate transformation	42
3.6.2	Stiffness and compliance transformations	44
3.7	Analysis of laminated composites	46
3.7.1	Plate kinematics	46
3.7.2	Plate equilibrium	48
3.7.3	Constitutive equation	48
3.8	The Python module <i>cmplampy</i>	52
4	Testing of bulk adhesives	57
4.1	Introduction	57
4.2	Materials and methods	58
4.2.1	Materials	58
4.2.2	Methods and procedures	58
4.2.3	Equipment	66
4.3	Experimental results	71
4.3.1	Tensile test results	71
4.3.2	Compression test results	75
4.3.3	Shear test result	79
4.3.4	Main obtained results	82
4.4	Conclusion	82
5	Testing of Double-shear lap-splice joint	83
5.1	Introduction	83
5.2	Materials and Methods	84
5.2.1	Steel adherends	84
5.2.2	Composite adherends	84
5.2.3	Adhesives and bonding procedure	89
5.3	Test procedure	89
6	Modelling of adhesively bonded joints	91
6.1	Introduction	91
6.2	Modelling strategy	91
6.3	Finite element analysis of the Double-Shear Lap-Splice Joint	93
6.4	Conclusion	98

7	Design overview of a selected case study	99
7.1	Introduction	99
7.2	Case study description	99
7.3	Dynamic response of liquid storage tanks	103
7.3.1	Convective pressure	105
7.3.2	Impulsive rigid pressure	107
7.3.3	Impulsive flexible pressure	108
7.3.4	Base shear and overturning moment	111
7.4	Actions on the anchorage system	113
7.5	The proposed solution	114
7.5.1	Numerical analysis	115
7.6	Conclusion	122
8	Conclusions	125
A	Appendix	129
	Bibliography	133

List of Figures

1.1	Slender fiberglass tank ($H/R = 6$)	2
1.2	Example of plinth-mounted steel tank anchorage [3].	3
1.3	Secondary Bonded Hold-Down Lug as per ASME RTP-1.	4
2.1	Basic loading modes on adhesive joints.	11
2.2	Common configurations of adhesive joints [19].	12
2.3	Geometry of a double-lap joint with gap (not to scale).	13
2.4	Schematic view of failure modes in steel-GFRP bonded joints.	14
2.5	Typical stress-strain curves of adhesives.	15
2.6	Geometry analysed by Volkersen.	20
3.1	Example of glass fibres formats.	27
3.2	Components of a GFRP tank.	29
3.3	Typical head types of tanks.	29
3.4	Schematic diagram of hand lay-up process.	30
3.5	Schematic of basic filament winding process.	31
3.6	Typical helical pattern filament winding process after [60]	32
3.7	Material, (1, 2, 3), and laminate, (x, y, z), reference frame.	40
3.8	Loss on ignition test.	55
4.1	Tensile test specimen dimensions.	59
4.2	Silicone mould of five dog-bone shaped tensile specimens.	61
4.3	ADH1 and ADH2 tensile specimens.	61
4.4	Mould for compression specimens filled with ADH1.	63
4.5	Temperature-time profiles during cross-linking reaction.	64
4.6	ADH1 and ADH2 compression specimens.	65
4.7	Shear test, specimen dimensions.	65
4.8	Parts of gripping system designed for tensile test	67
4.9	Tensile test setup.	68

4.10	Custom made DD1s support, detail of 3D printed part.	68
4.11	Compression test setup.	70
4.12	Prototype of shear fixture.	70
4.13	Shear test setup.	71
4.14	Axial Stress - Axial and Lateral Strain of ADH1 tensile tests.	73
4.15	Axial Stress - Axial and lateral Strain of ADH2 tensile tests.	73
4.16	Tensile test results for the sample TI-3.	74
4.17	Tensile test results for the sample TII-5	74
4.18	Poisson's ratio determination of sample TI-2.	75
4.19	Raw data acquired from compression test.	75
4.20	ADH1 compression tests.	77
4.21	Axial Stress - Axial and Lateral Strain of ADH2 compression tests.	77
4.22	Compression test for the sample CI-4.	78
4.23	Compression test for the sample CII-4.	78
4.24	Poisson's ratio determination of sample CI-3.	79
4.25	Shear test raw data, sample SI-1.	80
4.26	Engineering strain to principal strain.	80
4.27	Shear Stress-Shear Strain and main results for sample SI-1.	81
5.1	Dimensions of Double Lap Shear Joint.	83
5.2	Test specimen panel cut layout.	86
5.3	Tensile tests on composite parts.	86
5.4	Loss on ignition test of composite adherend samples (group B).	87
6.1	Double-shear lap-splice joint.	92
6.2	Model dimensions described by free parameters.	93
6.3	Material fields as assigned in code_aster.	94
6.4	DSLSJ geometry meshed.	95
6.5	Colour map of the displacements magnitude.	96
6.6	Detail of the shear deformation of the adhesive.	96
6.7	Comparison between the finite element model and the Tsai, Oplinger and Morton model.	97
6.8	Lateral view of the color map of σ_{xx}	98
7.1	Number of tanks for each slenderness interval.	101
7.2	Tank reference system in cylindrical coordinates	105
7.3	Pressure distribution of the convective component.	107

7.4	Pressure distribution of the rigid impulsive component. . . .	108
7.5	Pressure distribution of the flexible impulsive component. . .	112
7.6	Pressure flexible impulsive component with different tank slen- derness.	112
7.7	Hold-down bonding procedure.	115
7.8	Mesh for the 3D model.	115
7.9	Boundary conditions applied to the fem model.	116
7.10	Position of paths on adhesive surfaces.	119
7.11	Normalised equivalent stress curve on GTW path.	119
7.12	Normalised equivalent stress curve on SHD path.	120
7.13	Stassi d'Alia equivalent stresses on GTW path.	121
7.14	Stassi d'Alia equivalent stresses on SHD path.	121
7.15	Model A - Von Mises stress values in the overlay (proposed joining technique).	123
7.16	Model B - Von Mises stress values in the overlay (without the application of the adhesive).	123

List of Tables

3.1	Properties of typical E-glass fibre.	26
3.2	Properties of commonly used resins.	28
4.1	Specimens identification	59
4.2	Dimensions measured on the tensile specimens.	62
4.3	Dimensions measured on the compression specimens.	63
4.4	Dimensions measured on the shear specimens.	66
4.5	Adhesives properties obtained from tensile test.	72
4.6	Adhesives properties obtained from compression test.	76
4.7	Adhesives properties obtained from shear test.	81
4.8	Elastic bulk adhesives properties.	82
5.1	Results of tensile test, according to ISO 6892-1:2009.	84
5.2	Average properties of S355J2 steel.	84
5.3	Results of tensile test, according to EN 13121:2016.	87
5.4	Results of loss on ignition test, according to EN 13121:2016.	88
5.5	Average properties of the laminated adherends.	88
6.1	Material parameters for modelling joint's composite adherends	95
7.1	Tanks collected for the case study selection.	100
7.2	Case study tank laminates.	102
7.3	Actions on the anchorages: data for calculations.	114
7.4	Material parameters for modelling steel, adhesive ADH1 and resin.	116
7.5	Material parameters for modelling GFRP tank wall	117
7.6	AHD1 average strength properties.	118

Chapter 1

Introduction

1.1 Background information

Industrial storage tanks can be classified into several types according to their installation, geometric shape, the constituent material, the content they hold, allowable working pressure/temperature, and other factors.

In chemical facilities, tannery factories, wastewater treatment plants, and desalination plants, the typical tank for reagents is cylindrical with the axis oriented perpendicular to the foundation, continuously supported by a flat-bottom and has a hemispherical or dished (torispherical) cover. Where high resistance and stability to aggressive fluids of the container is the essential requirement, the use of Glass-Fibre Reinforced Polymer (GFRP) tanks is strongly recommended and often the only possible solution. GFRP is commonly known as fibreglass.

In most cases tanks are filled, at atmospheric pressure, from about 3 m^3 up to 200 m^3 or more with process water, chemicals or other types of hazardous fluids. The chemical process and the layout of plants usually require slender containers. For most of these tanks the ratio of the height of liquid, H , in the tank, and the tank radius, R , is greater than three (Figure 1.1). Therefore to withstand horizontal actions, like those induced by e.g. earthquakes, tanks need to be anchored at their base. In a tank farm one or more storage tanks are generally placed above-ground inside containment basins in order to contain spills for certain percentage of the entire content in case of tanks damage. Chemical spills or leaks may lead to serious property damage and environmental contamination of streams, soil and groundwater water, posing threats to human health. Nowadays the issue of chemical



Figure 1.1: Slender fiberglass tank ($H/R = 6$), filled with 100 m^3 of Hydrochloric Acid 33% solution.

releases caused by natural hazard events has become a great concern. In [1] the World Health Organization provides brief information on the mechanisms of chemical release resulting from earthquakes and the subsequent health impacts. In [2] Casson et al. have analysed and discussed a data-set of 438 records queried from three database specialized in industrial accidents using keywords like earthquake, flood, rainstorm etc.. The analysis shows that, despite earthquakes are only the 6% of the share, they have the hugest economic impact in NaTech (Natural Hazard Triggering Technological Disasters) events.

The main failures that are responsible for a large or total loss of the liquids contained in these storage tanks are rupture of pipelines and connection flanges caused by large base uplifts or horizontal movements out of the position, collapse of the shell-base connection and the penetration of the tank bottom or wall with anchor bolts. Therefore the proper anchorage design represents the crucial problem for satisfying safety and economic requirements of the whole storage structure.

There are many codes, e.g. those published by the European Committee

For Standardization, the American Society Of Mechanical Engineers, the American Petroleum Institute, the New Zealand Society for Earthquake Engineering and a wide literature covering the design of steel storage tanks and their anchorage system (hold-down lugs). Steel tanks hold-down lugs are usually welded or bolted directly to the shell wall (Figure 1.2).



Figure 1.2: Example of plinth-mounted steel tank anchorage [3].

Regarding GFRP tanks, clearly, GFRP of the tank wall and steel of the anchorage apparatus are not, in a strict sense, weldable. Design codes dealing with GFRP tanks, conversely, are only two: EN 13121-3:2016, *GRP tanks and vessels for use above ground - Part 3: Design and workmanship*, and ASME RTP-1:2019, *Reinforced Thermoset Plastic Corrosion Resistant Equipment*. The former suggests two sketches of a typical anchorage arrangement with no design procedures and specifies that the proposed anchors are not suitable for seismic loads unless friction load can be considered. It is worth noting that the evaluation of the coefficient of friction results in great uncertainty [4]. Besides, it is not acceptable to credit friction for a portion of the shear capacity and provide the remainder by anchor bolts. Therefore this anchorage arrangement is not suitable for use on tanks subjected to seismic actions. ASME RTP-1 in the Non-Mandatory Appendix NM-4 presents typical geometries and simple design procedures for two kinds of hold-down lugs. The proposed steel hold-down lugs are attached by hoop winding or

secondary bonding on the tank wall. These joining techniques are based on applying fibreglass overlays to assemble the anchorage apparatus to the tank wall. Hoop winding applies continuous glass fibres wound to the tank wall using a filament winding machine, secondary bonding uses hand lay-up impregnated fabric overlays instead. Regarding the secondary bonding, Figure 1.3 depicts the hold-down lug components on the right-hand side, and the left-hand side shows the hold-down lug overlaid with the fibreglass.

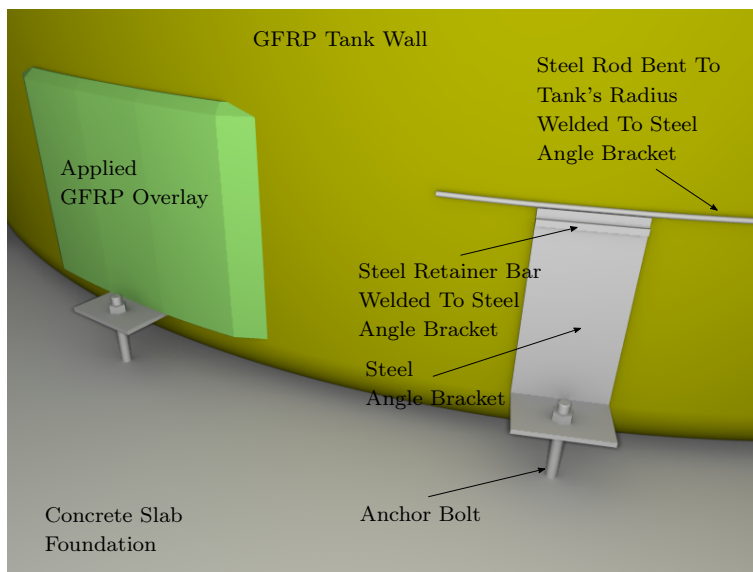


Figure 1.3: Secondary Bonded Hold-Down Lug as per ASME RTP-1.

However, these hold-down lugs are not suitable for resisting strong seismic actions because, generally, flat tank bottoms are not sufficiently stiff to permit the weight of the tank's liquid contents to balance the overturning moment even partially. Therefore the anchorage apparatus shall be designed for the total base moment, and high tensile loads have to be transferred from the anchor bolts to the tank wall.

Concerning other scientific publications on the subject discussed in this research, a recent literature survey using Elsevier's Scopus with the keywords *GFRP tank anchoring*, *GFRP tank hold-down lug*, *tank adhesively bonded anchorage*, *adhesively bonded hold-down* did not give any result. No references to other publications on the topic were found.

Going back to Appendix NM-4 of ASME RTP-1, the design procedure neglects the possible contribution in transferring hold-down to anchor-bolts

tensile loads that may be obtained with a bonded joint between the steel angle bracket's surface facing the tank wall and the tank wall itself. In the author's opinion, if the back surface of hold-down lugs is correctly bonded to the tank wall and the front surface overlaid with fibreglass, when strong forces need to be transferred from the tank wall to anchors, the so modified joint could improve the mechanical strength of the whole anchorage system. Therefore, to assess this improvement, it is necessary to investigate the materials involved, correctly define the seismic loads, select the right adhesive and evaluate its efficiency. On these bases, it will be possible to develop a numerical model for the hold-down lug.

It is worth noting that, not to make things too much complicated, this study relates to the short-term structural behaviour of the bond between steel and GFRP. Moreover, the investigation does not consider the long-term behaviour and environmental impact on joints performance and defer these topics to future work.

1.2 The objective of the thesis

To the author's knowledge, there have been no previous attempts to improve the joining technique between the steel hold-down lugs and the GFRP tank walls with systems that involve adhesives. This research proposes a novel technique for assembling the steel hold-down lugs on GFRP tanks walls and suggests a design method. It aims to better understand the behaviour of surface-mounted steel hold-down lug on GFRP tanks, improved adding a layer of adhesive. Addressing this topic, the research has involved several preliminary studies on the Glass-Fibre Reinforced Polymer composites fundamentals, the manufacturing method for GFRP tanks, the adhesives, the adhesively bonded joints, and the seismic analysis of liquid storage tanks.

The following objectives were defined and pursued under this research program:

- to experimentally measure the mechanical properties of two selected adhesives;
- to conduct tests for the mechanical characterization of the steel-GFRP joints made using the selected adhesives;
- to develop a numerical model of the steel-GFRP tested joints;

- to compute the actions on the anchorage due to seismic load for the liquid storage tanks;
- to apply obtained results to design the improved hold-down lug.

The entire experimental campaign described herein has been conducted at the Laboratory for Testing of Materials and Structures of the Polytechnic Department of Engineering and Architecture, University of Udine, Italy.

Chapter 2

Literature review

Since there is no related work on designing the anchorage system involving GFRP tanks, the subjects that supported the research objective are reviewed in this chapter. First, the general references to long fibre glass-polymer composites material the author followed in his work are presented. Secondly, supported by some references, adhesive, adherend and adhesion terms, are introduced. Thirdly a brief review of Baldan paper [5] that, based on extensive literature, explains adhesion phenomena' main topics is given. Next, many references concerning adhesively bonded joints and their analytical modelling are reviewed. Finally, the main works on the seismic analysis of liquid-storage tanks are shortly reviewed.

2.1 Composites

Composites are related to this research because the structure of tanks is made of Glass-Fibre Reinforced Polymer, and the joining technique involves even GFRP overlays to steel components of the hold-down lug. Although the underlying concepts of composite materials go back to ancient time, the technology was essentially developed, and most of the progress occurred, in the last four decades. Moreover, there is a considerable amount of literature on this topic. This section presents a very briefly review of references that concern the fundamental aspects of composites.

In [6] a traditional approach based on mechanical behaviour of compos-

ites described by the linear theory of elasticity can be found. The two books [7], and [8], selected for the study, presents an integrated coverage of the field of composite materials, including the current status of composites technology, properties of constituents, micro and macro mechanics aspects, and the Classical Lamination Theory (CLT). Regarding the design of the tanks structures, Eckold explained a detailed analysis of laminates as used in the manufacture of composite pipework, tanks and vessels, using the anisotropic elastic theory, in [9]. Eckold presented the procedures practised, at the time of writing, in the UK and described in the design code BS4994:1973, Vessels and tanks in reinforced plastics. Furthermore, he proposed a design method for filament wound composites that considers the relatively high shear stresses generated within the individual laminae from the application of relatively simple load systems.

Furthermore, composite materials present the most significant challenge to experimental characterization. In [10], a comprehensive guide to processing techniques, specimen preparation, test method analysis, test procedures and data reduction schemes can be found to determine mechanical properties and strength of composite materials. Regarding the selection of strain-gauges for surface strain measurements on composites, is not generally more difficult than for other materials. However, Slaminko [11] indicates many aspects to consider for selecting the strain gauges to be applied on composite and polymer-like materials. The choice of gage length and width must consider both the surface texture and the material's non-homogeneity. Since composites, like plastic, are a poor thermal conductor, even the gauge power-density plays an important role. Acceptable power-density for strain gages on composites is generally in the range of 0.31 kW m^{-2} to 1.20 kW m^{-2} . Using 3 mm or larger strain gauges having a grid resistance of 350Ω and working with an excitation level of 3 V or less, the power-density falls within this range.

2.2 Adhesive bonding

Adhesives have a long history. Starting from prehistorical age, man exploited bonding technology in joining materials together, even of different nature, to produce useful items (e.g., to glue the stone arrow heads to a wood shaft, birch-bark-tar were used [12]). After thousands years, in Egypt, adhesives were first mentioned [13] and the occupation of adhesive-maker was born. Since that period until a hundred years ago, almost all of adhesives

were from natural products such as bones, skins, fish, milk, and plants. In the early years of the twentieth century, adhesives based on synthetic polymers were developed. However, these first adhesives were of limited use, since they were expensive and had poor mechanical properties. Since 1940, as the chemical knowledge of polymers has started to grow rapidly, the mechanical performance, in terms of strength and ductility, and the cost reduction of adhesives have had an important improvement [14]. Aerospace industry was one of the first sectors especially involved in the use of bonding method. In the forties, together with polymer based adhesives, fibre-reinforced polymers (FRP) have been developed greatly since they were first introduced. Adhesively bonded systems in combination with FRP became more and more presents for various purposes in industries such as automotive, aeronautics, ship-building, electronics, construction, biomedical, etc..

It is convenient now to define an *adhesive* as a polymeric material which, when applied to surfaces, can join them together and resist separation [15]. When an adhesive is employed in primary load-bearing applications and provides for the major strength and stiffness of the structure, it is defined as *structural adhesive* [16]. The materials being joined together by the adhesive, are commonly referred as the *substrates* or *adherends*. The term *adhesion* is used when referring to the attraction between the adhesive and adherend [17]. Therefore, adhesion forces that develop between adhesive and substrate will hold the materials together.

2.3 Adhesion phenomena

Adhesion phenomena are a very complex issue and require a multidisciplinary knowledge of many subjects relate but not limited to polymer and surface chemistry, mechanics of materials, fracture mechanics and rheology. Fundamental concepts such as interfaces of similar and dissimilar materials, adhesion mechanism, surface free energy and wettability can be also found in Baldan [5]. The *interface* is the boundary between adherend and adhesive. The *interphase*, that may be formed when two homogeneous solids brought in contact with each other, is a region with finite volume and distinct physical properties or gradient in properties.

In [5] six adhesion theories that have been proposed by other researchers starting from the earliest introduced are summarized. Those most closely related to the present work are the mechanical interlocking model, the adsorp-

tion theory, the model of weak boundary layer and the chemical or molecular bonding theory.

The *mechanical interlocking model*, that is not a mechanism at the molecular level but a physical phenomenon, concerns with the irregularities of the adherend surface. Therefore roughness, porosity and irregularities of the surface are the main factors affecting the mechanical interlocking. However the modification of the surface is effective only under a sufficient wettability of the surface itself. The wetting concept is briefly explained hereafter. The *adsorption* involves interatomic and intermolecular forces between adhesive and substrate (adherend). These forces include, ordered by increasing strength, primary bonds, donor-acceptor interactions and secondary bonds. Primary bonds occurs through three mechanisms, covalent, ionic and metallic. In donor-acceptor interaction the formation of a bond take place e.g. with the transfer of a lone pair of electrons from the donor to the acceptor. Secondary bonds involve van der Waals forces and hydrogen bonds.

The *weak boundary layer theory* states that the failure occurs due to the formation of a weak boundary layer different from the interface between adhesive and substrate. Baldan reported also the Bikerman's classification of weak boundary layers when caused by air pores, impurities at the interface and reactions between components and substrate.

The *chemical bonding theory* involves a molecular bonding across the adhesive-substrate interface. Chemical bonds can greatly improve the adhesion even between dissimilar materials. The better the adhesion, the greater the mechanical strength of a joint. Therefore *coupling agents* based on silane molecules are often used in substrate surface pretreatments as adhesion promoters. Coupling agents acts at both the adhesive and the substrate. The afore-mentioned concepts that complete this briefly review on adhesion phenomena are the surface free energy and the wetting. The surface free energy can be considered as the surface tension of a solid, it is the work that would be necessary to increase the surface area of a solid phase. This work results from the attraction of the bulk material for the surface layer that reduces the number of molecules in the surface region increasing the intermolecular distances. The attraction originates because the forces on the surface molecule are unbalanced than those in the bulk solid. Back to normal configuration the work done will be returned. The excess energy associated with presence of the surface is the surface free energy.

Wetting of liquid on a solid surface is obtained when a physical interaction

develops between the two surfaces' atoms. The wettability is related to the surface free energy of the adhesive and the adherend. An adhesive with a surface free energy less than that of the adherend will spread over the substrate and readily wet the surface and form good bonds.

2.4 Adhesively bonded joints

An *adhesively-bonded joint* may be defined as a system in which two similar or dissimilar surfaces of materials hold together by means of an adhesive. Adhesively bonded joints are increasing alternatives to the traditionally adopted mechanical joints, i.e. bolted, in engineering applications, particularly with FRP adherends. The traditional joint methods usually result in the cutting of fibres, and hence the introduction of stress concentrations, both of which reduce structural integrity [18]. In Figure 2.1 the basic loading modes experienced by adhesive joints are shown. Designing joints with adhesives consists in a large part in arranging that stresses are resisted in shear rather than by direct tension, cleavage or peeling [15].

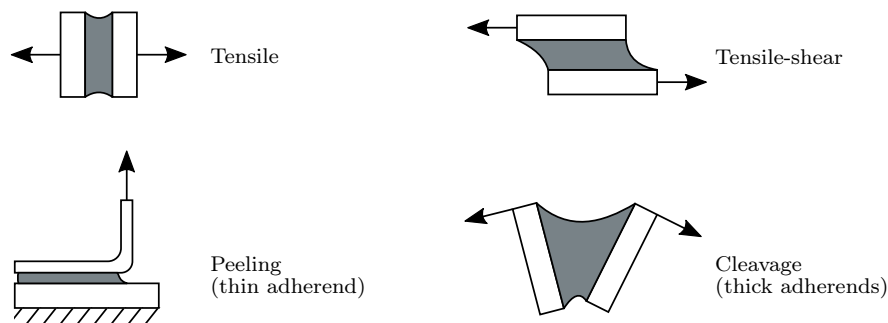


Figure 2.1: Basic loading modes on adhesive joints.

The most common joint types are Single-Lap Joints (SLJ), Double-Lap Joints (DLJ), butt-strap joints, Double Butt-Strap Joints (DBSJ), butt joints and scarf joints (Figure 2.2). These configurations are used for test purposes rather than featuring explicitly in actual constructions. However they allow to replicate quite well the actual mechanical behaviour of joints employed in the actual structures. Due to its ease fabrication process, the SLJ is the most studied joint configuration and it is used for comparison as well as quality control of adhesives. The SLJ experiences high peel loading at the ends of the overlap in addition to shear loading and puts the adhesive in a

complicated state of stress. Therefore, it is not suitable for the determination of the true adhesive properties.

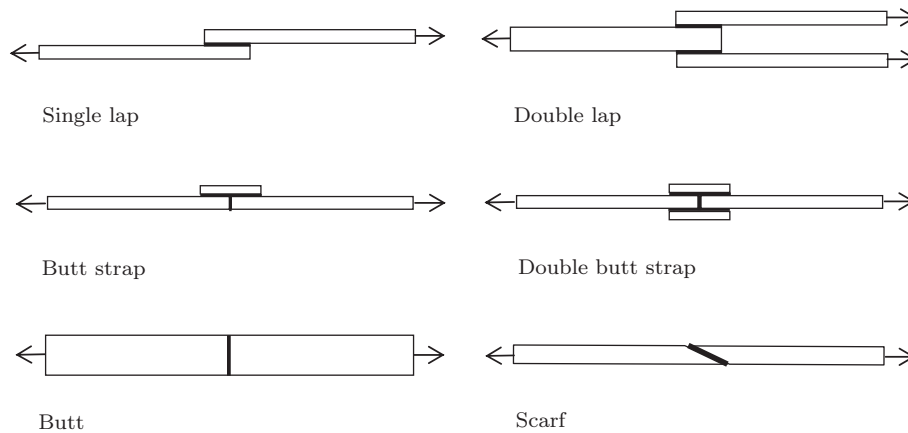


Figure 2.2: Common configurations of adhesive joints [19].

Adhesively-bonded joints have been widely used not only to join FRP structural components but also to hold together FRP and metal, wood etc. From the standpoint of civil engineering, after the pioneering work of Professor U. Meier in the late eighties, an extensive research on strengthening concrete structures with bonded FRP plates has been conducted. In [20] Teng et al. provided a comprehensive state-of-the-art summary on this topic. Pham and Al-Mahaidi [21] presented a background on FRP-concrete bond, pointing up to the most common test set-up methods and to the failure modes in shear-lap tests reported in literature. Chen and Teng [22] highlighted that a key issue in the design of retrofitting solutions using external bonded plates is the end anchorage strength. They provided a new model for practical applications in the design of FRP-concrete as well as steel to concrete bonded joints.

Over the past twenty years, the use of FRP to repair or upgrade steel structures has become an attractive solution and has received much research interest. Because of superior tensile properties of carbon fibres compared to glass fibres much more studies have been done on strengthening steel structures with bonded plates of carbon fibre-reinforced polymer, that is on CFRP-to-steel bond, than on GFRP-to-steel bond. Ramin et al. [23] reported that there appears to be much less research on GFRP-to-steel bond as compared with CFRP-to-steel. Part of the present work involves the study of adhesively bonded joints between steel and glass fibre-reinforced polymers.

Therefore existing investigations on the behaviour of CFRP-to-steel bonded joints are also reviewed considering the common concepts between these joints and GFRP-to-steel bonded joints.

Summaries of experimental test configurations used to characterise the bonded FRP-to-steel joints can be found in [24, 25]. Zhao et al. [24] reported a categorization of joints based on where the loads are applied, Type 1: load indirectly applied to FRP and steel plate in a beam, Type 2: load directly applied to steel element without gap, Type 3: load directly applied to steel element with gap and Type 4: load applied directly to FRP. Type 3 in the variant named i) was a double-strap joint in which a small gap was left between the two adjacent unloaded ends of the steel adherends and two FRP straps, as wide as steel, was bonded to steel. Yang et al. in [25] collected further test configurations of joints and presented the results of finite element simulations of the interfacial stresses of several FRP-to-steel joint configurations considered by different researchers.

Due to the double-shear plane arrangement, double-strap and double-lap joints have been also considered by other researchers in experimental as well as in numerical studies e.g., [26, 27, 28, 23, 29]. Figure 2.3 shows a double-lap joint with a gap and details the currently terms applied for adhesive joints; t_o , t_i and t_a are the thicknesses of outer adherends (or straps), inner adherends and adhesive, respectively, L is the overlap length; spew fillets are not represented, the spew fillet is the excess of adhesive squeezed out of the lap region at the moment of the joint manufacture.

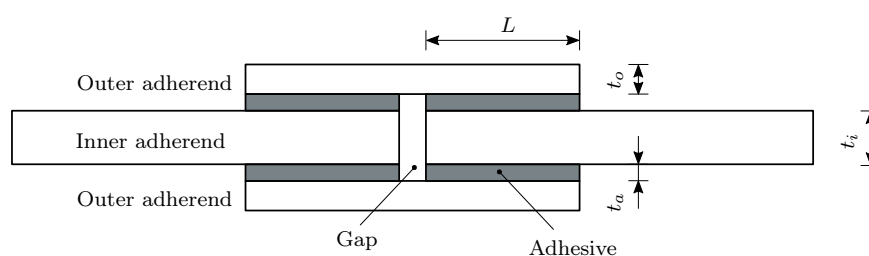


Figure 2.3: Geometry of a double-lap joint with gap (not to scale).

The failures analysis in testing adhesive bonded joints is based on the failure mode identification. Considering the adhesive bonded joints composed of homogenous adherends e.g., steel, alluminum etc., there are three basic ways in which they may fail: (a) in one of the adherends outside the joint, (b) by fracture of the adhesive layer (*cohesive failure*), (c) interfacially between the

adhesive and the adherend (*adhesive failure*). In FRP composite adhesive joints, according to the standard ASTM D5573, *Standard practice for classifying failure modes in fiber-reinforced-plastic (FRP) joints*, there are seven typical characterized modes of failure, (a) adhesive failure, (b) cohesive failure, (c) thin-layer cohesive failure, (d) fibre-tear failure, (e) light-fibre-tear failure, (f) stock-break failure, or (g) mixed failure. Regarding steel to GFRP bonded systems subjected to a tensile force, a schematic view of possible failure modes is shown in Figure 2.4, where dark grey rectangles highlight the adhesive layers.

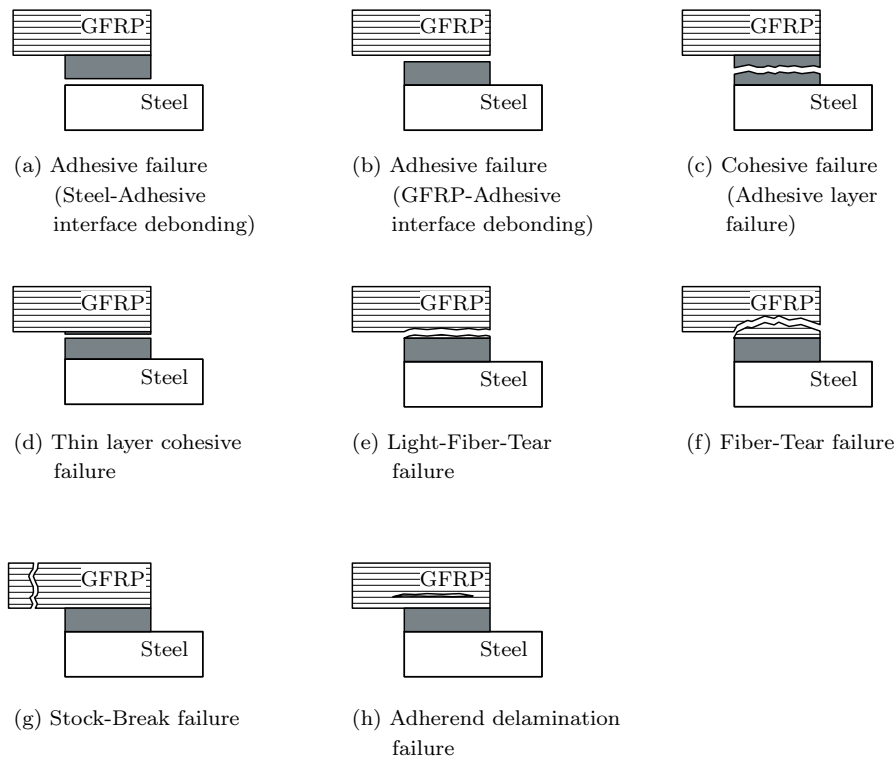


Figure 2.4: Schematic view of failure modes in steel-GFRP bonded joints.

There are a wide range of structural adhesives available in the marketplace which can be used to bond FRP to metallic substrates and these include epoxies, vinyl esters, polyurethanes, acrylics and cyanoacrylates. Adhesive selection involves the consideration of the following parameters: strength range, type of stress on adhesive, geometry and joint surface dimensions, interfaces condition, curing time and temperature and finally service temperature and humidity. Hence, finding an appropriate interfacial adhesive

with desired adhesion strength to bond the GFRP on a steel substrate is considered to be a challenging task [30]. It should be noted that adhesives that normally require curing at ambient temperature are best suited to in-situ applications. Epoxies have high strength and temperature resistance, vinyl esters cure rapidly at room temperature, such as a polyester, but exhibit adhesion and chemical resistance properties that are more representative of an epoxy, polyurethanes are resistant to fatigue and have good flexibility at low temperatures, acrylics have capabilities of fast curing and tolerate dirtier and less prepared surfaces, cyanoacrylates cure very fast but have poor resistance to moisture and temperature. Typical stress-strain curves of adhesives are shown in Figure 2.5, where the solid line, the dashed line and the dash-dotted line represent qualitatively, brittle, intermediate and ductile adhesives, respectively.

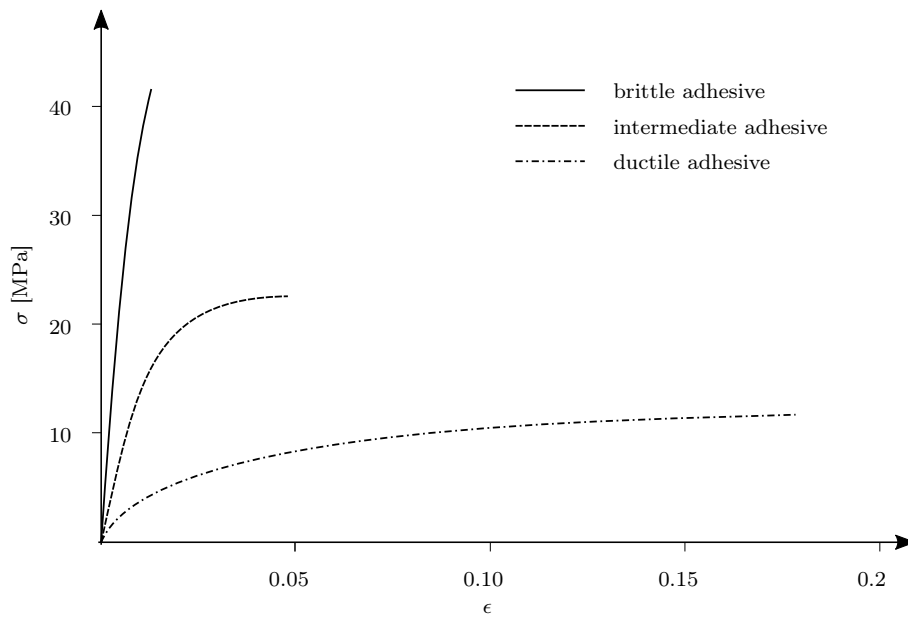


Figure 2.5: Typical stress-strain curves of adhesives.

When the adhesive has been chosen, the main parameters affecting the performance of the adhesively bonded joint are surface preparation of the adherends, mechanical properties of the adherend, adhesive thickness and overlap length.

Surface preparation is one of the most important and critical steps in the bonding technique. Careful selection of the surface preparation method with respect to the substrate material is needed as some methods may degrade

their properties [31]. Surface pretreatment increases the bond strength by altering the substrate surface in a number of ways including: (a) increasing surface tension, (b) increasing surface roughness or (c) changing surface chemistry [16]. The present work focuses on short-term joint strength under dry conditions. The positive effects that could be expected of chemical pretreatments on bonded joints under wet conditions may therefore not be encountered.

Hollaway and Cadei [32] outlined that surfaces to be bonded must be: (a) free from contamination, (b) sufficiently chemically active to enable the formation of chemical bonds between the adhesive and the adherends, and (c) resistant to environmental deterioration in service, especially due to hydration. The authors suggest three basic steps of surface pretreatment for metallic adherends, the removal of surface contamination by degreasing, grit blasting (sandblasting) and dry-wipe removing of sanding debris. For composite adherends when they do not contain a peel-ply¹ the procedure would be to abrade the bond-side of the plate with a medium sandpaper or a sand blaster, and to wipe clean with a dry cloth to remove any residue, and finally to wipe with acetone. It is worthwhile noting that surface preparation is especially important for secondary bonding to composites. Surfaces of composite materials have a high variability of texture, but they need to be prepared for bonding. The abrasion procedure on GFRP, when adopted, should just remove the surface of the resin without exposing fibres [18]. Pretreatment of steel surfaces with grit blasting and cleansing with solvent or alkaline solutions have been adopted by several researchers, [33, 34, 35, 36]. The main purpose of the treatment of the steel along the bond area is to remove dust, paint, oil and any other suspended materials on the surfaces and to ensure good contact between the FRP and steel along the bond area. In [37] Melograna and Grenestedt investigated the adhesion of stainless steel to vinyl ester composite. They suggest, for the stainless steel plates, a basic surface preparation that consisted of grit blasting (mixture of 40-70 grit), followed by solvent cleansing (using trichlorethylene, acetone, or Poly Fiber C2200). A more detailed explanation of tools and chemicals used in surface preparation is presented by Osouli-Bostanabad et. al [30]. The authors studied the influence of pre-bond surface pretreatment for steel pipes that need to

¹The peel-ply, namely tear ply, is a sacrificial layer of glass fibre and polymer material, which is placed on the surface during the laminating process; the removal of the peel ply can produce a clean and fresh surface with the required roughness.

be repaired using glass fibres reinforced epoxy patches, a novel maintenance and repairing damaged section trend for fluid transportation pipes. Steel surfaces of specimens (single lap splice SLS, and T-peel) were abraded using the Silicon Carbide (SiC) paper with different grit sizes up to 100, 220, 500 and polish according to ASTM D2651-90 standard. After that surfaces were precisely cleaned with demineralized water. Two different degreasing cleaner products were employed on the steel substrate to investigate the effect of the cleaner solution over the final adhesion strength. The former was an alkaline based solution (commercial Finish) and the latter was the solvent acetone. Glass fibre epoxy based composite was abraded by a set of emery papers and finally cleaned with acetone. Results revealed that the adhesion strength of samples pretreated with Finish was higher than those cleaned with the acetone. Furthermore hydrostatic tests were performed to validate the results of SLS and T-peel tests. The hydrostatic tests confirmed the improved performance of pipes fixed with patches applied after Finish cleaning. Wei et al. [38] polished CFRP adherends with abrasive paper of grit size up to 1000 and applied acetone to eliminate impurity of the substrate surfaces.

Many researchers have observed that the nature and mechanical properties of adherends strongly affects the joint performance. With steel to FRP joints the layered nature of composite adherend makes the failure mechanism more complex as shown earlier in Figure 2.4. Retrofitting procedures for strengthening steel structures adopt bonded FRP plates or non-impregnated fibres directly laid-up to steel members on site [39, 40]. Hence many studies have been involved with this type of adherends. The pultruded plates or the sheets in general consist of a given number of unidirectional layers. Therefore they are highly orthotropic. In [34] the experimental results on the behaviour of CFRP-to-steel bonded interfaces through the testing of a series of single-lap bonded joints showed that as CFRP adherend rigidity increases, the failure mode is likely to change from cohesion failure to the interlaminar failure of CFRP. Taib et al. [41] investigated experimentally the effect of fibre orientation on the failure load and the associated failure mode. They studied a GFRP-GFRP joints bonded with an epoxy adhesive and two types of adherend were considered. The first was manufactured by stacking six plies of glass fibre satin weave oriented in warp direction. The resulting laminate is termed as $[(0/90)]_6$. In the second one the fabric plies were rotated 45° obtaining a $[(45/-45)]_6$ laminate. The test results revealed that the stiffness of the joint with the $[0/90^\circ]$ laminate adherends is higher

than of the $[\pm 45^\circ]$ and this high stiffness seems to promote a higher failure load. The whole of $[\pm 45^\circ]$ laminates joint specimens exhibit an interfacial failure. The authors explained this behaviour by the fact that the more ductile $[\pm 45^\circ]$ adherends allow more deformation. As mentioned before there are several studies that have investigated steel-FRP bonded joints in which GFRP or CFRP adherends are unidirectional laminates. Few researchers have addressed the issue of effects of different type of laminates. The need for further investigations on GFRP to steel bonded joint has been confirmed by Rameshni et al. [23] that reported what Cadei et al. highlighted in [42]: the behaviour of GFRP bonded joints cannot be simply extrapolated from that of CFRP joints, because it is known that the strength and stiffness of the FRP have a profound effect on the joint capacity, and these characteristics are different from those of GFRP.

Adhesive thickness influences initial stiffness of joint, mode of failure and joint strength. Vallée et al. [43] studied double lap joints composed of pultruded GFRP profiles with relatively thick adhesive layers, typically used in infrastructure applications. They investigated the influence on joint strength of a variation in the adhesive layer thickness from 5 mm to 35 mm in steps of 5 mm. The analysis showed that joint strength decreased non-linearly with increasing adhesive layer thicknesses and the gradient of the strength reduction decreased with increasing adhesive layer thicknesses. Xia and Teng [34] investigated the influence of bondline thickness on the debonding failure mode using a pull-off test specimens with load applied directly on a pultruded CFRP plate bonded to a steel member with an epoxy adhesive. They observed that when an adhesive layer of realistic thickness (< 2 mm) is used, debonding is likely to occur within the adhesive layer with a ductile failure process, but when a thick adhesive layer is used, debonding is likely to occur by FRP delamination. In [44] Yu et al. analysed the effect of adhesive thickness of two selected adhesives. Three adhesive thicknesses (i.e. 1.5 mm, 2 mm, 3 mm) were adopted. Results show that, within the practical thickness range of 1 mm to 2 mm, a thicker adhesive layer appears to increase the bond strength of the joint in the cohesion failure mode and the authors concluded that more tests is needed to thoroughly clarify such effect. Recently, Sugiman et al. [45] presented a study focused on the effect of adhesive thickness on the strength of steel-composite joints aged in wet environment. The authors performed the tests using low carbon steel-GFRP single lap joints specimens. The thickness of an epoxy based adhesive layer

was varied in the range 0.1 mm to 0.5 mm with a step of 0.1 mm. They reported that in dry condition the joint strength tended to increase with the increase of adhesive thickness. An opposite trend was observed by da Silva et al. [35]. These authors studied the effect of bondline thickness for three adhesives (very ductile, very brittle, intermediate) on the bond strength of single-lap joints. The results showed that the lap shear strength increases at the decrease of adhesive thickness .

The overlap length influences the stress distribution and, therefore, the adhesive joint's strength. In [33] Jiao and Zhao, studying the CFRP strengthened butt-welded very high strength (VHS) circular steel tubes, found a similar phenomenon that Chen and Teng [22] highlighted for the bond strength between CFRP and Concrete. They observed that the joint strength cannot always increase with increased bond length, beyond the *effective bond length*. The experimental results of Yu et al. in [44] confirmed the existence of an effective bond length. Al-Mosawe et al. [29] investigated the impact of CFRP properties on the effective bond length of the CFRP-steel double-strap joint specimens, numerically and experimentally. They obtained the same effective bond length value for both experimental and analytical tests.

2.5 Modelling of adhesively bonded joints

The single-lap joint (SLJ), Figure 2.2, is one of the most common joints found in practice. In modelling the adhesive-bonded joint, the most straightforward analytical approach assumes that the substrates (adherends) are virtually rigid and the adhesive deforms only in shear. Therefore, the load transfers from one substrate to another substrate by constant shear stress in the adhesive. This shear stress, τ , constant over the overlap length, l , is given by:

$$\tau = \frac{P}{bl}$$

where P is the applied load and b is the joint width. The shear stress value can be considered the average shear stress that is acting on the adhesive layer. Many simplifications affect this approach; however, it is still the basis for assessing the adhesive shear strength in many test situations proposed by codes and standards. Nevertheless, the apparent simple single lap joint gives rise to quite complicated adhesive stress. In 1938, Volkersen [46] first introduced the concept of differential shear and proposed a simple shear lag

model for the SLJ adhesively bonded joints. This model, shown in Figure 2.6, assumes that the elastic and isotropic adherends are in tension and the adhesive is subjected to shear only, and both stresses are constant across the thickness.

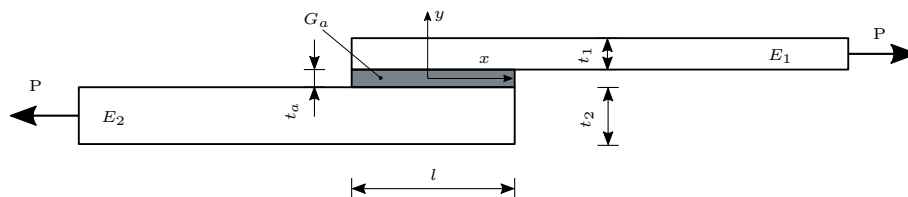


Figure 2.6: Geometry analysed by Volkersen.

The equation for the shear stress obtained with the Volkersen assumptions and different Young's modulus for adherends gives:

$$\tau(\xi) = \frac{P}{bl} \left(\frac{\omega \cosh \omega \xi}{2 \sinh \frac{\omega l}{2}} + \frac{w}{2} \left(\frac{E_2 t_2 - E_1 t_1}{E_1 t_1 + E_2 t_2} \right) \frac{\sinh \omega \xi}{\cosh \frac{\omega l}{2}} \right) \quad (2.1)$$

where $\xi = x/l$ with $-1/2 \leq \xi \leq 1/2$ and

$$\omega = \sqrt{\frac{G_a}{t_a} \frac{E_1 t_1 + E_2 t_2}{E_1 t_1 \cdot E_2 t_2}} \quad (2.2)$$

However, this analytical model has limitations. It does not consider the bending moments induced by the applied load's eccentricity, nor the adherend shearing, and it predicts the maximum shear stress to occur at the free surface at the end of the joint overlap. Regarding the bending moment, the model of Volkersen, applied to a quarter of double lap joint gives a solution closer to the actual behaviour because the bending of the adherends is not as significant as in the SLJ. Concerning the adherend shearing, when laminated composite adherends are present, the shear, and normal deformation should be considered. Indeed, with adherends with relatively low transverse shear and normal moduli, as it is the case with laminated composite adherends, the shear and normal stresses will cause large transverse shear and normal deformations in the adherends, close to the interfaces. At the free surface of the joint overlap, the shear stress should be, in practice, zero. In addition, analyses that ignore the stress-free condition overestimate the stress at the ends of the overlap and tend to give conservative failure

load predictions, [47]. After Volkersen, many authors proposed further analytical models of increasing complexity. Da Silva et al. in [48] and in [49] presented a comprehensive literature survey on closed form methods and comparative study of the principal ones, respectively. Table 1 of [48] reports a summary of both linear and nonlinear two-dimensional analytical models available in the literature. The comparative study presents three classes of analytical models, elastic, nonlinear adhesive, and nonlinear adhesive and adherends. In [50], the authors improved theoretical solutions for adhesively bonded single- and double-lap joints. They considered the adherend shear deformations assuming a linear shear stress distribution through the thickness of the adherends. Furthermore, they validated the analytical solution with experimental results and numerical solutions. Especially for the adherends with relatively low transverse shear stiffness (for example, in the case of laminated composite adherends), the proposed theoretical solutions provide a better prediction than the classical solutions. A later investigation by Tsai and Morton [51], showed that with unidirectional ($[0]_{16}$) and quasi-isotropic ($[0/90/-45/45]_{2S}$) composite adherends under tensile loading, the results obtained with the improved model formulated in [50], are in good agreement with experimental results. Generally, even for simple geometries, analytical techniques become highly involved in the presence of composite adherends. Due to composites anisotropic nature, the adherend constitutive model is more complicated, and the obtained equations require a numerical solution. However, numerical solutions derived from FEMs are preferable.

In the literature several methodologies for the finite element analysis can be found. In [39], Youssef et al. adopted the finite element, using three-dimensional brick elements, to describe the profile of stresses and strains that develop in the rehabilitated steel beam with GFRP sheets. The comparison between the experimental and finite element results showed excellent agreement that validated the developed tools. Speth et al. [28] investigated a double lap-shear joint involved in the design and certification of the adhesively-bonded composite to steel joints for the marine industry. Using FEA models, a careful analysis of the joint performance proved his minimum safety factor. In [23] Rameshni et al. studied the adhesive bond between glass fibre-reinforced polymer (GFRP) and steel both experimentally and using finite element analysis. They developed a three-dimensional, nonlinear model for the double-shear lap-splice tested specimens. The comparison between the predicted and experimentally measured strain at the surface of the

GFRP along the longitudinal axis of the double-shear lap specimens validated the model. Recently, Jiang et al. in [52] presented an experimental study and numerical analysis on the mechanical behaviour of the adhesively-bonded joint between FRP sandwich bridge deck and steel girder. The linear-elastic finite elements analysis involved the specimen as well as the whole experimental apparatus. The stress states obtained on the FRP laminate interface and the adhesive layer under six loading angles, using Finite Element modelling method, indicated the crack initiation location and the failure mode for the tested adhesive joints.

2.6 Seismic analysis of liquid-storage tanks

The analysis and design of liquid storage tanks subjected to earthquake-induced actions have been the subject of numerous analytical, numerical, and experimental works. Housner, in a pioneering work [53], presented a solution for the hydrodynamic effects in non-deformable vertical cylindrical and rectangular liquid containers. The seismically induced loads, with this method, for the first time, are split in the impulsive component (due to rigid body movement of the tank and the fluid) and the convective component (due to sloshing oscillation of the fluid). The base shear and overturning moment are calculated with these load components. However, assuming the tank as rigid, the proposed method completely neglects the fluid-structure influence and does not permit the calculation of stresses in the shell. Nevertheless, this model constitutes the basis for the American Petroleum Institute standard provisions for vertical cylindrical tanks, [54]. Numerous analyses of damage caused by earthquakes have shown that tank dimensioning using the Housner method does provide a conservative estimate of the dynamically activated loads, especially for slender tanks with flexible walls (e.g. slender steel tanks). Veletsos and Yang [55], through elaboration on the fluid dynamics of an incompressible inviscid liquid, have extended the Housner's formulation. This approach has been developed to the case of a flexible tank by Haroun [56]. Veletsos and Yang and Haroun's contributions formed the basis for the seismic design provisions concerning vertical cylindrical tanks reported in the European Standard Code, Eurocode 8. For the calculation of flexible tanks, the Eurocode 8 suggest the added-mass method. The results obtained with this method are quite accurate, as well as the method is pretty complicated. It requires a coupling of complex mathematical software

with a finite element program, indeed. Meskouris et al. in [57] proposed an equivalent method, based on tabulated coefficients.

Chapter 3

Basics of glass-fibre reinforced polymer composites

Glass-fibre reinforced polymer composites belong to a broader class of heterogeneous media types: the so-called composites materials. This chapter lays down fundamental concepts, and definitions for glass-fibre reinforced polymer mostly used in tanks design and manufacturing. First, it introduces the two primary constituents materials, glass fibres and thermoset polymer resins. Then explores the manufacturing processes adopted for tanks. Next presents some theoretical aspects concerning the mechanical properties of GFRP. Finally, it illustrates the custom procedure we develop, that implements the stiffness prediction of composite laminates.

3.1 Introduction

A structural composite is a material system consisting of two or more phases on a macroscopic scale. The properties and mechanical performance of composite are superior to those of its constituent materials acting independently. The reinforcement is the discontinuous, stiffer, and stronger phase, whereas the continuous, less stiff and weaker phase is called the matrix. In the following, we discuss polymer composite systems containing glass fibre as reinforcement and thermoset resins as the matrix. From the technological perspective, we focus our attention on glass fibres formats and thermoset

matrix resins types frequently used for tanks manufacturing.

3.2 Raw materials

3.2.1 Glass fibres

The most important reinforcement fibre is E-glass (lime aluminium borosilicate) because of its high tensile strength, good chemical resistance, and relatively low cost. E-glass fibres have high tensile strength since of the low number and size of defects on the fibre's surface of the fibre. Continuous glass fibres are formed by extruding molten glass to filament diameters between 5 μm to 25 μm , Table 3.1 reports the typical properties of E-glass fibre. The individual fibres have a thin surface coating of mainly organic material, the *size*, applied during their manufacture. *Sizing* is the process of coating fibres with a size. The sizing helps protect the fibres acting as a lubricant and antistatic agent before combining 102 or 204 filaments of fibres in a *strand*. Moreover, the sizing acts as a coupling agent during resin impregnation of dry fibres, to promote bonding with the composite matrix. It is worth noting that strands are spun together from fibres produced simultaneously from a single furnace. A single strand is an untwisted bundle of continuous fibres and represents the basic unit for producing other different arrangements of fibres. For example, the *roving*, used in the filament winding technique, is a collection of untwisted parallel strands (Figure 3.1 (a)). Concerning the so-called fabrics, the *chopped strand mat* (CSM) used, e.g., in hand lay-up technique is made by randomly oriented chopped strands (Figure 3.1 (b)). Figures 3.1(c) and 3.1 (d) show *uniaxial* and *woven roving* fabric, respectively.

Table 3.1: Properties of typical E-glass fibre.

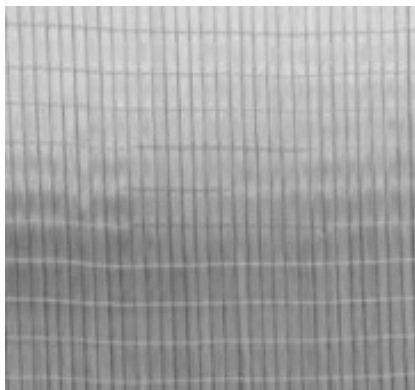
Property	Unit	value
Density	(kg m^{-3})	2560
Modulus of elasticity	(MPa)	74000
Shear Modulus	(MPa)	30000
Poisson's Ratio	(-)	0.25



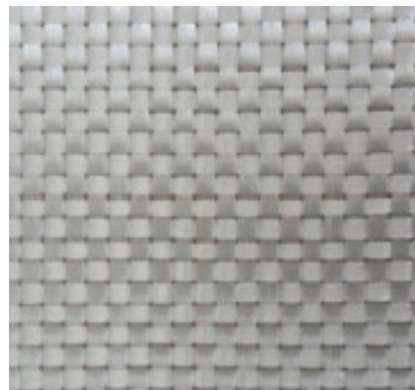
(a) Roving (Oven Corning)



(b) Chopped Strand Mat



(c) Uniaxial fabric



(d) Woven roving fabric

Figure 3.1: Example of glass fibres formats.

3.2.2 Polymer resins

In the following with the word ‘resin’ we refer to thermoset resins. A thermoset matrix is formed by the irreversible chemical transformation of a resin system into a cross-linked polymer matrix. In general, the polymer is called a resin system during processing and matrix after the polymer has cured, [58]. Thermoset resins have low viscosity, which allows for excellent impregnation of the fiber reinforcement and high processing speeds. Thermoset resins are the most common resin systems. Table 3.2, lists the properties of three commonly used resins. The resin (matrix) transfers the

Table 3.2: Properties of commonly used resins.

Resins	Density (kg m^{-3})	Elastic Modulus (MPa)	Shear Modulus (MPa)	Poisson’s ratio (–)
Epoxy	1200	4500	1600	0.40
Polyester	1200	4000	1400	0.40
Vinylester	1110	3500	1270	0.38

externally applied loads to the reinforcement (fibres). Besides, the matrix protects the reinforcement from mechanical, physical, chemical degradation, which would lead to a loss in performance. The mechanical characteristics of a composite depend primarily on the mechanical properties of the combined materials. However, the fibre-resin bonding nature and the stress transfer mode at the fibre-resin interface play an important role. The need for an excellent fibre-resin bonding explains the use of coupling agents, e.g. sizing, in the fibre production.

3.3 Manufacturing methods

Tanks related to this work are composed by three distinct structural elements, the flat bottom, the cylindrical wall and the top head (Figure 3.2). The top head can be in different shapes, flat, elliptical, torispherical, hemispherical or conical (Figure 3.3). In general both the ends are made by the *hand lay-up* technique and the cylindrical wall is manufactured by the *filament winding* process. With overlays made by hand lay-up or filament

winding, flat bottom and top head are joined to the base and to the top of cylindrical wall, respectively.

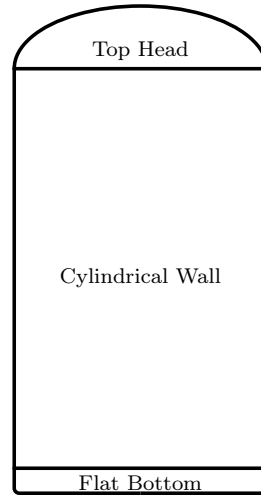


Figure 3.2: Components of a GFRP tank.

3.3.1 Hand lay-up

The hand lay-up technique, also called wet lay-up, is the simplest and oldest manufacturing process suited especially for large fibreglass components. Desired shape/thickness is achieved by using an open mould. This mould may be convex or concave type, depending on which surface needs to be smooth. After properly preparing the mould with a release agent, fibres can be laid onto the mould by hand. The reinforcement is applied in the form of chopped strand mat, woven roving and combinations of both. Pre-measured resin and catalyst (hardener) are thoroughly mixed together

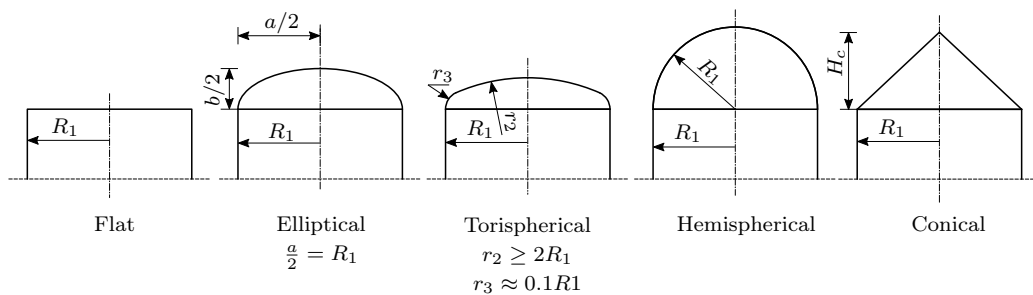


Figure 3.3: Typical head types of tanks.

and the mixture poured and brushed on. To ensure complete air removal and wet-out, rollers are used to compact the material against the mould to remove any entrapped air (Figure 3.4). At full impregnation of fibres another layer of reinforcement is added and so forth. Resin-catalyst mixture can be deposited on the glass fibres also by a spray gun, which automatically combines the right proportions of the ingredients. Spray lay-up is an open

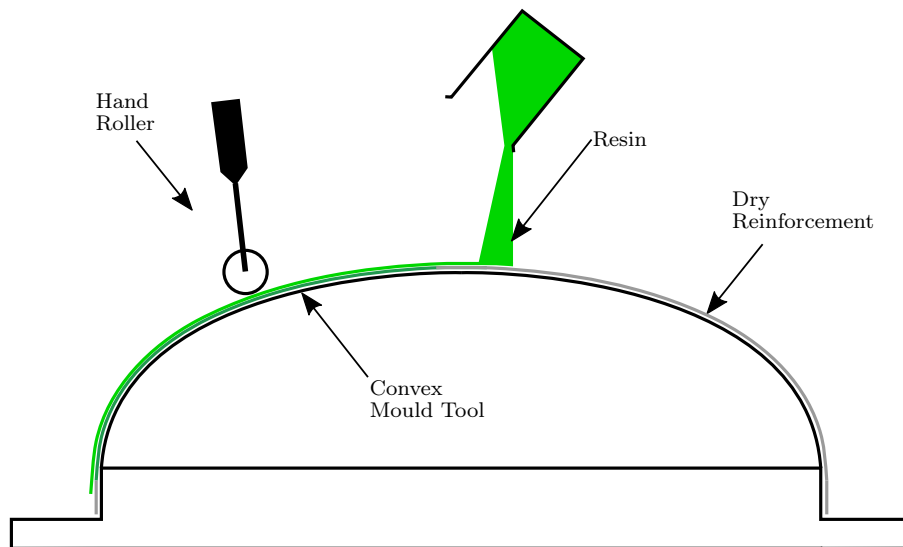


Figure 3.4: Schematic diagram of hand lay-up process.

moulded process quite similar to hand lay-up, is normally used when a high volume of components are required on a regular basis. With spray lay-up catalysed resin and glass fibre strands are sprayed directly onto the mould, obtaining chopped strand mat layers. When sprayed, the fibre strands are steadily cut by the chopper of the spray gun. Production operators after the application of a defined thickness, consolidate the laminate using paddle rollers and brushes. Layers with different fibreglass fabric e.g. WR, can also be manually alternated to CSM layers.

3.3.2 Filament winding

Filament winding (FW) is a process used for the manufacture of axisymmetric geometries such as cylinders, tapered shafts and spheres. A continuous length of glass fibres impregnated with a liquid resin, by passing them through an in-line resin bath, are wound over a rotating mandrel. Depending

on the desired properties of the product, winding patterns such as hoop, and helical can be developed. From the simple mechanical winder of Richard E. Young (1940) [59] up to the eighties, the parameters affecting the winding process, e.g. winding tension, stacking sequence, winding-tension gradient, winding time etc., were mechanically/manually controlled. Only in the last two decades filament winding machines have been improved by important technological advances and nowadays, mechanical, electrical and electronics components have all CNC (Computerized Numerical Control) controlled. Figure 3.5 shows a schematic illustration of a conventional horizontal filament winding machine. The dry fibres, roving, are pulled from a spool rack (creel) through the resin impregnator to the pay-out eye. The Resin impregnator and the pay-out eye run through a carriage that moves back and forth over the length of the part, covering the mandrel in a specified *pattern* with the impregnated fibre band. Filament winding technique has three winding patterns, which are the hoop, helical and polar winding. The cylindrical part of the tank uses the hoop and the helical winding pattern. Figure 3.6, from [60], illustrates the steps of a typical helical pattern filament winding process.

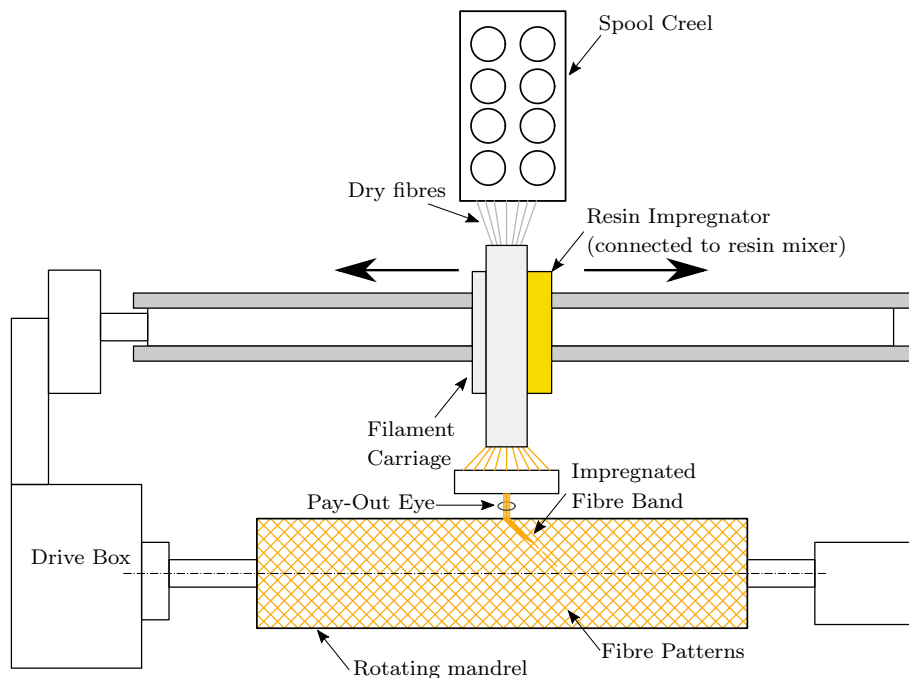


Figure 3.5: Schematic of basic filament winding process.

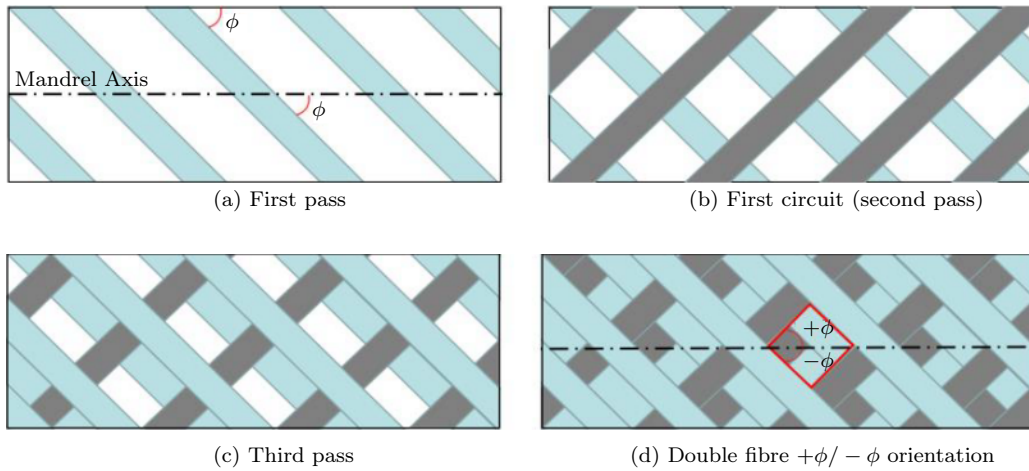


Figure 3.6: Typical helical pattern filament winding process after [60]

3.4 Stiffness prediction of GRFP laminates

This section provides an overview of techniques for the analysis of composite materials. Starting with basic notions of tensors, the constitutive equation of an anisotropic hyperelastic material is derived. Then are considered the micromechanics of fibre and matrix in a lamina, the ply mechanics and macromechanics.

Mathematical entities are indicated as follows:

- with bold uppercase letters we indicate second-order tensors, e.g. \mathbf{T} is a tensor, moreover with \mathbb{C} we indicate a fourth-order tensor;
- with bold lowercase letters we indicate vectors, e.g. \mathbf{u} is a vector;
- with italics lowercase letters we indicate scalars, e.g. α is a scalar.

In the expression the summations over repeated indexes are treated using Einstein's contracted notation.

3.4.1 Stress, strain and constitutive equations

First, let us recall some useful definitions. Considering a finite linear vector space V , a second-order tensor is a mathematical entity that satisfies the following:

Definition 3.4.1. A second-order tensor \mathbf{L} is a linear application from V to V :

$$\mathbf{L} : V \rightarrow V$$

such that:

$$\mathbf{L}(\alpha\mathbf{u} + \beta\mathbf{v}) = \alpha\mathbf{L}\mathbf{u} + \beta\mathbf{L}\mathbf{v} \quad \forall \alpha, \beta \in \mathbb{R}, \forall \mathbf{u}, \mathbf{v} \in V. \quad (3.1)$$

Definition 3.4.2. Let V a finite linear vector space. $Lin V$ is the set of all second-order tensors over V :

$$Lin V = \{\mathbf{L} \mid \mathbf{L} : V \rightarrow V, \mathbf{L} \text{ is linear}\}$$

Definition 3.4.3. A fourth-order tensor \mathbb{C} is a linear application from $Lin V$ to $Lin V$:

$$\mathbb{C} : Lin V \rightarrow Lin V$$

such that:

$$\mathbb{C}(\alpha\mathbf{T} + \beta\mathbf{S}) = \alpha\mathbb{C}\mathbf{T} + \beta\mathbb{C}\mathbf{S} \quad \forall \alpha, \beta \in \mathbb{R}, \forall \mathbf{T}, \mathbf{S} \in Lin V \quad (3.2)$$

hereinafter the vector space V will be replaced by the vector space \mathbb{R}^3 .

Given a continuum body $\Omega \subset \mathbb{R}^3$ subjected to loads and displacement boundary conditions, the state of stress *evaluated at certain point* $\mathbf{p} \in \Omega$ is described by a symmetric second-order tensor \mathbf{T} called *stress tensor*, [61]. Defining an orthonormal basis $\mathcal{B} = \{\mathbf{e}_i\}_{i=1}^3$ of \mathbb{R}^3 , \mathbf{T} can be represented as a 3×3 real matrix indicated with \mathbf{T} :

$$\mathbf{T} = \begin{bmatrix} \sigma_{11} & \sigma_{12} & \sigma_{13} \\ \sigma_{12} & \sigma_{22} & \sigma_{23} \\ \sigma_{13} & \sigma_{23} & \sigma_{33} \end{bmatrix}$$

Imagine a plane surface Π passing through the internal point $\mathbf{p} \in \Omega$. Let \mathbf{n} be the normal vector of Π , applied in \mathbf{p} . The stress tensor takes \mathbf{n} and provides another vector \mathbf{t} called *stress vector*:

$$\mathbf{t} = \mathbf{T}\mathbf{n} \Rightarrow t_i = \sigma_{ij}n_j$$

Because of loads and displacement boundary conditions, Ω deforms. The displacement of each point $\mathbf{p} \in \Omega$ is described by the displacement field $\mathbf{u} = (u_1, u_2, u_3)$. From \mathbf{u} it is possible to define the state of strain of Ω evaluated at \mathbf{p} . The symmetric second-order tensor \mathbf{E} characterizes the state

of strain. Therefore, given the unit vector base \mathcal{B} , the components of \mathbf{E} are defined by:

$$E_{ij} = \frac{1}{2} \left(\frac{\partial u_i}{\partial x_j} + \frac{\partial u_j}{\partial x_i} \right) \quad (3.3)$$

The components of \mathbf{E} are written as $\varepsilon_{ij} = E_{ij} \forall i = j$ and $\gamma_{ij} = 2E_{ij} \forall i \neq j$, and the matrix representing \mathbf{E} becomes:

$$\mathbf{E} = \begin{bmatrix} \varepsilon_{11} & \gamma_{12}/2 & \gamma_{13}/2 \\ \gamma_{12}/2 & \varepsilon_{22} & \gamma_{23}/2 \\ \gamma_{13}/2 & \gamma_{23}/2 & \varepsilon_{33} \end{bmatrix}$$

We can say that:

- the tensor \mathbf{T} represent a measure of stress;
- the tensor \mathbf{E} represent a measure of strain.

The mechanical properties of the material Ω join these two measures by a fourth-order tensor \mathbb{C} called *elastic tensor*, which acts in such a way:

$$\mathbf{T} = \mathbb{C}\mathbf{E} \quad (3.4)$$

Equation (3.4) is the so-called *constitutive equation*. The expansion of the components of (3.4) leads to:

$$T_{ij} = C_{ijrs} E_{rs}$$

A $3 \times 3 \times 3 \times 3$ real matrix, which has 81 elements, represents the elastic tensor \mathbb{C} . However, symmetrical properties of \mathbf{T} and \mathbf{E} imply:

$$C_{ijrs} = C_{jirs} = C_{ijsr} \quad (3.5)$$

these are called *minor symmetries* of \mathbb{C} . Accordingly, the number of independent elements of \mathbb{C} reduces to 36. If the material is assumed to be *hyperelastic*, i.e. the components of \mathbf{T} are given by:

$$T_{ij} = \frac{\partial w(\mathbf{E})}{\partial E_{ij}} \quad (3.6)$$

where $w(\mathbf{E})$ is the *elastic strain energy* defined as:

$$w(\mathbf{E}) = \frac{1}{2} \mathbb{C}\mathbf{E} \cdot \mathbf{E} \quad (3.7)$$

where \cdot denotes the inner product between two second order tensors.

It can be shown that only 21 independent elements of \mathbb{C} are left over. Indeed for hyperelastic materials holds the following property, called *major symmetry* of \mathbb{C} :

$$C_{ijrs} = C_{rsij}$$

It is worth noting that exploiting the so-called *material symmetries transformation* the number of independent elements further reduce.

Given the symmetrical properties of \mathbf{T} , \mathbf{E} and \mathbb{C} adopting the *Voigt's notation*, \mathbf{T} is represented by the following vector:

$$\boldsymbol{\sigma} = [\sigma_1 \ \sigma_2 \ \sigma_3 \ \sigma_4 \ \sigma_5 \ \sigma_6]^\top \quad (3.8)$$

where: $\sigma_1 = \sigma_{11}$, $\sigma_2 = \sigma_{22}$, $\sigma_3 = \sigma_{33}$, $\sigma_4 = \sigma_{23}$, $\sigma_5 = \sigma_{13}$, $\sigma_6 = \sigma_{12}$. Similarly \mathbf{E} is represented by the following vector:

$$\boldsymbol{\varepsilon} = [\varepsilon_1 \ \varepsilon_2 \ \varepsilon_3 \ \gamma_4 \ \gamma_5 \ \gamma_6]^\top$$

where: $\varepsilon_1 = \varepsilon_{11}$, $\varepsilon_2 = \varepsilon_{22}$, $\varepsilon_3 = \varepsilon_{33}$, $\gamma_4 = \gamma_{23}$, $\gamma_5 = \gamma_{13}$, $\gamma_6 = \gamma_{12}$. For a hyperelastic material, Daniel and Ishai in [8, p. 65], explain the steps to achieve the contracted form of \mathbb{C} with a *symmetric* 6×6 matrix:

$$\mathbf{C} = \begin{bmatrix} C_{11} & C_{12} & C_{13} & C_{14} & C_{15} & C_{16} \\ C_{12} & C_{22} & C_{23} & C_{24} & C_{25} & C_{26} \\ C_{13} & C_{23} & C_{33} & C_{34} & C_{35} & C_{36} \\ C_{14} & C_{24} & C_{34} & C_{44} & C_{45} & C_{46} \\ C_{15} & C_{25} & C_{35} & C_{45} & C_{55} & C_{56} \\ C_{16} & C_{26} & C_{36} & C_{46} & C_{56} & C_{66} \end{bmatrix} \quad (3.9)$$

\mathbf{C} has 21 independent elements. Using Voigt's contracted notation the constitutive equation (3.4) becomes:

$$\boldsymbol{\sigma} = \mathbf{C}\boldsymbol{\varepsilon} \quad (3.10)$$

\mathbf{C} is called *stiffness matrix*. Its inverse matrix \mathbf{S} , if exists, is called *compliance matrix* and is such that:

$$\boldsymbol{\varepsilon} = \mathbf{S}\boldsymbol{\sigma}. \quad (3.11)$$

3.5 Micromechanics of composites

Fibreglass composite material system consist of two constituents, the resin matrix and the glass fibre reinforcement. The composite material is heterogeneous, given that the constituents form two distinct, separated phases. The micromechanics study of composite materials considers the interaction of the constituent materials [7]. In particular, micromechanics let the designer to represent a heterogeneous material and its related properties as an equivalent homogeneous material usually anisotropic. However, a composite's mechanical properties are strictly related to the relative volume of fibre and resin used.

Let v_m, v_f, v_c be the volumes of the matrix, of the fibres and the composite, respectively. The following equation holds:

$$v_c = v_m + v_f \quad (3.12)$$

Therefore it is possible to define the following ratios:

$$V_m = \frac{v_m}{v_c} \quad \text{matrix volume fraction}$$

$$V_f = \frac{v_f}{v_c} \quad \text{fibre volume fraction}$$

the sum of the volume fractions gives:

$$V_f + V_m = 1$$

Given the density of the matrix, the fibre and the whole composite, ρ_m, ρ_f and ρ_c , respectively, we can calculate the mass of the composite constituents:

$$w_m = \rho_m v_m \quad (3.13)$$

$$w_f = \rho_f v_f \quad (3.14)$$

$$w_c = \rho_c v_c \quad (3.15)$$

where w_m, w_f, w_c are the mass of the matrix, of the fibres and of the composite material and:

$$w_c = w_m + w_f \quad (3.16)$$

From these masses we can define the following ratios:

$$W_m = \frac{w_m}{w_c} \quad \text{matrix mass fraction} \quad (3.17)$$

$$W_f = \frac{w_f}{w_c} \quad \text{fibre mass fraction} \quad (3.18)$$

W_f and W_m are such that:

$$W_f + W_m = 1$$

Rearranging Equations (3.13), (3.14) and (3.15) we obtain:

$$\rho_m = \frac{w_m}{v_m} = \frac{w_m/w_c w_c}{v_m/v_c w_c} = \frac{W_m}{V_m} \rho_c$$

$$\rho_f = \frac{w_f}{v_f} = \frac{w_f/w_c w_c}{w_f/w_c w_c} = \frac{W_f}{V_f} \rho_c$$

The substitution of these two equations into (3.12) and (3.16) leads to:

$$\rho_c = \rho_m V_m + \rho_f V_f \quad (3.19)$$

$$\frac{1}{\rho_c} = \frac{W_m}{\rho_m} + \frac{W_f}{\rho_f} \quad (3.20)$$

It is possible to calculate the composite material's density given the matrix and the glass fibre density and the volume fraction or the mass fraction. for n constituents the Equations (3.19) and (3.20) become:

$$\rho_c = \sum_{i=1}^n \rho_i V_i$$

$$\frac{1}{\rho_c} = \sum_{i=1}^n \frac{W_i}{\rho_i}$$

and for a generic constituent must hold:

$$\frac{\rho_i}{\rho_c} = \frac{W_i}{V_i}$$

The following micromechanics analysis concerns only the so-called long fibre reinforced composite materials. Continuum Mechanics theory asserts that two constants completely characterize an isotropic material's mechanical response: Young's modulus E and Poisson's ratio ν . We assume that the matrix and the reinforcement, with known mechanical properties, are *isotropic*. Therefore, for characterizing a composite, we have two couples of constants, Young's moduli and Poisson's ratio, for resin, E_m and ν_m , for the resin and E_f and ν_f , for the reinforcement. Given E and ν , the *shear modulus* can be calculated from the equation (see the proof in Appendix A) below:

$$G = \frac{E}{2(1 + \nu)} \quad (3.21)$$

G_m and G_f calculated with Equation 3.21 are the shear moduli for the matrix and for the fibres respectively.

We focus the attention only on a small portion of composite material suitable to describe the composite material as a whole. This portion is the so-called *Representative Volume Element, RVE*. The RVE is heterogeneous since it embeds both the matrix and the fibres. The micromechanics goal is to determine the mechanical properties of an equivalent, homogeneous material, that replaces the RVE without affecting the state of stress around it. The resultant equivalent material, with the fair assumption that the fibers are randomly distributed in the cross section, is transversely isotropic and it is defined by *five* constants. Using this concept many authors proposed different expressions to calculate these constants. In the following we list the equations reported in [7]:

1. E_1 longitudinal (i.e. in the fibres directions) Young's modulus:

$$E_1 = E_m V_m + E_f V_f \quad (3.22)$$

2. E_2 transverse (i.e. in the direction orthogonal to the fibres direction) Young's modulus:

$$E_2 = E_m \frac{1 + \xi \eta V_f}{1 - \eta V_f} \quad (3.23)$$

$$\eta = \frac{E_f/E_m - 1}{E_f/E_m + \xi} \quad (3.24)$$

where $\xi = 2$ for circular and square cross-section fibres, or $\xi = 2a/b$ for rectangular $a \times b$ cross-section fibres;

3. ν_{12} in-plane Poisson's ratio:

$$\nu_{12} = \nu_m V_m + \nu_f V_f \quad (3.25)$$

4. G_{12} in-plane shear modulus:

$$G_{12} = \frac{(1 + V_f) + (1 - V_f)G_m/G_f}{(1 - V_f) + (1 + V_f)G_m/G_f} \quad (3.26)$$

5. G_{23} out-of-plane shear modulus, or also called inter-laminar shear modulus:

$$G_{23} = \frac{V_f + \eta_4(1 - V_f)}{\eta_4(1 - V_f) + V_f G_m / G_f} \quad (3.27)$$

$$\eta_4 = \frac{3 - 4\nu_m + G_m / G_f}{4(1 - \nu_m)} \quad (3.28)$$

$G_{13} = G_{12}$ because the assumption of transversely isotropic material.

3.6 Elastic Constants of a Lamina

Generally, composite materials structures are plates or shells with two dimensions, length and width, larger than the third, the thickness. In this case, it is possible to assume null stress along the plate thickness, namely:

$$\sigma_3 = 0 \quad (3.29)$$

With the aforementioned assumption we want to determine, for a specific lamina, the general constitutive equation (3.10) (or equivalently (3.11)), using for convenience the contracted notation. First, we define two orthonormal reference frames, second, we represent the constitutive equation with respect of \mathcal{B} and \mathcal{D} and finally, we find the relationship between the two representations. The two orthonormal reference frames, Figure 3.7, are:

- the material reference frame $(1, 2, 3)$ with its related generators collected in the basis $\mathcal{B} = \{\mathbf{e}_1, \mathbf{e}_2, \mathbf{e}_3\}$, with \mathbf{e}_1 aligned to the fibres direction, \mathbf{e}_2 perpendicular to \mathbf{e}_1 lying in the plane of the laminate and $\mathbf{e}_3 = \mathbf{e}_1 \times \mathbf{e}_2$;
- the laminate reference frame (x, y, z) with its related generators collected in the basis $\mathcal{D} = \{\boldsymbol{\eta}_x, \boldsymbol{\eta}_y, \boldsymbol{\eta}_z\}$;

The constitutive equation in material coordinates can be written as:

$$\begin{bmatrix} \sigma_1 \\ \sigma_2 \\ \sigma_3 \\ \sigma_4 \\ \sigma_5 \\ \sigma_6 \end{bmatrix} = \begin{bmatrix} C_{11} & C_{12} & C_{12} & 0 & 0 & 0 \\ C_{12} & C_{22} & C_{23} & 0 & 0 & 0 \\ C_{12} & C_{23} & C_{22} & 0 & 0 & 0 \\ 0 & 0 & 0 & (C_{22} - C_{23})/2 & 0 & 0 \\ 0 & 0 & 0 & 0 & C_{55} & 0 \\ 0 & 0 & 0 & 0 & 0 & C_{55} \end{bmatrix} \begin{bmatrix} \varepsilon_1 \\ \varepsilon_2 \\ \varepsilon_3 \\ \gamma_4 \\ \gamma_5 \\ \gamma_6 \end{bmatrix} \quad (3.30)$$

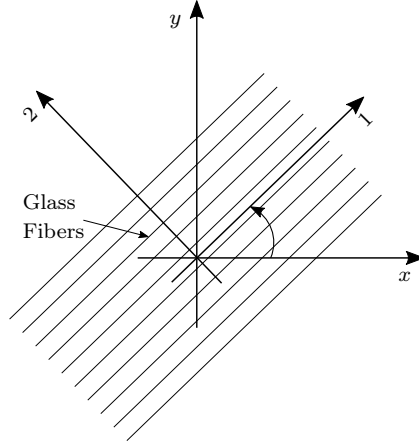


Figure 3.7: Material, (1, 2, 3), and laminate, (x, y, z), reference frame.

Expanding the first three equations taking into account the hypothesis $\sigma_3 = 0$ gives:

$$\sigma_1 = C_{11}\varepsilon_1 + C_{12}\varepsilon_2 + C_{12}\varepsilon_3 \quad (3.31)$$

$$\sigma_2 = C_{12}\varepsilon_1 + C_{22}\varepsilon_2 + C_{23}\varepsilon_3 \quad (3.32)$$

$$\sigma_3 = C_{12}\varepsilon_1 + C_{23}\varepsilon_2 + C_{22}\varepsilon_3 = 0 \quad (3.33)$$

isolating ε_3 from (3.31) and substituting it into (3.32) and (3.33), we have:

$$\begin{aligned} \sigma_1 &= \left(C_{11} - \frac{C_{12}C_{12}}{C_{22}}\right)\varepsilon_1 + \left(C_{12} - \frac{C_{12}C_{23}}{C_{22}}\right)\varepsilon_2 \\ \sigma_2 &= \left(C_{12} - \frac{C_{23}C_{12}}{C_{22}}\right)\varepsilon_1 + \left(C_{22} - \frac{C_{23}C_{23}}{C_{22}}\right)\varepsilon_2 \\ \sigma_3 &= -\frac{C_{12}}{C_{22}}\varepsilon_1 - \frac{C_{23}}{C_{22}}\varepsilon_2 \end{aligned}$$

Further transformation allows us to reduce (3.31) and (3.32) to

$$\begin{aligned} \sigma_1 &= C_{11}^*\varepsilon_1 + C_{12}^*\varepsilon_2 \\ \sigma_2 &= C_{12}^*\varepsilon_1 + C_{22}^*\varepsilon_2 \end{aligned}$$

where:

$$\begin{aligned} C_{11}^* &= \left(C_{11} - \frac{C_{12}C_{12}}{C_{22}}\right) & C_{12}^* &= \left(C_{12} - \frac{C_{12}C_{23}}{C_{22}}\right) \\ C_{22}^* &= \left(C_{22} - \frac{C_{23}C_{23}}{C_{22}}\right) \end{aligned}$$

Therefore the equation (3.30) is compacted as follows:

$$\begin{bmatrix} \sigma_1 \\ \sigma_2 \\ \sigma_4 \\ \sigma_5 \\ \sigma_6 \end{bmatrix} = \begin{bmatrix} C_{11}^* & C_{12}^* & 0 & 0 & 0 \\ C_{12}^* & C_{22}^* & 0 & 0 & 0 \\ 0 & 0 & (C_{22} - C_{23})/2 & 0 & 0 \\ 0 & 0 & 0 & C_{55} & 0 \\ 0 & 0 & 0 & 0 & C_{55} \end{bmatrix} \begin{bmatrix} \varepsilon_1 \\ \varepsilon_2 \\ \gamma_4 \\ \gamma_5 \\ \gamma_6 \end{bmatrix} \quad (3.34)$$

The inversion of (3.30) leads to:

$$\begin{bmatrix} \varepsilon_1 \\ \varepsilon_2 \\ \varepsilon_3 \\ \gamma_4 \\ \gamma_5 \\ \gamma_6 \end{bmatrix} = \begin{bmatrix} S_{11} & S_{12} & S_{12} & 0 & 0 & 0 \\ S_{12} & S_{22} & S_{23} & 0 & 0 & 0 \\ S_{12} & S_{23} & S_{22} & 0 & 0 & 0 \\ 0 & 0 & 0 & 2(S_{22} - S_{23}) & 0 & 0 \\ 0 & 0 & 0 & 0 & S_{55} & 0 \\ 0 & 0 & 0 & 0 & 0 & S_{55} \end{bmatrix} \begin{bmatrix} \sigma_1 \\ \sigma_2 \\ \sigma_3 \\ \sigma_4 \\ \sigma_5 \\ \sigma_6 \end{bmatrix} \quad (3.35)$$

Equations (3.30) and (3.35) can be easily recovered for a hyperelastic material considering that the symmetries transformations for a transversely isotropic material consist of three reflections:

$$\mathbf{Q}_1 = \begin{bmatrix} -1 & 0 & 0 \\ 0 & 1 & 0 \\ 0 & 0 & 1 \end{bmatrix} \quad \mathbf{Q}_2 = \begin{bmatrix} 1 & 0 & 0 \\ 0 & -1 & 0 \\ 0 & 0 & 1 \end{bmatrix} \quad \mathbf{Q}_3 = \begin{bmatrix} 1 & 0 & 0 \\ 0 & 1 & 0 \\ 0 & 0 & -1 \end{bmatrix}$$

and one rotation about the axis 1:

$$\mathbf{Q}_4 = \begin{bmatrix} 1 & 0 & 0 \\ 0 & \cos \theta & \sin \theta \\ 0 & -\sin \theta & \cos \theta \end{bmatrix} \quad \forall \theta \in [0, 2\pi]$$

and recalling the change of basis for a fourth-order tensor:

$$C_{abcd} = C_{ijrs} Q_{ai} Q_{bj} Q_{cr} Q_{ds}$$

Equation (3.35) compacted according to (3.34) gives:

$$\begin{bmatrix} \varepsilon_1 \\ \varepsilon_2 \\ \gamma_4 \\ \gamma_5 \\ \gamma_6 \end{bmatrix} = \begin{bmatrix} S_{11} & S_{12} & 0 & 0 & 0 \\ S_{12} & S_{22} & 0 & 0 & 0 \\ 0 & 0 & 2(S_{22} - S_{23}) & 0 & 0 \\ 0 & 0 & 0 & S_{55} & 0 \\ 0 & 0 & 0 & 0 & S_{55} \end{bmatrix} \begin{bmatrix} \sigma_1 \\ \sigma_2 \\ \sigma_4 \\ \sigma_5 \\ \sigma_6 \end{bmatrix} \quad (3.36)$$

From the mechanical constants expressed in (3.22), (3.23), (3.25), (3.26), (3.27) and, since the compliance matrix must be symmetric and the following must be satisfied,

$$\frac{\nu_{12}}{E_1} = \frac{\nu_{21}}{E_2} \quad (3.37)$$

we get the elements of the compliance matrix \mathbf{S} of (3.36):

$$\begin{aligned} S_{11} &= \frac{1}{E_1} & S_{12} &= -\frac{\nu_{12}}{E_1} = -\frac{\nu_{21}}{E_2} & S_{22} &= \frac{1}{E_2} \\ S_{44} &= 2(S_{22} - S_{23}) = \frac{1}{G_{23}} \\ S_{55} &= \frac{1}{G_{12}} = \frac{1}{G_{13}} \end{aligned}$$

Gathering previous information, Equation (3.36) becomes:

$$\begin{bmatrix} \varepsilon_1 \\ \varepsilon_2 \\ \gamma_4 \\ \gamma_5 \\ \gamma_6 \end{bmatrix} = \begin{bmatrix} 1/E_1 & -\nu_{21}/E_2 & 0 & 0 & 0 \\ -\nu_{12}/E_1 & 1/E_2 & 0 & 0 & 0 \\ 0 & 0 & 1/G_{23} & 0 & 0 \\ 0 & 0 & 0 & 1/G_{13} & 0 \\ 0 & 0 & 0 & 0 & 1/G_{12} \end{bmatrix} \begin{bmatrix} \sigma_1 \\ \sigma_2 \\ \sigma_4 \\ \sigma_5 \\ \sigma_6 \end{bmatrix} \quad (3.38)$$

Finally the inversion of (3.38) gives the explicit components of (3.34):

$$\begin{bmatrix} \sigma_1 \\ \sigma_2 \\ \sigma_4 \\ \sigma_5 \\ \sigma_6 \end{bmatrix} = \begin{bmatrix} E_1/\Delta & \nu_{21}E_1/\Delta & 0 & 0 & 0 \\ \nu_{12}E_2/\Delta & E_2/\Delta & 0 & 0 & 0 \\ 0 & 0 & G_{23} & 0 & 0 \\ 0 & 0 & 0 & G_{13} & 0 \\ 0 & 0 & 0 & 0 & G_{12} \end{bmatrix} \begin{bmatrix} \varepsilon_1 \\ \varepsilon_2 \\ \gamma_4 \\ \gamma_5 \\ \gamma_6 \end{bmatrix} \quad (3.39)$$

where $\Delta = 1 - \nu_{12}\nu_{21}$.

3.6.1 Coordinate transformation

This section provides the transformation of the constitutive equation from two sets of right-handed rectangular cartesian axes, the *material coordinates* system (1, 2, 3) to the *laminate coordinates*. The transformation refers to a plane coordinate change in which $\mathbf{e}_3 = \boldsymbol{\eta}_z$. Therefore, the coordinate change expressed with respect to the generators gives:

$$\begin{bmatrix} \mathbf{e}_1 \\ \mathbf{e}_2 \\ \mathbf{e}_3 \end{bmatrix} = \begin{bmatrix} \cos \theta & \sin \theta & 0 \\ -\sin \theta & \cos \theta & 0 \\ 0 & 0 & 1 \end{bmatrix} \begin{bmatrix} \boldsymbol{\eta}_x \\ \boldsymbol{\eta}_y \\ \boldsymbol{\eta}_z \end{bmatrix} \quad (3.40)$$

Writing a generic vector \mathbf{x} referring to both the basis we have:

$$x = x_1\mathbf{e}_1 + x_2\mathbf{e}_2 + x_3\mathbf{e}_3 = x\boldsymbol{\eta}_x + y\boldsymbol{\eta}_y + z\boldsymbol{\eta}_z$$

the applied coordinate change (3.40) works as follows:

$$\begin{bmatrix} x_1 \\ x_2 \\ x_3 \end{bmatrix} = \begin{bmatrix} \cos \theta & \sin \theta & 0 \\ -\sin \theta & \cos \theta & 0 \\ 0 & 0 & 1 \end{bmatrix} \begin{bmatrix} x \\ y \\ z \end{bmatrix}$$

The inversion of the last relationship leads to:

$$\begin{bmatrix} x \\ y \\ z \end{bmatrix} = \begin{bmatrix} \cos \theta & -\sin \theta & 0 \\ \sin \theta & \cos \theta & 0 \\ 0 & 0 & 1 \end{bmatrix} \begin{bmatrix} x_1 \\ x_2 \\ x_3 \end{bmatrix}$$

Given the strain components in material coordinate, the strain components in laminate coordinate become:

$$\begin{aligned} \varepsilon_x &= \frac{\partial u_x}{\partial x} = \frac{\partial}{\partial x}(\cos \theta u_1 - \sin \theta u_2) = \\ &= \cos \theta \left(\frac{\partial u_1}{\partial x_1} \frac{\partial x_1}{\partial x} + \frac{\partial u_1}{\partial x_2} \frac{\partial x_2}{\partial x} \right) - \sin \theta \left(\frac{\partial u_2}{\partial x_1} \frac{\partial x_1}{\partial x} + \frac{\partial u_2}{\partial x_2} \frac{\partial x_2}{\partial x} \right) = \\ &= \cos^2 \theta \frac{\partial u_1}{\partial x_1} + \sin^2 \theta \frac{\partial u_2}{\partial x_2} - \sin \theta \cos \theta \left(\frac{\partial u_1}{\partial x_2} + \frac{\partial u_2}{\partial x_1} \right) = \\ &= \cos^2 \theta \varepsilon_1 + \sin^2 \theta \varepsilon_2 - \sin \theta \cos \theta \gamma_6 = \\ &= \cos^2 \theta \varepsilon_1 + \sin^2 \theta \varepsilon_2 - 2 \sin \theta \cos \theta \frac{1}{2} \gamma_6 \end{aligned} \quad (3.41)$$

Similarly for ε_y :

$$\varepsilon_y = \sin^2 \theta \varepsilon_1 + \cos^2 \theta \varepsilon_2 + 2 \sin \theta \cos \theta \frac{1}{2} \gamma_6 \quad (3.42)$$

and for γ_6 .

$$\frac{\gamma_{xy}}{2} = \cos \theta \sin \theta \varepsilon_1 - \cos \theta \sin \theta \varepsilon_2 + \frac{\gamma_6}{2} \quad (3.43)$$

Gathering equations (3.41), (3.42) and (3.43), the matrix form gives:

$$\begin{bmatrix} \varepsilon_x \\ \varepsilon_y \\ \frac{\gamma_{xy}}{2} \end{bmatrix} = \begin{bmatrix} \cos^2 \theta & \sin^2 \theta & -2 \cos \theta \sin \theta \\ \sin^2 \theta & \cos^2 \theta & 2 \cos \theta \sin \theta \\ \cos \theta \sin \theta & -\cos \theta \sin \theta & \cos^2 \theta - \sin^2 \theta \end{bmatrix} \begin{bmatrix} \varepsilon_1 \\ \varepsilon_2 \\ \frac{\gamma_6}{2} \end{bmatrix} \quad (3.44)$$

Applying the coordinate change (3.40), it can be easily proved that:

$$\begin{bmatrix} \gamma_{yz} \\ \gamma_{xz} \end{bmatrix} = \begin{bmatrix} \cos \theta & \sin \theta \\ -\sin \theta & \cos \theta \end{bmatrix} \begin{bmatrix} \gamma_4 \\ \gamma_5 \end{bmatrix} \quad (3.45)$$

Even more briefly, we may write equations (3.44) and (3.45) in the form:

$$\begin{bmatrix} \varepsilon_x \\ \varepsilon_y \\ \frac{\gamma_{xy}}{2} \end{bmatrix} = \mathbf{R}_1 \begin{bmatrix} \varepsilon_1 \\ \varepsilon_2 \\ \frac{\gamma_6}{2} \end{bmatrix} \quad \begin{bmatrix} \gamma_{yz} \\ \gamma_{xz} \end{bmatrix} = \mathbf{R}_2 \begin{bmatrix} \gamma_4 \\ \gamma_5 \end{bmatrix} \quad (3.46)$$

where:

$$\mathbf{R}_1 = \begin{bmatrix} \cos^2 \theta & \sin^2 \theta & -2 \cos \theta \sin \theta \\ \sin^2 \theta & \cos^2 \theta & 2 \cos \theta \sin \theta \\ \cos \theta \sin \theta & -\cos \theta \sin \theta & \cos^2 \theta - \sin^2 \theta \end{bmatrix} \quad \mathbf{R}_2 = \begin{bmatrix} \cos \theta & \sin \theta \\ -\sin \theta & \cos \theta \end{bmatrix}$$

The same procedure applies to stresses as follows:

$$\begin{bmatrix} \sigma_x \\ \sigma_y \\ \sigma_{xy} \end{bmatrix} = \mathbf{R}_1 \begin{bmatrix} \sigma_1 \\ \sigma_2 \\ \sigma_6 \end{bmatrix} \quad \begin{bmatrix} \sigma_{yz} \\ \sigma_{xz} \end{bmatrix} = \mathbf{R}_2 \begin{bmatrix} \sigma_4 \\ \sigma_5 \end{bmatrix} \quad (3.47)$$

3.6.2 Stiffness and compliance transformations

Given the coordinate changes for stress and strain, we write the coordinate change for the compliance matrix. Splitting the constitutive equation (3.39) in two parts gives:

$$\begin{bmatrix} \sigma_1 \\ \sigma_2 \\ \sigma_6 \end{bmatrix} = \begin{bmatrix} E_1/\Delta & \nu_{21}E_1/\Delta & 0 \\ \nu_{12}E_2/\Delta & E_2/\Delta & 0 \\ 0 & 0 & 2G_{12} \end{bmatrix} \begin{bmatrix} \varepsilon_1 \\ \varepsilon_2 \\ \frac{\gamma_6}{2} \end{bmatrix} \quad (3.48)$$

$$\begin{bmatrix} \sigma_4 \\ \sigma_5 \end{bmatrix} = \begin{bmatrix} G_{23} & 0 \\ 0 & G_{13} \end{bmatrix} \begin{bmatrix} \gamma_4 \\ \gamma_5 \end{bmatrix} \quad (3.49)$$

We can write Equation (3.48) in the form:

$$\begin{bmatrix} \sigma_1 \\ \sigma_2 \\ \sigma_6 \end{bmatrix} = \begin{bmatrix} 1 & 0 & 0 \\ 0 & 1 & 0 \\ 0 & 0 & 2 \end{bmatrix} \begin{bmatrix} E_1/\Delta & \nu_{21}E_1/\Delta & 0 \\ \nu_{12}E_2/\Delta & E_2/\Delta & 0 \\ 0 & 0 & G_{12} \end{bmatrix} \begin{bmatrix} \varepsilon_1 \\ \varepsilon_2 \\ \frac{\gamma_6}{2} \end{bmatrix} \quad (3.50)$$

Therefore, compacting relationships (3.50) and (3.49) we have:

$$\begin{bmatrix} \sigma_1 \\ \sigma_2 \\ \sigma_6 \end{bmatrix} = \mathbf{Q}\mathbf{L}_1 \begin{bmatrix} \varepsilon_1 \\ \varepsilon_2 \\ \frac{\gamma_6}{2} \end{bmatrix} \quad \begin{bmatrix} \sigma_4 \\ \sigma_5 \end{bmatrix} = \mathbf{L}_2 \begin{bmatrix} \gamma_4 \\ \gamma_5 \end{bmatrix}$$

where:

$$\mathbf{L}_1 = \begin{bmatrix} E_1/\Delta & \nu_{21}E_1/\Delta & 0 \\ \nu_{12}E_2/\Delta & E_2/\Delta & 0 \\ 0 & 0 & 2G_{12} \end{bmatrix} \quad \mathbf{L}_2 = \begin{bmatrix} G_{23} & 0 \\ 0 & G_{13} \end{bmatrix} \quad \mathbf{Q} = \begin{bmatrix} 1 & 0 & 0 \\ 0 & 1 & 0 \\ 0 & 0 & 2 \end{bmatrix}$$

The coordinate changes (3.46) and (3.47) for strain and stress, respectively, lead to:

$$\mathbf{R}_1^{-1} \begin{bmatrix} \sigma_x \\ \sigma_y \\ \sigma_{xy} \end{bmatrix} = \mathbf{Q}\mathbf{L}_1\mathbf{R}_1^{-1} \begin{bmatrix} \varepsilon_x \\ \varepsilon_y \\ \frac{\gamma_{xy}}{2} \end{bmatrix} \quad \mathbf{R}_2^{-1} \begin{bmatrix} \sigma_{yz} \\ \sigma_{xz} \end{bmatrix} = \mathbf{L}_2\mathbf{R}_2^{-1} \begin{bmatrix} \gamma_{yz} \\ \gamma_{xz} \end{bmatrix}$$

and it follows that:

$$\begin{bmatrix} \sigma_x \\ \sigma_y \\ \sigma_{xy} \end{bmatrix} = \mathbf{R}_1\mathbf{Q}\mathbf{L}_1\mathbf{R}_1^{-1}\mathbf{Q}^{-1} \begin{bmatrix} \varepsilon_x \\ \varepsilon_y \\ \gamma_{xy} \end{bmatrix} \quad (3.51)$$

$$\begin{bmatrix} \sigma_{yz} \\ \sigma_{xz} \end{bmatrix} = \mathbf{R}_2\mathbf{L}_2\mathbf{R}_2^{-1} \begin{bmatrix} \gamma_{yz} \\ \gamma_{xz} \end{bmatrix} \quad (3.52)$$

Compacting in a block-partitioned matrix form (3.51) and (3.52), gives :

$$\begin{bmatrix} \sigma_x \\ \sigma_y \\ \sigma_{xy} \\ - \\ \sigma_{yz} \\ \sigma_{xz} \end{bmatrix} = \begin{bmatrix} \mathbf{R}_1\mathbf{Q}\mathbf{L}_1\mathbf{R}_1^{-1}\mathbf{Q}^{-1} & | & \mathbf{0} \\ - & & - \\ \mathbf{0} & | & \mathbf{R}_2\mathbf{L}_2\mathbf{R}_2^{-1} \end{bmatrix} \begin{bmatrix} \varepsilon_x \\ \varepsilon_y \\ \gamma_{xy} \\ - \\ \gamma_{yz} \\ \gamma_{xz} \end{bmatrix}$$

The matrix:

$$\tilde{\mathbf{C}} = \begin{bmatrix} \mathbf{R}_1\mathbf{Q}\mathbf{L}_1\mathbf{R}_1^{-1}\mathbf{Q}^{-1} & | & \mathbf{0} \\ - & & - \\ \mathbf{0} & | & \mathbf{R}_2\mathbf{L}_2\mathbf{R}_2^{-1} \end{bmatrix} \quad (3.53)$$

is the so-called transformed reduced stiffness matrix.

3.7 Analysis of laminated composites

Generally, a composite material structure, a laminate, consists of several stacked unidirectional composite laminae or plies arranged in various orientations respect to the laminate reference system. This section presents the classic theory of laminated plates.

We consider a plate $\Omega \subset \mathbb{R}^3$ as a three dimensional domain such that $\Omega = [-a/2; a/2] \times [-b/2; b/2] \times [-t/2; t/2]$ where a , b , t are the length, the width and the height of the plate respectively. In addition we assume that the laminate thickness is small compared to its lateral dimensions and the following statements hold:

- a line initially straight and orthogonal to the middle surface of the plate remains straight as the plate deforms, this implies, from experimental evidence, that γ_{yz} and γ_{xz} are constant through the thickness;
- the lengths of the middle surfaces sides remain constant; this implies that $\varepsilon_{zz} = 0$.

3.7.1 Plate kinematics

The displacements at every point of the plate is described by the following vector field:

$$u_x(x, y, z) = u_x^0(x, y) - z\phi_x(x, y) \quad (3.54)$$

$$u_y(x, y, z) = u_y^0(x, y) - z\phi_y(x, y) \quad (3.55)$$

$$u_z(x, y, z) = u_z^0(x, y) \quad (3.56)$$

where, u_x^0 , u_y^0 and u_z^0 are the displacements of the middle surface, ϕ_x and ϕ_y are rotations (measured counter-clockwise) of the surfaces normal to the middle surface.

Strains can be evaluated by applying (3.3):

$$\varepsilon_x = \frac{\partial u_x}{\partial x} = \frac{\partial u_x^0}{\partial x} - z \frac{\partial \phi_x}{\partial x} \quad (3.57)$$

$$\varepsilon_y = \frac{\partial u_y}{\partial y} = \frac{\partial u_y^0}{\partial y} - z \frac{\partial \phi_y}{\partial y} \quad (3.58)$$

$$\gamma_{xy} = \frac{\partial u_x}{\partial y} + \frac{\partial u_y}{\partial x} = \frac{\partial u_x^0}{\partial y} + \frac{\partial u_y^0}{\partial x} - z \left(\frac{\partial \phi_x}{\partial y} + \frac{\partial \phi_y}{\partial x} \right) \quad (3.59)$$

$$\gamma_{yz} = \frac{\partial u_y}{\partial z} + \frac{\partial u_z}{\partial y} = -\phi_y + \frac{\partial u_z^0}{\partial y} \quad (3.60)$$

$$\gamma_{xz} = \frac{\partial u_x}{\partial z} + \frac{\partial u_z}{\partial x} = -\phi_x + \frac{\partial u_z^0}{\partial x} \quad (3.61)$$

Because of the assumption of thin laminate and neglecting the shear deformations, equations (3.60) and (3.61) give:

$$\phi_y = \frac{\partial u_z^0}{\partial y}$$

$$\phi_x = \frac{\partial u_z^0}{\partial x}$$

The curvatures of the plate due to bending and twisting are given by:

$$\kappa_x = -\frac{\partial \phi_x}{\partial x}$$

$$\kappa_y = -\frac{\partial \phi_y}{\partial y}$$

$$\kappa_{xy} = -\left(\frac{\partial \phi_x}{\partial y} + \frac{\partial \phi_y}{\partial x} \right)$$

Rearranging equations (3.57), (3.58) and (3.59) we obtain:

$$\varepsilon_x = \varepsilon_x^0 + z\kappa_x$$

$$\varepsilon_y = \varepsilon_y^0 + z\kappa_y$$

$$\gamma_{xy} = \gamma_{xy}^0 + z\kappa_{xy}$$

where

$$\varepsilon_x^0 = \frac{\partial u_x^0}{\partial x} \quad \varepsilon_y^0 = \frac{\partial u_y^0}{\partial y} \quad \gamma_{xy}^0 = \frac{\partial u_x^0}{\partial y} + \frac{\partial u_y^0}{\partial x}$$

These expressions compacted in vector form result:

$$\begin{bmatrix} \varepsilon_x \\ \varepsilon_y \\ \gamma_{xy} \end{bmatrix} = \begin{bmatrix} \varepsilon_x^0 \\ \varepsilon_y^0 \\ \gamma_{xy}^0 \end{bmatrix} + z \begin{bmatrix} \kappa_x \\ \kappa_y \\ \kappa_{xy} \end{bmatrix} \quad (3.62)$$

3.7.2 Plate equilibrium

Integrating the stresses over the thickness of laminate we obtain:

$$\begin{bmatrix} N_x \\ N_y \\ N_{xy} \end{bmatrix} = \int_{-t/2}^{t/2} \begin{bmatrix} \sigma_x \\ \sigma_y \\ \sigma_{xy} \end{bmatrix} dz \quad (3.63)$$

$$\begin{bmatrix} N_{yz} \\ N_{xz} \end{bmatrix} = \int_{-t/2}^{t/2} \begin{bmatrix} \sigma_{yz} \\ \sigma_{xz} \end{bmatrix} dz \quad (3.64)$$

$$\begin{bmatrix} M_x \\ M_y \\ M_{xy} \end{bmatrix} = \int_{-t/2}^{t/2} \begin{bmatrix} \sigma_x \\ \sigma_y \\ \sigma_{xy} \end{bmatrix} z dz \quad (3.65)$$

Where, N_x , N_y are the tensile forces, N_{xy} , N_{xz} and N_{yz} are the shear forces, M_x , M_y and M_{xy} are the moments, all of these per unit length, applied along a plate element boundary.

Partitioning the thickness of a N plies laminate,

$$[-t/2, t/2] = \bigcup_{k=1}^N [-t_k/2, t_k/2]$$

we can write the equilibrium equations (3.63), (3.64) and (3.65) applied to each ply thickness $t_k \forall k = 1, 2, \dots, N$ as:

$$\begin{bmatrix} N_x \\ N_y \\ N_{xy} \end{bmatrix} = \sum_{k=1}^N \int_{-t_k/2}^{t_k/2} \begin{bmatrix} \sigma_x \\ \sigma_y \\ \sigma_{xy} \end{bmatrix}_k dz \quad (3.66)$$

$$\begin{bmatrix} N_{yz} \\ N_{xz} \end{bmatrix} = \sum_{k=1}^N \int_{-t_k/2}^{t_k/2} \begin{bmatrix} \sigma_{yz} \\ \sigma_{xz} \end{bmatrix}_k dz \quad (3.67)$$

$$\begin{bmatrix} M_x \\ M_y \\ M_{xy} \end{bmatrix} = \sum_{k=1}^N \int_{-t_k/2}^{t_k/2} \begin{bmatrix} \sigma_x \\ \sigma_y \\ \sigma_{xy} \end{bmatrix}_k z dz \quad (3.68)$$

3.7.3 Constitutive equation

The last step consists of putting together kinematic and equilibrium equations to combine applied loads and strains.

Substituting the constitutive equations (3.51) and (3.52) into (3.66), (3.67) and (3.68) we have:

$$\begin{bmatrix} N_x \\ N_y \\ N_{xy} \end{bmatrix} = \sum_{k=1}^N \int_{-t_k/2}^{t_k/2} [\mathbf{R}_1 \mathbf{Q} \mathbf{L}_1 \mathbf{R}_1^{-1} \mathbf{Q}^{-1}]_k \begin{bmatrix} \varepsilon_x \\ \varepsilon_y \\ \gamma_{xy} \end{bmatrix}_k dz \quad (3.69)$$

$$\begin{bmatrix} N_{yz} \\ N_{xz} \end{bmatrix} = \sum_{k=1}^N \int_{-t_k/2}^{t_k/2} [\mathbf{R}_2 \mathbf{L}_2 \mathbf{R}_2^{-1}]_k \begin{bmatrix} \gamma_{yz} \\ \gamma_{xz} \end{bmatrix}_k dz \quad (3.70)$$

$$\begin{bmatrix} M_x \\ M_y \\ M_{xy} \end{bmatrix} = \sum_{k=1}^N \int_{-t_k/2}^{t_k/2} [\mathbf{R}_1 \mathbf{Q} \mathbf{L}_1 \mathbf{R}_1^{-1} \mathbf{Q}^{-1}]_k \begin{bmatrix} \varepsilon_x \\ \varepsilon_y \\ \gamma_{xy} \end{bmatrix}_k z dz \quad (3.71)$$

Using (3.62), the previous equations become:

$$\begin{aligned} \begin{bmatrix} N_x \\ N_y \\ N_{xy} \end{bmatrix} &= \sum_{k=1}^N \int_{-t_k/2}^{t_k/2} [\mathbf{R}_1 \mathbf{Q} \mathbf{L}_1 \mathbf{R}_1^{-1} \mathbf{Q}^{-1}]_k \begin{bmatrix} \varepsilon_x^0 \\ \varepsilon_y^0 \\ \gamma_{xy}^0 \end{bmatrix}_k dz + \\ &+ \sum_{k=1}^N \int_{-t_k/2}^{t_k/2} [\mathbf{R}_1 \mathbf{Q} \mathbf{L}_1 \mathbf{R}_1^{-1} \mathbf{Q}^{-1}]_k \begin{bmatrix} \kappa_x \\ \kappa_y \\ \kappa_{xy} \end{bmatrix}_k z dz \end{aligned} \quad (3.72)$$

$$\begin{bmatrix} N_{yz} \\ N_{xz} \end{bmatrix} = \sum_{k=1}^N \int_{-t_k/2}^{t_k/2} [\mathbf{R}_2 \mathbf{L}_2 \mathbf{R}_2^{-1}]_k \begin{bmatrix} \gamma_{yz} \\ \gamma_{xz} \end{bmatrix}_k dz \quad (3.73)$$

$$\begin{aligned} \begin{bmatrix} M_x \\ M_y \\ M_{xy} \end{bmatrix} &= \sum_{k=1}^N \int_{-t_k/2}^{t_k/2} [\mathbf{R}_1 \mathbf{Q} \mathbf{L}_1 \mathbf{R}_1^{-1} \mathbf{Q}^{-1}]_k \begin{bmatrix} \varepsilon_x^0 \\ \varepsilon_y^0 \\ \gamma_{xy}^0 \end{bmatrix}_k z dz + \\ &+ \sum_{k=1}^N \int_{-t_k/2}^{t_k/2} [\mathbf{R}_1 \mathbf{Q} \mathbf{L}_1 \mathbf{R}_1^{-1} \mathbf{Q}^{-1}]_k \begin{bmatrix} \kappa_x \\ \kappa_y \\ \kappa_{xy} \end{bmatrix}_k z^2 dz \end{aligned} \quad (3.74)$$

In the adopted displacement field (Equations (3.54), (3.55) and (3.56)) the derived quantities, referred to the middle plane, ε_x^0 , ε_y^0 , γ_{xy}^0 , γ_{yz}^0 , κ_x , κ_y and κ_{xy} are independent of z . Moreover these quantities are common to all laminae and are k independent. With the assumption that γ_{yz} and γ_{xz} are constant along the laminate thickness, they are independent of z .

Furthermore, γ_{yx} and γ_{xz} are constant for all laminae, hence independent of k and the (3.75) holds:

$$\begin{bmatrix} \varepsilon_x^0 \\ \varepsilon_y^0 \\ \gamma_{xy}^0 \end{bmatrix}_k \mapsto \begin{bmatrix} \varepsilon_x^0 \\ \varepsilon_y^0 \\ \gamma_{xy}^0 \end{bmatrix} \quad \begin{bmatrix} \kappa_x \\ \kappa_y \\ \kappa_{xy} \end{bmatrix}_k \mapsto \begin{bmatrix} \kappa_x \\ \kappa_y \\ \kappa_{xy} \end{bmatrix} \quad \begin{bmatrix} \gamma_{yz} \\ \gamma_{xz} \end{bmatrix}_k \mapsto \begin{bmatrix} \gamma_{yz} \\ \gamma_{xz} \end{bmatrix} \quad \forall k = 1, \dots, N \quad (3.75)$$

As a consequence extracting from integrals the k-vector of (3.72), (3.73) and (3.74) the equations simplify as follows:

$$\begin{aligned} \begin{bmatrix} N_x \\ N_y \\ N_{xy} \end{bmatrix} &= \begin{bmatrix} \varepsilon_x^0 \\ \varepsilon_y^0 \\ \gamma_{xy}^0 \end{bmatrix} \sum_{k=1}^N \int_{-t_k/2}^{t_k/2} [\mathbf{R}_1 \mathbf{Q} \mathbf{L}_1 \mathbf{R}_1^{-1} \mathbf{Q}^{-1}]_k dz + \\ &+ \begin{bmatrix} \kappa_x \\ \kappa_y \\ \kappa_{xy} \end{bmatrix} \sum_{k=1}^N \int_{-t_k/2}^{t_k/2} [\mathbf{R}_1 \mathbf{Q} \mathbf{L}_1 \mathbf{R}_1^{-1} \mathbf{Q}^{-1}]_k z dz \end{aligned} \quad (3.76)$$

$$\begin{bmatrix} N_{yz} \\ N_{xz} \end{bmatrix} = \begin{bmatrix} \gamma_{yz} \\ \gamma_{xz} \end{bmatrix} \sum_{k=1}^N \int_{-t_k/2}^{t_k/2} [\mathbf{R}_2 \mathbf{L}_2 \mathbf{R}_2^{-1}]_k dz \quad (3.77)$$

$$\begin{aligned} \begin{bmatrix} M_x \\ M_y \\ M_{xy} \end{bmatrix} &= \begin{bmatrix} \varepsilon_x^0 \\ \varepsilon_y^0 \\ \gamma_{xy}^0 \end{bmatrix} \sum_{k=1}^N \int_{-t_k/2}^{t_k/2} [\mathbf{R}_1 \mathbf{Q} \mathbf{L}_1 \mathbf{R}_1^{-1} \mathbf{Q}^{-1}]_k z dz + \\ &+ \begin{bmatrix} \kappa_x \\ \kappa_y \\ \kappa_{xy} \end{bmatrix} \sum_{k=1}^N \int_{-t_k/2}^{t_k/2} [\mathbf{R}_1 \mathbf{Q} \mathbf{L}_1 \mathbf{R}_1^{-1} \mathbf{Q}^{-1}]_k z^2 dz \end{aligned} \quad (3.78)$$

Finally, defining the matrices:

$$\begin{aligned}\mathbf{A} &= \sum_{k=1}^N \int_{-t_k/2}^{t_k/2} [\mathbf{R}_1 \mathbf{Q} \mathbf{L}_1 \mathbf{R}_1^{-1} \mathbf{Q}^{-1}]_k dz \\ \mathbf{B} &= \sum_{k=1}^N \int_{-t_k/2}^{t_k/2} [\mathbf{R}_1 \mathbf{Q} \mathbf{L}_1 \mathbf{R}_1^{-1} \mathbf{Q}^{-1}]_k z dz \\ \mathbf{D} &= \sum_{k=1}^N \int_{-t_k/2}^{t_k/2} [\mathbf{R}_1 \mathbf{Q} \mathbf{L}_1 \mathbf{R}_1^{-1} \mathbf{Q}^{-1}]_k z^2 dz \\ \mathbf{P} &= \sum_{k=1}^N \int_{-t_k/2}^{t_k/2} [\mathbf{R}_2 \mathbf{L}_2 \mathbf{R}_2^{-1}]_k dz\end{aligned}$$

it is possible to gather (3.76), (3.77) and (3.78) in a block-partitioned matrix form:

$$\begin{bmatrix} N_x \\ N_y \\ N_{xy} \\ - \\ M_x \\ M_y \\ M_{xy} \\ - \\ V_x \\ V_y \end{bmatrix} = \begin{bmatrix} \mathbf{A} & \mathbf{B} & \mathbf{0} \\ - & - & - \\ \mathbf{B} & \mathbf{D} & \mathbf{0} \\ - & - & - \\ \mathbf{0} & \mathbf{0} & \mathbf{P} \end{bmatrix} = \mathbf{C}_\Omega \begin{bmatrix} \varepsilon_x^0 \\ \varepsilon_y^0 \\ \gamma_{xy}^0 \\ - \\ \kappa_x \\ \kappa_y \\ \kappa_{xy} \\ - \\ \gamma_{yz} \\ \gamma_{xz} \end{bmatrix} \quad (3.79)$$

where:

- \mathbf{A} , is the *in-plane stiffness matrix*;
- \mathbf{B} , is the *bending-extension coupling stiffness matrix*;
- \mathbf{D} , is the *bending stiffness matrix*;
- \mathbf{P} , is the *transverse shear stiffness matrix*;
- \mathbf{C}_Ω , is the *plate stiffness matrix*.

Inverting the constitutive equation (3.79) expressed in terms of stiffness matrices, we can write the constitutive equation in terms of compliance ma-

trices as:

$$\begin{bmatrix} \varepsilon_x^0 \\ \varepsilon_y^0 \\ \gamma_{xy}^0 \\ - \\ \kappa_x \\ \kappa_y \\ \kappa_{xy} \\ - \\ \gamma_{yz} \\ \gamma_{xz} \end{bmatrix} = \begin{bmatrix} \boldsymbol{\alpha} & | & \boldsymbol{\beta} & | & \mathbf{0} \\ - & & - & & - \\ \boldsymbol{\beta} & | & \boldsymbol{\delta} & | & \mathbf{0} \\ - & & - & & - \\ \mathbf{0} & | & \mathbf{0} & | & \boldsymbol{\pi} \end{bmatrix} \begin{bmatrix} N_x \\ N_y \\ N_{xy} \\ - \\ M_x \\ M_y \\ M_{xy} \\ - \\ V_x \\ V_y \end{bmatrix} = \mathbf{S}_\Omega \begin{bmatrix} N_x \\ N_y \\ N_{xy} \\ - \\ M_x \\ M_y \\ M_{xy} \\ - \\ V_x \\ V_y \end{bmatrix}$$

where:

- $\boldsymbol{\alpha}$, is the *in-plane compliance matrix*;
- $\boldsymbol{\beta}$, is the *bending-extension coupling compliance matrix*;
- $\boldsymbol{\delta}$, is the *bending compliance matrix*;
- $\boldsymbol{\pi}$, is the *transverse shear compliance matrix*;
- \mathbf{S}_Ω , is the *plate compliance matrix*.

We reviewed the above concepts on micromechanics aspects of composites, elastic constants of a single lamina and the analysis of laminated composites for several reasons. GFRP composites use different resins and several glass fibres formats suitably combined to achieve the specific fibre volume fractions requested by the application. The knowledge of elastic constants for the single lamina and the equivalent homogenised elastic constants of the laminate is of primary importance for the preliminary design of the experimental test and to define analytical or numerical models required for interpreting experimental results.

3.8 The Python module *cmplampy*

Python is a general-purpose, object-oriented scripting-programming language [62]. Python provides the possibility to create user-defined modules. A module can define functions, classes and variables in a self-contained package known as a namespace. In the module *cmplampy* we have implemented the following classes and functions:

- *MaterialProp* (class);
- *basePly* (class);
- *inLamPly* (class);
- *Laminate* (class);
- *ElConBase* (function);
- *ElConCSM* (function);

The *MaterialProp* class provides the data structure to define a general isotropic material. The *basePly* class defines the lamina properties in the material coordinate system, Figure 3.7, using fibre and matrix *MaterialProp* objects), the fibre specific mass, the function *ElConBase* or *ElConCSM* and the fibre fraction in terms of volume or mass. The class *inLamPly* compute the lamina's transformed reduced stiffness matrix, $\tilde{\mathbf{C}}$, Equation 3.53. The class *Laminate* stacks *inLamPly* lamina objects to build a laminate. A *Laminate* object implements the constitutive equations reported in 3.7.3. The function *ElConBase* actually implements the Equations 3.22 to 3.28 whereas *ElConCSM* use the equation of the semi-empirical Halpin-Tsai model. In the application examples, *ElConBase* and *ElConCSM*, used in *basePly*, contains the equations for the definition of lamina properties. However, another function that creates the same attributes for the object, e.g. using other author's formulations for calculating the lamina elastic constants, can initialize a *basePly* object. Furthermore, the use of other functions does not require changes to the module code.

Example 1

Given a laminate, the manufacturer provided the used brand and type of the resin and fibreglass, DERAKANE 411 resin and Vetrotex glass fibre, and the composition reported below:

$[(CSM^{600}/WR^{830}/CSM^{600})_2/CSM^{225}/WR^{500}/CSM^{225}]$, where

superscript indicates fabric specific mass in g m^{-2} . With the resin and the glass fibre mechanical properties, using the *cmplampy* module, we calculate the elastic modulus of the laminate as follows.

```

# imports functions and classes from the module cimplampy
import cimplampy

# create the resin material
derakane411 = MaterialProp (density=1120, elastic_mod=3200,\
                           shear_mod=1159, poisson_r=0.38, \
                           t_strength=90, c_strength=117,\
                           elongation=0.050)

# create the e-glass material (vetrotex)
e_glass = MaterialProp (density=2600, elastic_mod=72350, shear_mod=29650,\
                       poisson_r=0.22, t_strength=2400, c_strength=0,\
                       elongation=0.024)

# create the basic laminae
csm_600 = basePly('CSM600', e_glass, derakane411, 600, ElConCSM, Mf=0.30)
csm_225 = basePly('CSM225', e_glass, derakane411, 225, ElConCSM, Mf=0.30)
uni_415 = basePly('UND415', e_glass, derakane411, 415, ElConBase, Mf=0.45)
uni_250 = basePly('UND250', e_glass, derakane411, 250, ElConBase, Mf=0.45)

# create the laminate by stacking laminae with fibers in various orientation
lamin = Laminate('VALID_01', csm_225, 0)
lamin.addply(uni_250, 0)
lamin.addply(uni_250, 90)
lamin.addply(csm_225, 0)

for i in range(0,2):
    lamin.addply(csm_600, 0)
    lamin.addply(uni_415, 0)
    lamin.addply(uni_415, 90)
    lamin.addply(csm_600, 0)

# calculate matrices Eq. (3.75)
lamin.matx_lam()

```

The equivalent laminate modulus results, $E_x = 10\,472$ MPa, and it is in good agreement, with experimental results of tensile tests, performed in the Official Laboratory for Testing of Materials and Structures of the Polytechnic Department of Engineering and Architecture, and reported in the Certificate n.74/2017. The certificate exhibits an average modulus, for the specimens identified with B-T, equal to 10 602 MPa.

Example 2

Given a laminate manufactured with DERA KANE 411 resin and Vetrotex glass fibre, of unknown laminae composition, we perform loss on ignition test, to determine the textile-glass content, Figure 3.8. After this type of

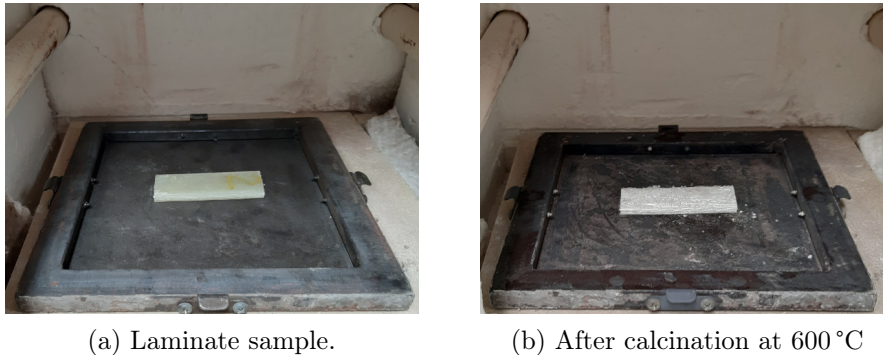


Figure 3.8: Loss on ignition test.

test, it is possible to observe the nature of the fabric present in each layer and, by weighting, to determine the fabric specific mass in g m^{-2} . The composition of the laminate results:

$[CSM^{225}/WR^{500}/CSM^{225}]_3$.

The fibre mass fraction, Equation 3.18, results $W_f = 0.473$. Then, using the custom module *cmplampy*:

```
import cmplampy
derakane411 = MaterialProp (density=1120, elastic_mod=3200,\
                           shear_mod=1159, poisson_r=0.38, \
                           t_strength=90, c_strength=117,\
                           elongation=0.050)

e_glass = MaterialProp (density=2600, elastic_mod=72350, shear_mod=29650,\
                        poisson_r=0.22, t_strength=2400, c_strength=0,\
                        elongation=0.024)

csm_225 = basePly('CSM225', e_glass, derakane411, 225, ElConCSM, Mf=0.473)
uni_250 = basePly('UND250', e_glass, derakane411, 250, ElConBase, Mf=0.473)

laminat = Laminat('VALID_02', csm_225, 0)
laminat.addply(uni_250, 0)
laminat.addply(uni_250, 90)
laminat.addply(csm_225, 0)
for i in range (0, 2, 1):
    laminat.addply(csm_225, 0)
    laminat.addply(uni_250, 0)
    laminat.addply(uni_250, 90)
    laminat.addply(csm_225, 0)

laminat.matx_lam()
```

we calculate the equivalent laminate modulus resulting in $E_x = 13\,744$ MPa.

The experimental values, acquired from two tensile tests we performed on this laminate, have an average value of 13 401 MPa. Therefore the theoretical and the experimental results show a good agreement.

Chapter 4

Testing of bulk adhesives

Standard test methods consider the adhesive in its in-situ or thin-film form. Therefore, required mechanical properties for stress analysis purposes when the adhesive needs to be modelled, for example using the finite element method, are not provided. An approach allowing to determine these properties uses 'bulk' adhesive tests. Currently, no official standard exists for bulk adhesive testing. However, since the selected adhesives are similar to plastic, many of the standards for plastics included in ASTM as well as in EN/ISO might be adapted to test the properties of bulk adhesives. In this chapter we describe materials, methodology and results of tests carried out on selected adhesives, considering the described approach.

4.1 Introduction

This chapter begins with a full description of materials and methods that were used throughout the manufacturing of the bulk specimens for tensile, compression and shear tests. Then a detailed description of the equipment and test set-up used to perform the tests is reported, and, finally, the experimental results are presented and discussed.

4.2 Materials and methods

4.2.1 Materials

Two adhesives have been selected for bulk tests. The first one, a Vinyl-ester Putty Adhesive Paste, hereinafter referred to as ADH1, has been provided through the courtesy of Carbon Compositi Srl ¹, the second, Adesilex PG1 (ADH2), through the courtesy of Mapei SpA ².

ADH1 has a vinyl-ester based formulation with fillers and additives that allow curing properly at temperatures starting from 5 to 6 °C. ADH1 was developed to join GFRP pipes with GFRP fittings. The manufacturer recommend the use of methyl ethyl ketone peroxide (MEKP) as initiator mixed 2% by volume with the adhesive. Currently Carbon Compositi is running an experimental campaign on this adhesive putty and other technical data will be available soon.

ADH2 is an epoxy-type, two-component, rapid-setting thixotropic adhesive for structural bonds. A typical application for this product is the structural reinforcement of beams by bonding composite material plates to concrete. According to the manufacturer's specifications the mixing ratio of component A to component B is 3:1 and the pot-life of mix is 35 min at 23 °C. Adesilex PG1 should be applied at least in thickness of 1 to 2 mm. The maximum layer thickness is 10 mm. Mechanical properties reported in the technical data sheet (<https://www.mapei.com/it/it/prodotti-e-soluzioni/prodotti/dettaglio/adesilex-pg1>) refers to tests conducted in accordance with European Codes.

4.2.2 Methods and procedures

The main objective of bulk adhesive specimen preparation is to obtain samples having mechanical properties similar to those of the adhesive layer in joints. Making of adhesive samples involves many technological problems indeed, [63]. Handling of high adhesion materials is difficult, prevent the air inclusion during mixing components is not straightforward and, due to different viscosity of adhesives, pouring or spreading adhesive into the mould requires manual dexterity, [64]. Furthermore the shrinkage and the heat

¹Carbon Compositi S.r.l., Via Zanon n.14/16, 33031 Basiliano (UD), Italy

²Mapei S.p.A., Via Cafiero n.22, 20158 Milano, Italy

generated in the cross-linking process, state that it is not possible to use one universal method for obtaining repeatable specimens. This section describes specimens geometry and adopted fabrication procedure. For each selected adhesive Table 4.1 reports the identification of specimens whose production was planned for the tensile, compression and shearing tests.

Table 4.1: Specimens identification

Adhesive	Tensile Test (ID)	Compression Test (ID)	Shear Test (ID)
ADH1	TI-1	CI-1	SI-1
	TI-2	CI-2	SI-2
	TI-3	CI-3	SI-3
	TI-4	CI-4	-
	TI-5	CI-5	-
	TI-6	-	-
ADH2	TII-1	CII-1	SII-1
	TII-2	CII-2	SII-2
	TII-3	CII-3	SII-3
	TII-4	CII-4	-
	TII-5	CII-5	-
	TII-6	-	-

For tensile test dog-bone shaped specimens were used according to the standard EN ISO 527-2 for the type 1B specimen (Figure 4.1).

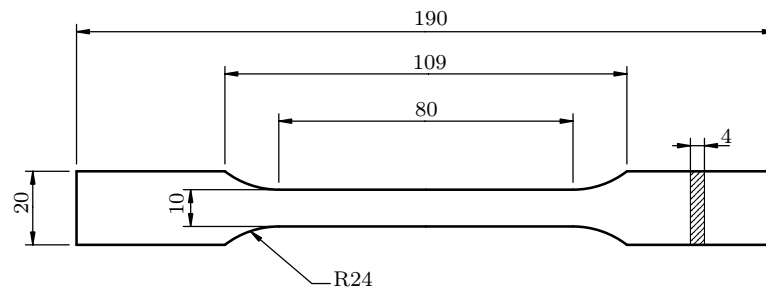


Figure 4.1: Tensile test, specimen dimensions type 1B of ISO 527-2 compliant.

To obtain dog-bone shape for the specimens, this shape was modelled with the open-source parametric 3D modeler FreeCAD. The shapes of five

samples were 3D printed using PLA filament (Polylactic acid) and fixed in a plastic container. Then the container was appropriately filled with the addition cure RTV Silicone R PRO 30 made by RESCHIMICA Srl. This silicone rubber has low shrink characteristics making it suitable for forming moulds with high dimensional accuracy. After curing at room temperature a five dogbone-shaped mould was obtained (Figure 4.2). Silicone mould prevent the adhesive from adhering to the mould surface. The upper face (cover) of the mould was obtained with a Poly(methyl methacrylate) (PMMA) 25 mm thick plate, interposing a Mylar film. As silicone, Mylar is a low surface energy material. In this manner no release agent was applied to the surface of the mould components avoiding any contamination of the adhesive. For each selected adhesive, groups of five samples were cast at once and, after curing, removed from the mould. An additional sample was made using the first preliminary mould version, hence six specimens for each selected adhesive were obtained (Figure 4.3). In this manner no milling or other types of mechanical processing are needed for shaping the samples. Each specimen were measured at three transversal sections for width, b , and thickness, h , using a digital caliper (Mitutoyo, Tokyo, Japan) to the nearest 0.01 mm. The three transversal sections were centred on the specimen length over an interval of 50 mm (gauge length). Mean value and standard deviation for measured dimensions are reported in Table 4.2. The standard deviation values show that the cross-section dimensions of each sample have small variations along its gauge length.

For compression test cylindrical specimens with an height/diameter ratio equal to 2 were used. This aspect ratio reduces the confinement effects of frictional force exerted by the machine platens during the test. The adhesive samples were formed adopting standard polypropylene syringes as mould (Figure 4.4) as in [63]. A further feature was added to this technique: the temperature monitoring of the adhesive.

A custom-made system composed by an aluminium/PLA sump and an aluminium sensor holder for a Pt100 class A probe were used. The mass of sump, probe and sensor holder results in 1.14 g that is lower than 2% of the total mass of the poured adhesive in a single mould. Room temperature and relative humidity were measured with DHT22 digital-output module with an accuracy of 2 to 5% for humidity over the 0 to 100% humidity range and $\pm 0.5^\circ\text{C}$ for temperature over the -40 to 80°C range. During the cross-linking reaction, the temperature of adhesive in one specimen of each group



Figure 4.2: Silicone mould of five dog-bone shaped tensile specimens.

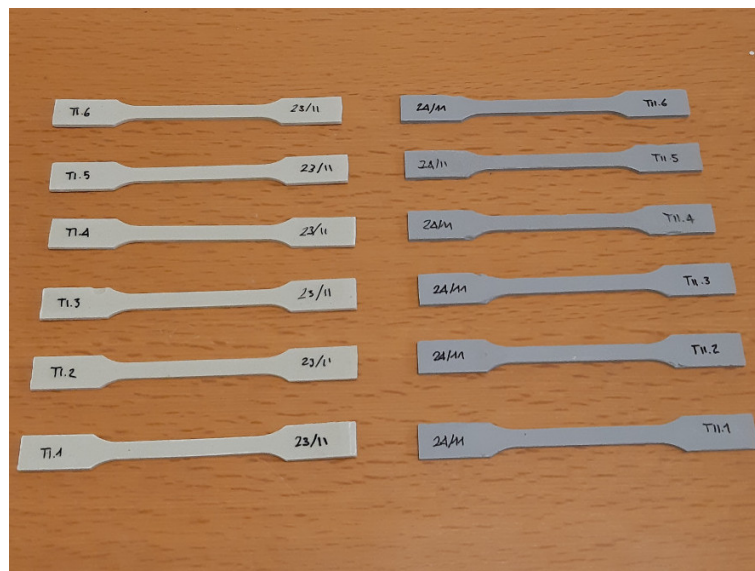


Figure 4.3: Tensile specimens of ADH1 (left-hand side) and of ADH2 (right-hand side).

Table 4.2: Tensile specimens, mean value and standard deviation of cross-section dimensions.

Specimen ID	b (mm)	σ_b (mm)	h (mm)	σ_h (mm)
TI-1	9.61	0.03	3.96	0.06
TI-2	9.63	0.08	3.78	0.01
TI-3	9.59	0.01	3.82	0.08
TI-4	9.68	0.01	3.82	0.08
TI-5	9.57	0.02	3.94	0.01
TI-6	9.57	0.02	3.88	0.03
TII-1	9.90	0.01	3.77	0.03
TII-2	9.77	0.01	3.81	0.04
TII-3	9.86	0.01	3.75	0.06
TII-4	9.79	0.03	3.82	0.03
TII-5	9.85	0.01	3.62	0.02
TII-6	9.81	0.01	4.20	0.05

and room parameters were acquired (Figure 4.5).

In order to have the specimen ends smooth, flat and parallel each other and perpendicular to the longitudinal axis of the specimen, cylinder of adhesive, de-moulded from the syringes, were lathe cut with great care. Following, the diameter, D (at three cross sections), height, h and mass, m , were measured. Mean value and standard deviation for measured data are reported in Table 4.3. The standard deviation values, not greater than 0.08 mm, show small variations of the cross-section dimensions along the samples height. Differences in density (ρ) values, in particular for ADH2 samples, reveal the presence of unwanted entrapped air in the specimens.

For shear test a novel technique has been proposed and more details on this will be given in the next paragraph. Shear test uses a plane rectangular specimen of adhesive, Figure 4.7. The specimens was manufactured with the same technique used for the tensile samples, using silicone moulds. The overall dimensions of specimen were recorded as well as the thickness, measured at upper and lower boundary of the specimen (4.4).

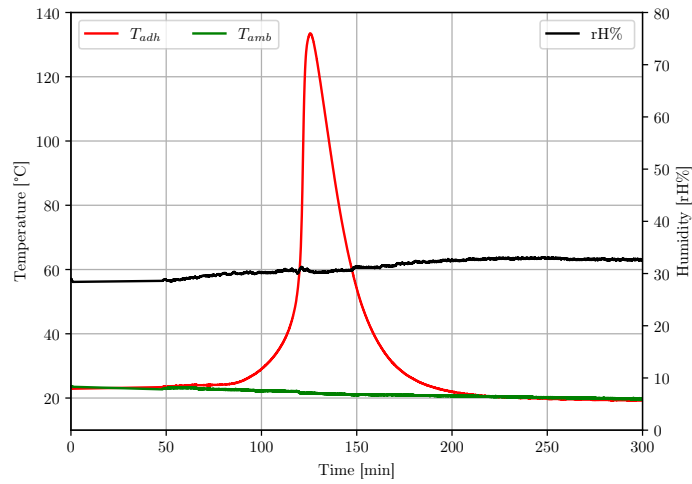
Tensile, compression and shear bulk adhesive samples were all manufactured and cured at 20 to 23 °C.



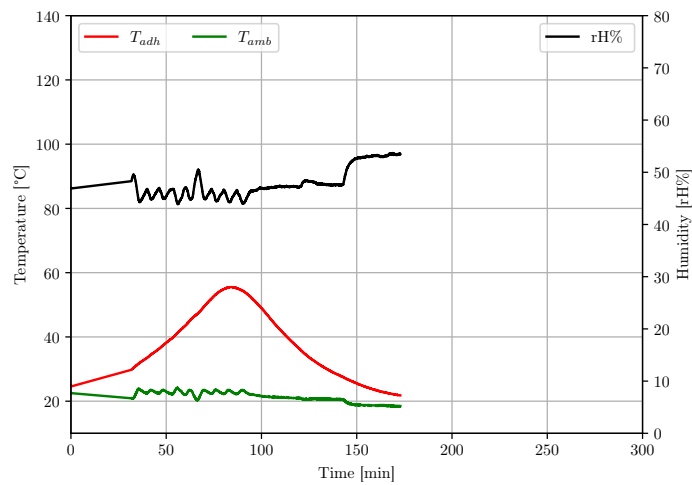
Figure 4.4: Mould for compression specimens filled with ADH1.

Table 4.3: Compression specimens, mean value and standard deviation of cross-section dimensions, mass value and computed density.

Sample ID	D (mm)	σ_D (mm)	h (mm)	σ_h (mm)	m (kg)	ρ (kg m ⁻³)
CI-1	28.67	0.04	57.41	0.04	33.5e-3	903.8
CI-2	28.73	0.07	57.93	0.04	34.0e-3	905.8
CI-3	28.71	0.05	57.34	0.02	33.0e-3	913.0
CI-4	28.63	0.01	58.09	0.03	33.7e-3	900.9
CI-5	28.69	0.04	57.98	0.03	34.0e-3	906.9
CII-1	29.13	0.08	58.61	0.02	65.0e-3	1664.5
CII-2	29.18	0.03	57.65	0.02	65.6e-3	1701.1
CII-3	29.17	0.03	57.76	0.04	65.5e-3	1697.0
CII-4	29.18	0.01	57.76	0.02	64.2e-3	1662.1
CII-5	29.19	0.08	57.88	0.03	66.2e-3	1708.6



(a) Adhesive type ADH1



(b) Adhesive type ADH2

Figure 4.5: Temperature-time profiles recorded in the centre of the sample inside the mould.

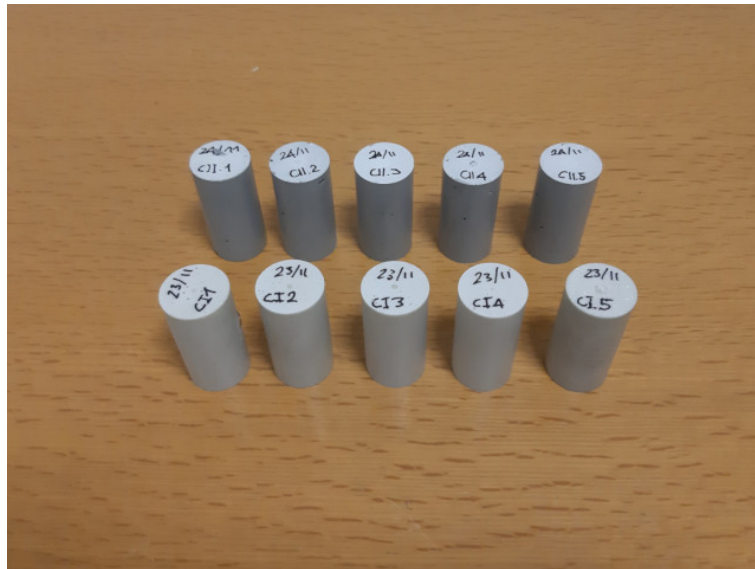


Figure 4.6: Compression specimens of ADH1, in the lower part, and of ADH2, at the top.

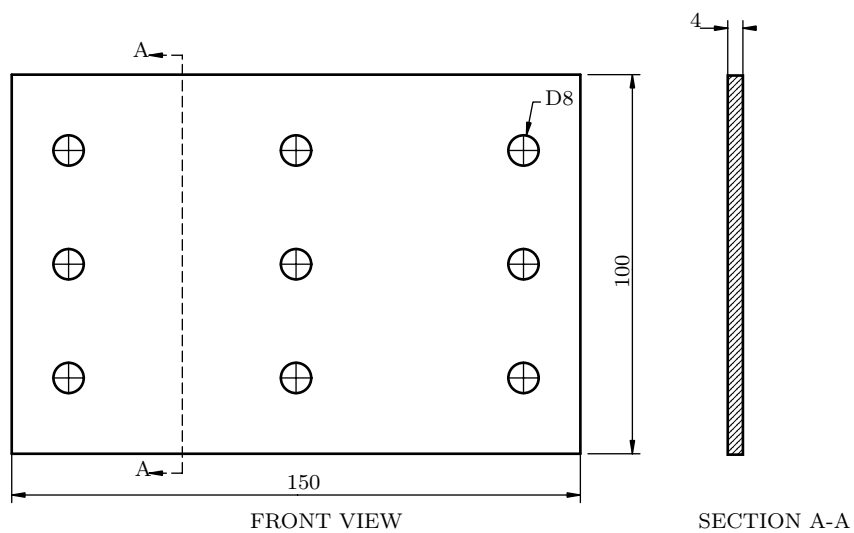


Figure 4.7: Shear test, specimen dimensions.

Table 4.4: Shear specimens, mean value and standard deviation of dimensions, mass value and computed density.

Sample ID	h (mm)	σ_h (mm)	b (mm)	σ_b (mm)	t (mm)	σ_t (mm)	m (kg)	ρ (kg m ⁻³)
SI-1	98.66	0.08	148.42	0.06	4.09	0.05	53.1	915.9
SI-2	98.76	0.10	148.53	0.01	4.16	0.10	54.9	930.4
SI-3	99.17	0.15	148.55	0.08	4.00	0.23	52.5	920.6
SII-1	99.61	0.08	150.10	0.12	4.32	0.04	108.8	1740.8
SII-2	99.61	0.07	149.85	0.01	4.45	0.21	108.8	1692.8
SII-3	99.43	0.08	149.67	0.04	4.43	0.27	105.9	1658.4

4.2.3 Equipment

All the tests were conducted using the 500 kN multipurpose servo-hydraulic testing system MTS 810 (MTS Systems Corporation). In tensile tests although the MTS 810 has two hydraulic wedges to hold the specimen ends, a specifically designed mechanical gripping system was used. Figure 4.8 shows the grips parts. Parts of the clamp were manufactured by laser cutting a S275J0 grade structural steel plate. This design offers both geometrical and friction gripping. The central plate has a cropped shape of the specimen grip end provides the geometrical gripping. Friction gripping is obtained with the application of 80-mesh red-brown corundum abrasive sand, over the shape corresponding to grip section of the dog-bone specimen. In this application first, the grip surface was degreased, sandblasted and further wiped and degreased with acetone, then a thin layer of epoxy resin was applied and finally the corundum was distributed by sprinkling it over the fresh resin. When the external plates are fasten by bolting with the central plate and gripping end of specimen, geometrical and friction gripping keep specimen ends from slipping or breaking in-between the grips. The tightening of all bolts was performed at 9 N m with a 1/4" torque wrench Wurth with a range of 4 N m to 20 N m . The MTS 810's force transducer can be used with two different full-scale ranges of 500 kN or 50 kN. Both are not suitable for measuring the estimated forces in this application. Therefore an additional force measuring device with a range up to 5 kN was applied. Two strain-gauge-based HBM DD1 displacement and strain transducer were used to measure longitudi-

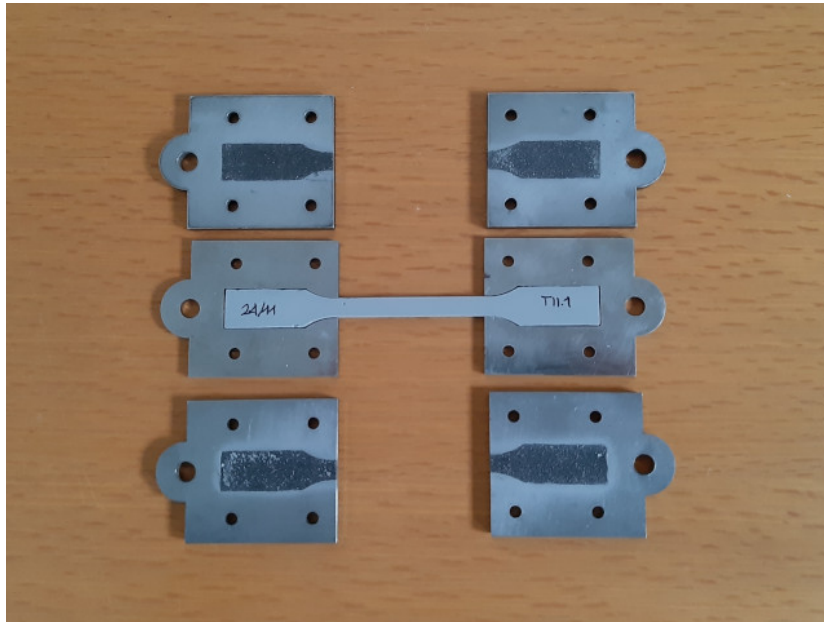


Figure 4.8: Parts of gripping system designed for tensile test

nal and transverse deformation. DD1 measures displacements in a range of ± 2.5 mm very accurately, offering an accuracy class of 0.1. The support we developed for the purpose, enables the two DD1 transducers to be simultaneously fixed to the tensile specimen. The gauge length was 50 mm and equal to sample width, for longitudinal and transverse deformation, respectively. Figure 4.9 shows the experimental setup for tensile test and Figure 4.10 details the custom-made DD1s support frame.

The specimens in compression test were positioned in between the compression platen of the MTS 810. The upper platen is on a spherical seat for improved alignment and ensuring even pressure across the entire surface of the specimen. The chosen height/diameter aspect ratio of specimens reduces the confinement effects of frictional force exerted by the machine platen during the test. To assess whether this reduction is effective or not for each selected adhesive, two types of lubricant, PTFE based and silicone based, were spread on the machine platen surface for the second and third and for the fourth and fifth specimens, respectively. The longitudinal force was measured with the MTS 810's at full-scale range of 500 kN. The longitudinal displacement was measured with three linear variable differential transformer (LVDT) transducers, type W10TK by HBM. The transducers

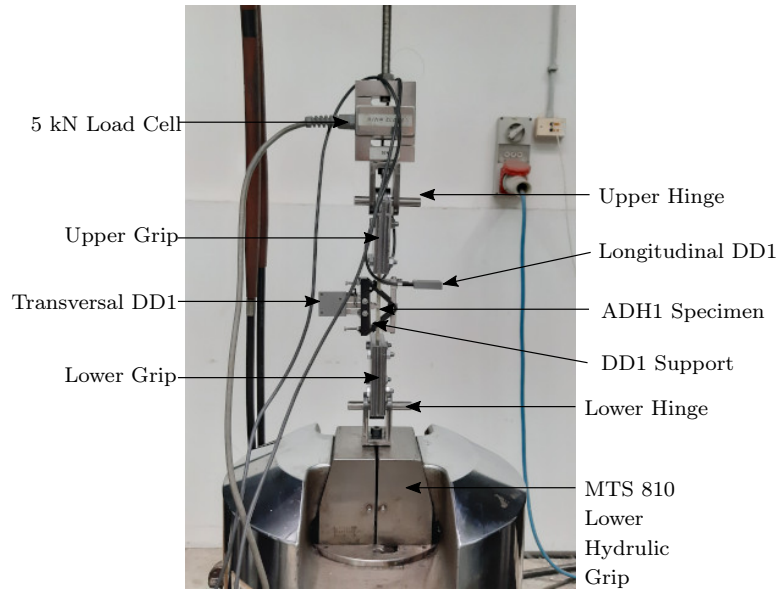


Figure 4.9: Tensile test setup.

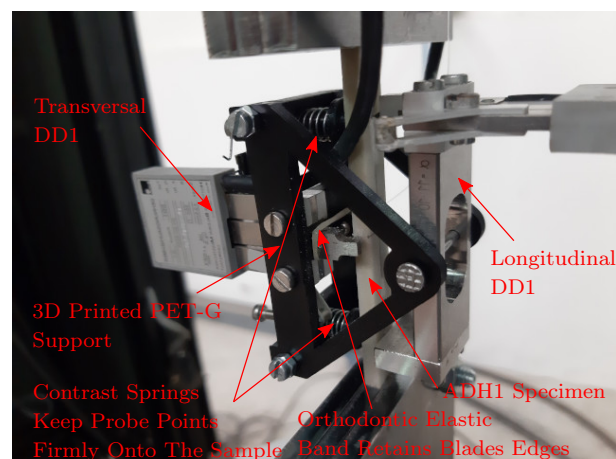


Figure 4.10: Custom made DD1s support, detail of 3D printed part (black PET-G).

were positioned 120° from each other. In addition to the measurement of the longitudinal force and displacement, simultaneous strain measurement were performed using a strain-gauge. Figure 4.11 shows the experimental setup for compression test.

The designed and fabricated fixture for shear test is a variation on the classic apparatus proposed in the ASTM D4255/4255M *Standard Test Method for In-Plane Shear Properties of Polymer Matrix Composite Materials by the Rail Shear Method*. The design has taken into account both the improvements proposed by De Baere et. al in [65, 66] and by Mohseni in [67]. The rectangular adhesive specimen of Figure 4.7 is clamped by three coupled (grips) bars parallel each other (Figure 4.12) and, during the test, the central couple of bars has a relative vertical motion with respect to the two outer couples. Therefore a state of shear stress is induced in the specimen. The shear deformation was measured using four strain-gauges appropriately placed on the specimen surface. Figure 4.13 presents the experimental set up for shear test. The test specimen is held such that slip relative to the grips is prevented. This gripping system not cause premature fracture or crushing of the specimen in the grips. The testing apparatus can be used with or without the hinge joints. In the latter case, gripping the apparatus ends directly into hydraulic wedges, cyclic tests can be performed.

As reported before the tests were conducted using the 500 kN multipurpose servo-hydraulic testing system MTS 810 (MTS Systems Corporation). A constant rate of cross-head movement control was applied for all configurations experimental tests. In tensile test the machine was set up for 0.005 mm s^{-1} which lead, for sample length equal to 80 mm, to an axial strain rate of $62.5 \times 10^{-6} \text{ s}^{-1}$. In compression and shear test the rate of displacement was set up to 0.004 mm s^{-1} for an axial strain rate of $69.0 \times 10^{-6} \text{ s}^{-1}$ and for a shear deformation rate of $65.0 \times 10^{-6} \text{ s}^{-1}$ respectively. Additional load cell and DD1 transducers in tensile test and LDTV transducers in compression test were connected to an HBM MGC amplifier. In the compression test as well as in the shear test the strain gauges were connected to National Instrument NI9237 amplifier module. This module was configured for a quarter bridge I using a NI9945 (350Ω) completion resistor. Provided data from the MGC through an RS-232 interface, from the NI9237 module by USB interface and from MTS 810 via Ethernet were acquired, plotted real-time and saved in a personal computer running National Instruments LabView Virtual instrument software.

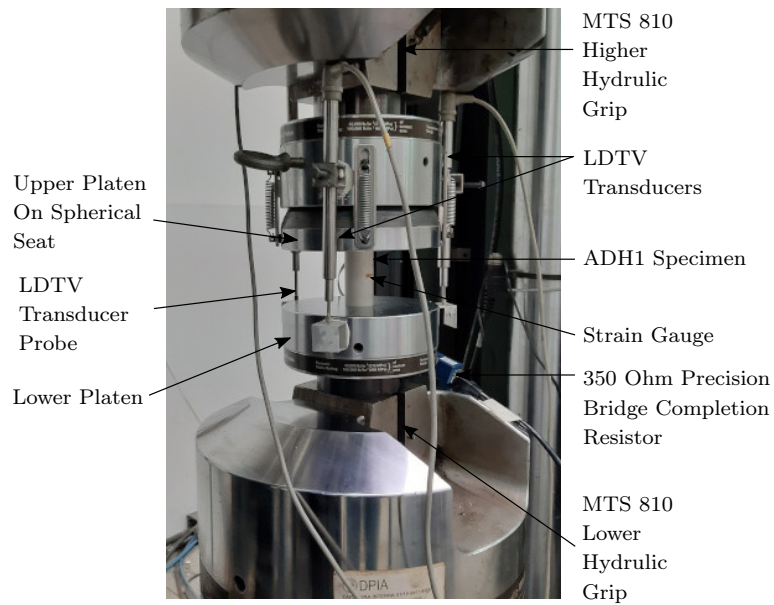
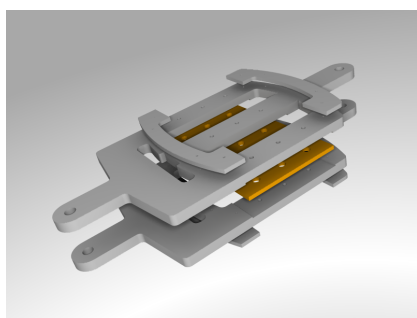
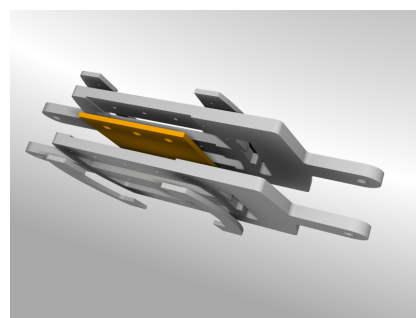


Figure 4.11: Compression test setup.



(a)



(b)

Figure 4.12: Prototype of shear fixture, parts of 3D FreeCAD model rendered with open source software POV-Ray.

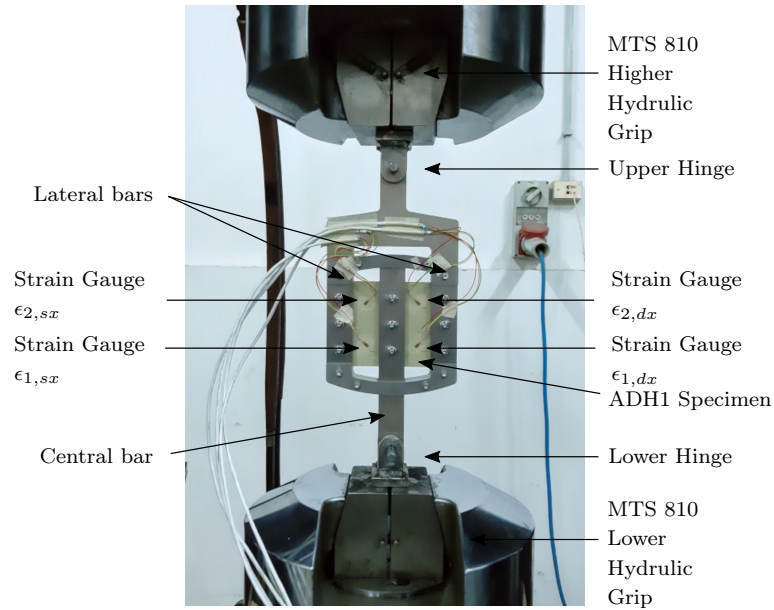


Figure 4.13: Shear test setup.

4.3 Experimental results

4.3.1 Tensile test results

The following standard equations were used to convert the test result into engineering tensile stress (σ_t), longitudinal (ϵ_y) and transversal (ϵ_x) strain:

$$\sigma_t = \frac{F}{A} \quad (4.1)$$

$$\epsilon_y = \frac{\Delta y}{y_0} \quad (4.2)$$

$$\epsilon_x = \frac{\Delta x}{x_0} \quad (4.3)$$

where F is the applied load, A is the cross-sectional area of the sample, Δy is the axial extension, Δx is the lateral extension, y_0 is the longitudinal displacement transducer gauge length equal to 50 mm and x_0 is the lateral gauge length equal to the sample width. Then the computed stress and strain values were plotted to draw stress-strain curves as shown in Figure 4.14 and Figure 4.15. The irregularities of lateral strain curves, more evident for the ADH2, are caused by the not expected random slipping of transducer blades

over the lateral surface of the sample. Research into solving this problem is already in progress. For homogeneous, isotropic, elastic material submitted to the action of normal stress the modulus of elasticity E and the Poisson's ratio are given by the equations:

$$E = \frac{\sigma}{\epsilon_y} \quad (4.4)$$

$$\nu = -\frac{\epsilon_x}{\epsilon_y} \quad (4.5)$$

The modulus of elasticity was determined, according to EN ISO 527 by applying a linear regression to the initial linear region of the stress-strain curve, in the longitudinal strain interval $0.0005 \leq \epsilon_y \leq 0.0025$. The slope of a least-squares regression line fit to this data subset was assumed as the modulus of elasticity. Figure 4.16 and Figure 4.17 detail the stress-strain curve subset and the fitted line for specimens TI-3 and TII-5. Regarding the reduction of Poisson's ratio due to the aforementioned difficulties in measuring the lateral contraction of samples and taking into account that is not recommended (EN ISO 527) to determine Poisson's ratio in the strain region used for the modulus determination, longitudinal strain - lateral strain curves were plotted for each test. Then a different longitudinal strain interval was selected corresponding to a linear portion of the specimen curve. Applying a linear regression to the selected interval of the stress-strain curves the slope was taken as the Poisson's ratio (Figure 4.18).

The overall bulk tensile properties of the selected adhesives were obtained eliminating from the test results those results relevant to both when premature failure in specimens was detected (e.g. caused by observable flaws on the surface of the broken section), and when the lateral displacement measurement system presented an evident slipping issue during the test. The bulk adhesive properties as computed by tensile tests results, reduced as indicated above, are summarized in Table 4.5.

Table 4.5: Adhesives properties obtained from tensile test.

Adhesive ID	E (MPa)	St.Dev. E (MPa)	ν (-)	St.Dev. ν (-)	σ (MPa)	St.Dev. σ (MPa)	ϵ_l (%)	St.Dev. ϵ_l (%)
ADH1	2328	143	0.33	0.01	16.3	0.63	1.09	0.096
ADH2	10680	331	0.36	0.06	26.9	0.94	0.28	0.02

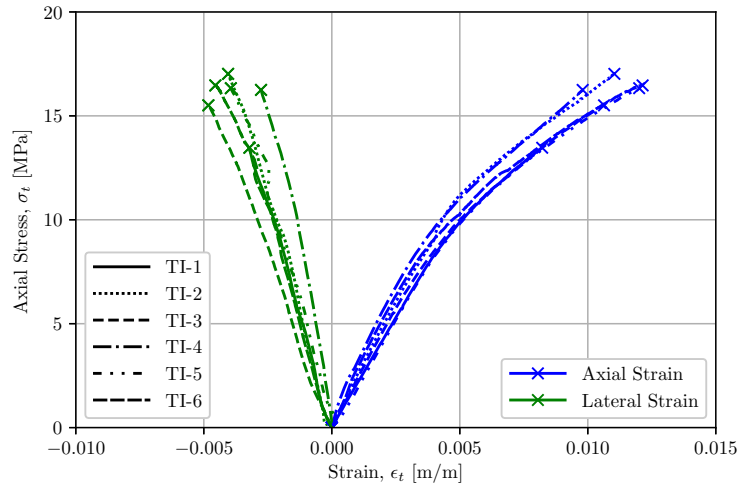


Figure 4.14: Axial Stress - Axial and Lateral Strain of ADH1 tensile tests.

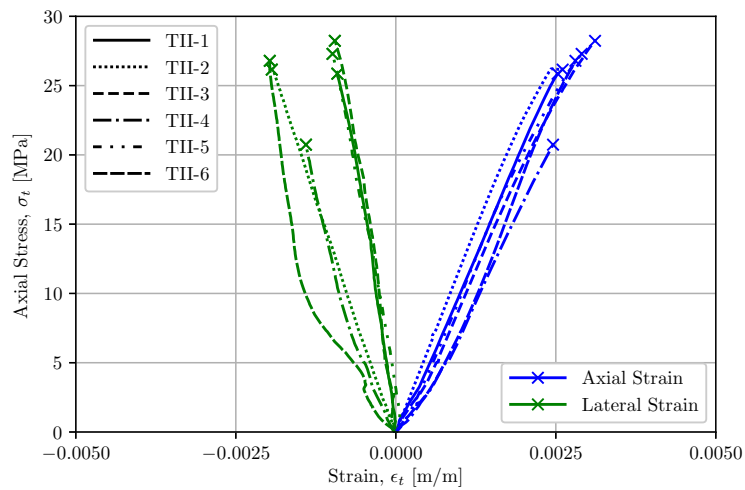


Figure 4.15: Axial Stress - Axial and lateral Strain of ADH2 tensile tests.

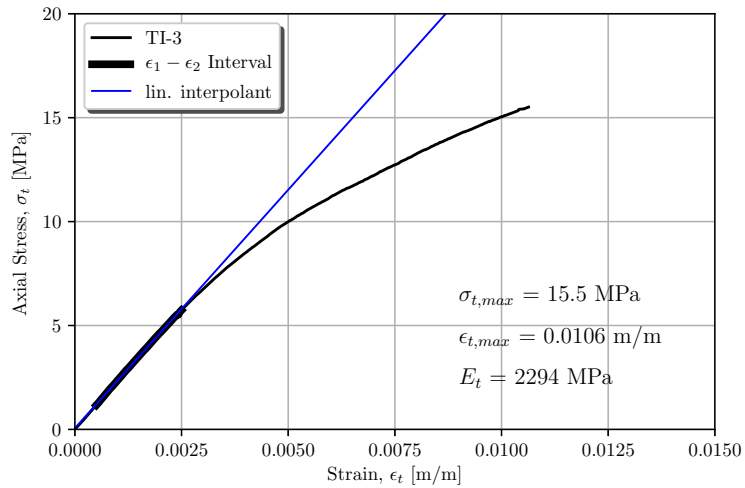


Figure 4.16: Stress-Strain diagram with main results of tensile test for TI-3 sample.

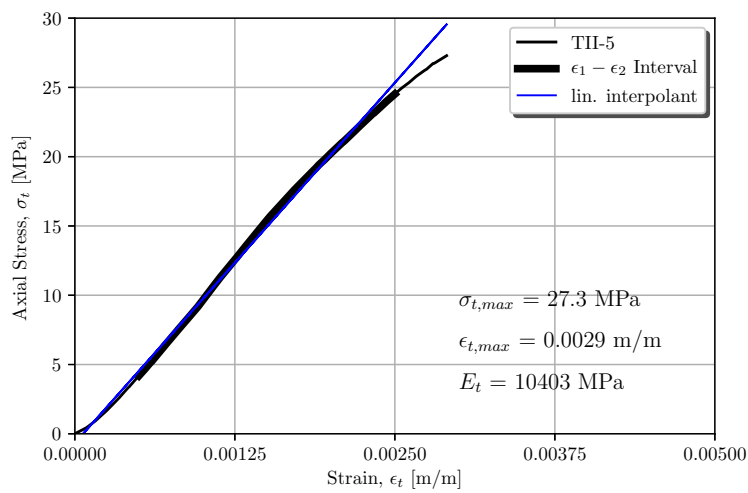


Figure 4.17: Stress-Strain diagram with main results of tensile test for TII-5 sample.

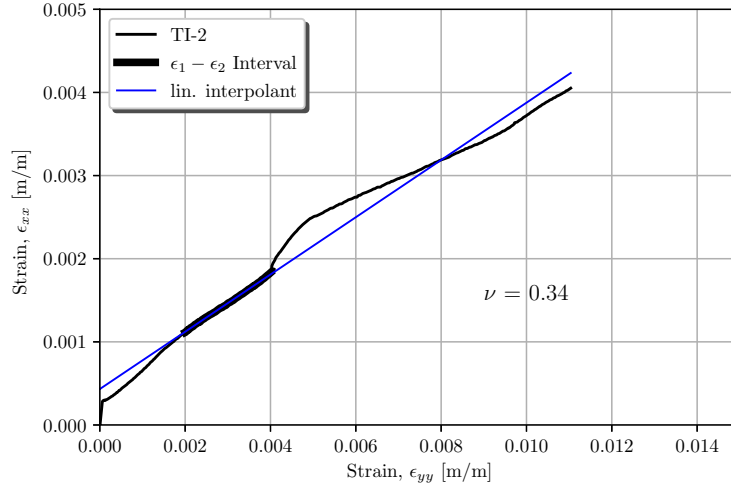


Figure 4.18: Poisson's ratio determination of sample TI-2.

4.3.2 Compression test results

In Figure 4.19 the raw data of load and longitudinal displacement acquired in the compression test of samples CI-4 and CII-3 are presented. The trends of the graphs are representative of all the other specimens for each selected adhesive. Moreover the small differences between the values of LDTV readings prove the good alignment of the compressive force with the specimen axis. Only specimens of ADH2 adhesive presented an evident collapse whereas specimens of ADH1 adhesive withstood up to 5% longitudinal deformation without any exterior damage. Therefore loading of samples of

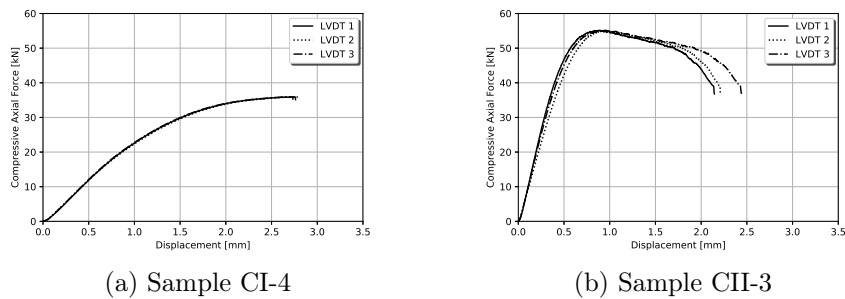


Figure 4.19: Raw data acquired from compression test.

ADH1 adhesive was interrupted about at 2.6 mm to 2.8 mm relative displacement between MTS810's platens. Axial stress were calculated by means of Equation 4.1. Longitudinal strain is computed from the equation below:

$$\epsilon_y = \frac{1}{3h} \sum_{i=1}^3 d_i, \quad (4.6)$$

where d_i , $i = 1, 2, 3$, are the displacements measured by the LVTDs and h is the specimen height. The transversal strain ϵ_x was directly provided by the strain gauge applied to the lateral surface of the specimens through the NI9237 module. The computed values of stress and longitudinal strain along with transversal strain were plotted to draw the stress-strain diagrams reported in Figure 4.20 and Figure 4.21. It is worth to point out that the maximum transversal strain depicted in the graphs is not the failure strain because of strain gauge de-bonding or saturation. Recalling Equation 4.4 and Equation 4.5, the modulus of elasticity and the Poisson's ratio were computed by applying a linear regression to the initial linear region of the longitudinal stress-strain curve and longitudinal strain-transversal strain curve, respectively. The longitudinal strain interval assumed for the determination of the modulus of elasticity was $0.0025 \leq \epsilon_y \leq 0.0075$, for the adhesive ADH1 (Figure 4.22) and $0.0025 \leq \epsilon_y \leq 0.0050$, for the adhesive ADH2 (Figure 4.23). The linear region of the longitudinal strain-transversal strain curve in which the Poisson's ratios was calculated corresponds to the longitudinal strain interval $0.0075 \leq \epsilon_y \leq 0.0125$ and $0.005 \leq \epsilon_y \leq 0.0075$ for ADH1 and ADH2, respectively. Figure 4.24 shows the longitudinal strain-transversal strain curve, the curve subset considered in computation and reports the value of Poisson's ratio determined for sample CI-3. The bulk adhesive properties obtained from compression test data are reported in Table 4.6.

Table 4.6: Adhesives properties obtained from compression test.

Adhesive ID	E (MPa)	St.Dev. E (MPa)	ν (-)	St.Dev. ν (-)	σ (MPa)	St.Dev. σ (MPa)	ϵ_l (%)	St.Dev. ϵ_l (%)
ADH1	2347	82	0.33	0.01	56.7	0.85	4.93	0.27
ADH2	8855	227	0.27	0.02	79.4	4.78	3.48	1.06

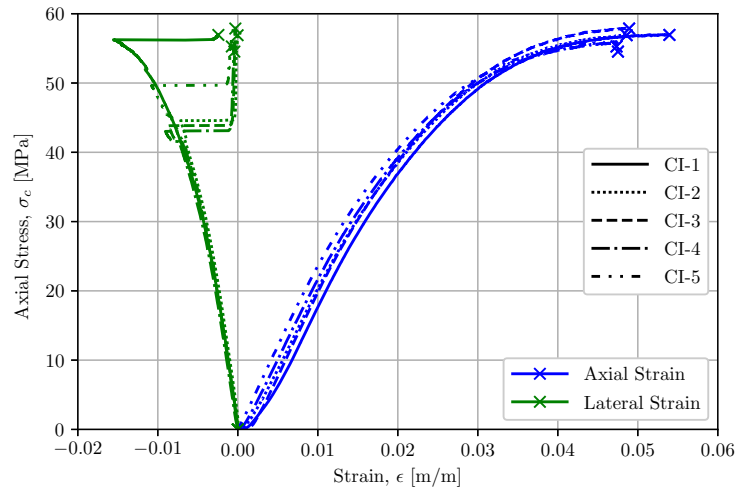


Figure 4.20: Axial Stress - Axial and Lateral Strain of ADH1 compression tests.

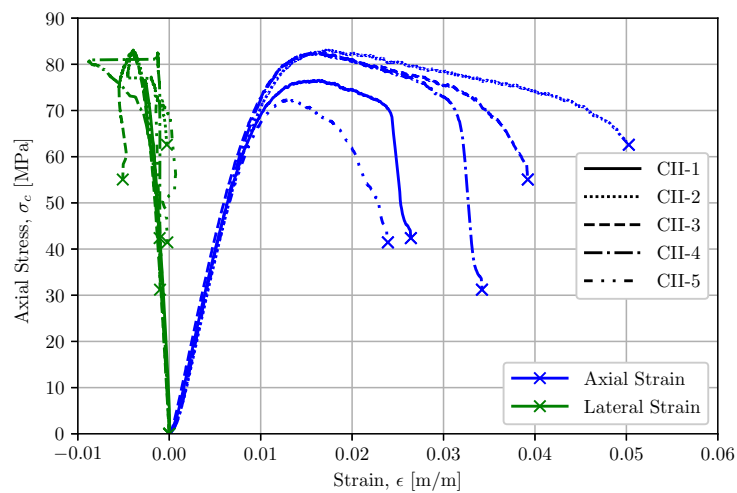


Figure 4.21: Axial Stress - Axial and Lateral Strain of ADH2 compression tests.

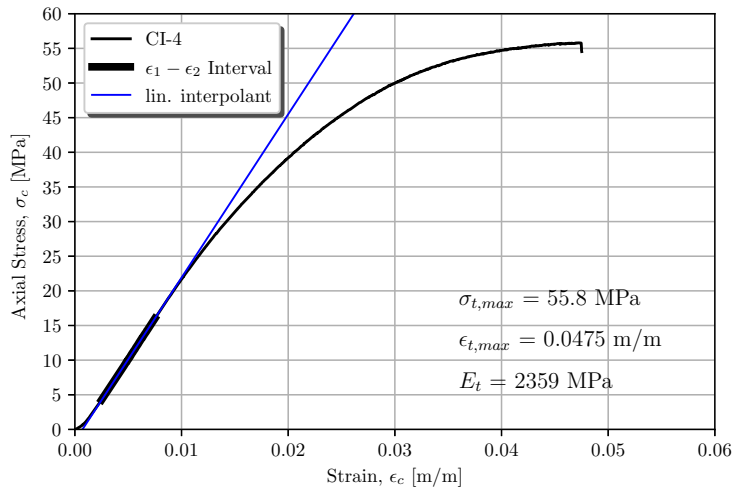


Figure 4.22: Stress-Strain diagram with main results of tensile test for sample CI-4.

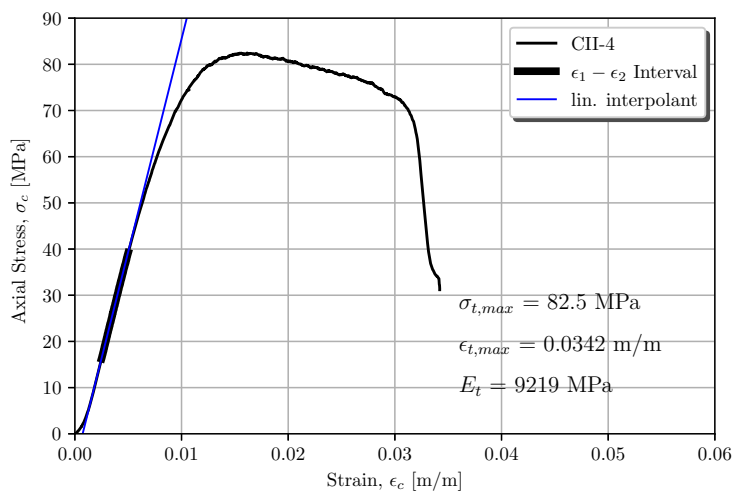


Figure 4.23: Stress-Strain diagram with main results of tensile test for sample CII-4.

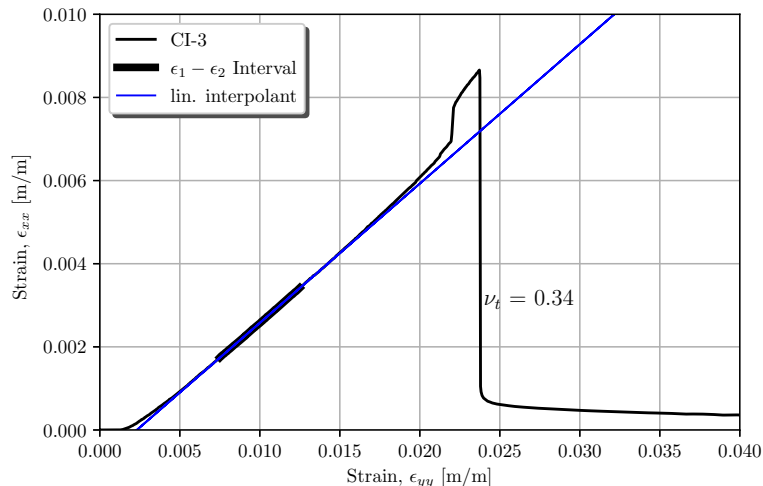


Figure 4.24: Poisson's ratio determination of sample CI-3.

4.3.3 Shear test result

The load measured by the MTS810 load cell and strains acquired with the strain gauges of the specimen SI-1 are reported in Figure 4.25. The curves load-strain are representative of all the other specimens for each selected adhesive. It should be noted that curves corresponding to symmetrical strain gauges, $\epsilon_{1,sx}-\epsilon_{1,dx}$ and $\epsilon_{2,sx}-\epsilon_{2,dx}$ (Figure 4.13), are almost superimposable. This proves that the designed fixture works properly, i.e. it applies symmetric deformation to the specimen. The shear stress was calculated as:

$$\tau = \frac{F}{2ht} \quad (4.7)$$

where F is the applied load on central bar (each portion of the sample carries half of the total force), h is the height of the specimen, t is the thickness. In the specimen subjected to an engineering shear strain γ_{12} (Figure 4.26 (a)) theoretically, except the portions near the edges and near the grips, the induced deformation state (Figure 4.26 (b)) can be represented on Mohr's circle (Figure 4.26 (c)). Points C_1 and C_2 on the circle represent the strain state for the element, having unit normals \mathbf{e}_1 and \mathbf{e}_2 , respectively. Making a counter-clockwise angle $2\alpha = \pi/2$ on Mohr's circle we obtain points F_1 and F_2 , which represent the principal in-plane strains. These strains, according to a rotation of $\alpha = \pi/4$ for F_1 and of $\alpha = 3/4\pi$ for F_2 on the surface of

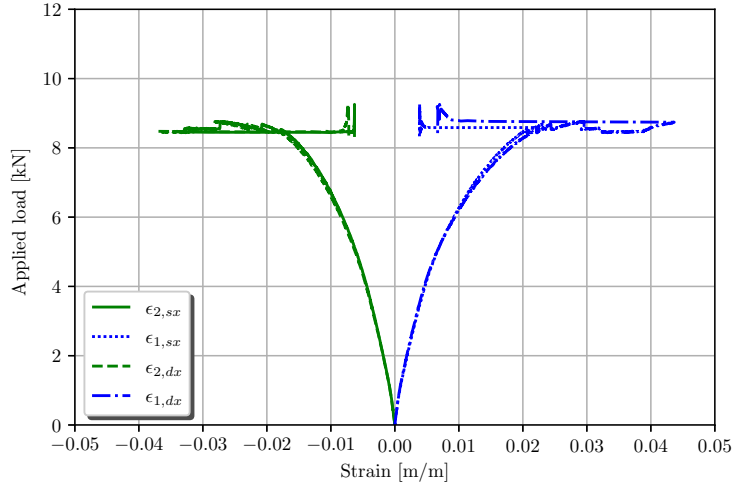


Figure 4.25: Shear test raw data, sample SI-1.

the specimen (Figure 4.26 (d)) can be measured with strain gauges mounted under an angle of 45° , ϵ_{+45} and -45° , ϵ_{-45} , with respect to the vertical axis of the specimen. Therefore the shear strain was given by the equation:

$$\gamma_{12} = |\epsilon_{+45} - \epsilon_{-45}|. \quad (4.8)$$

Having two couple of strain gauges, Figure 4.13, the average value of shear strain is calculated as follows:

$$\gamma_{12,ave} = \frac{|\epsilon_{1,sx} + \epsilon_{1,dx} - (\epsilon_{2,sx} + \epsilon_{2,dx})|}{2}. \quad (4.9)$$

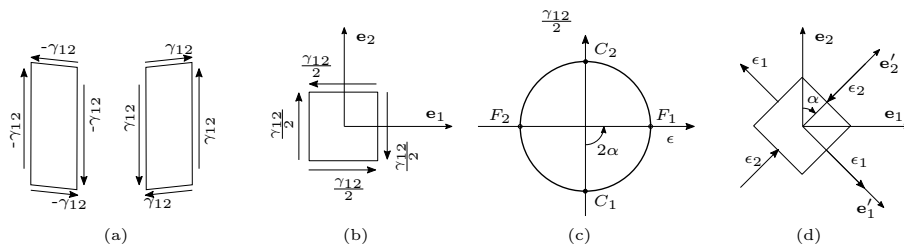


Figure 4.26: (a) Engineering strain; (b) Deformation state; (c) Mohr's circle; (d) Principal strain.

With the average shear stress, the shear modulus, G , can be determined from the shear stress and shear strain as follows:

$$G = \frac{\tau_{ave}}{\gamma_{12,ave}}. \quad (4.10)$$

The shear modulus was calculated herein applying a linear regression to the initial linear portion of the curve shear stress-shear strain. The shear strain region assumed for the computation of G was $0.0001 \leq \epsilon_y \leq 0.001$ as shown in Figure 4.27. It is worthwhile noting that the maximum shear strain depicted in the graphs is not the failure strain because of strain gauge de-bonding or saturation. The results from these calculations are reported in Table 4.7.

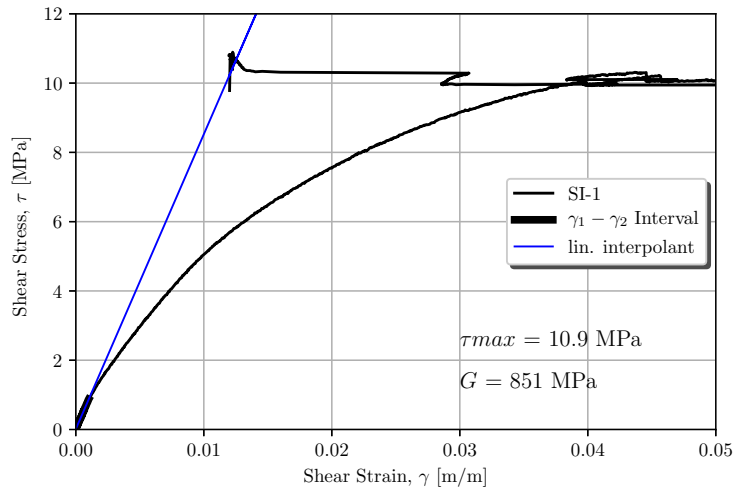


Figure 4.27: Shear Stress-Shear Strain and main results for sample SI-1.

Table 4.7: Adhesives properties obtained from shear test.

Adhesive ID	G (MPa)	St.Dev. G (MPa)	τ (MPa)	St.Dev. τ (MPa)
ADH1	832	19	11.6	2.2
ADH2	4043	36	13.7	2.6

4.3.4 Main obtained results

The determined Young's modulus and Poisson's ratio from tensile tests and compression tests for the adhesives assumed similar values, as the results reported in Table 4.5 and Table 4.6 show. The selected adhesives in the tensile test both exhibit a brittle behaviour without any definite yield point. There are no stress values at which the deformation occurs without further load increase.

In compression, the ADH1 specimens withstand up to 5% deformation without any exterior damage and show, for strain greater than this value a plateau. For this reason, the test is interrupted at this level of deformation. On the contrary, before the failure, ADH2 specimens present softening behaviour after the peak of maximum stress.

In the shear test, the adhesives behave in a more ductile manner than in the tensile test. To further our research, we plan to investigate if the tensile specimen manufacturing may cause this difference. However, regardless of specimen problems, we have compared the elastic shear modulus, directly calculated using the shear test results, with those calculated with Equation 3.21 using Young's modulus and Poisson's ratio obtained from tensile and compression tests. Table 4.8 summarizes the bulk adhesives properties.

4.4 Conclusion

The comparison between the results obtained from the test and the corresponding theoretic values is encouraging since they are very similar, thus giving confidence to the assumption that proposed test set-ups provide uniform uniaxial and pure shear stress states. Since both the adhesives do not show a definite yield point the constitutive law advisable to use, for finite element modelling, is the linear one.

Table 4.8: Elastic bulk adhesives properties.

Adhesive ID	Shear test		Tensile test			Compression test			
	G (MPa)	E (MPa)	ν (-)	G (MPa)	ΔG (%)	E (MPa)	ν (-)	G (MPa)	ΔG (%)
ADH1	832	2328	0.33	875	-5.19	2347	0.33	882	-6.05
ADH2	4043	10680	0.36	3926	2.88	8855	0.27	3486	13.77

Chapter 5

Testing of Double-shear lap-splice joint

5.1 Introduction

The double lap shear joint consists of two rectangular steel plates adhesively bonded using two rectangular composite panels. Figure 5.1 shows the dimensions for the steel plates, the composite plates, the bondline thickness and the gap. At this stage of testing only the dimensions of the composite plates assumes two different lengths, 110 mm and 210 mm. Hence, maintaining a constant gap, each portion of joined steel plates' overlap lengths results equal to 50 mm e 100 mm, respectively.

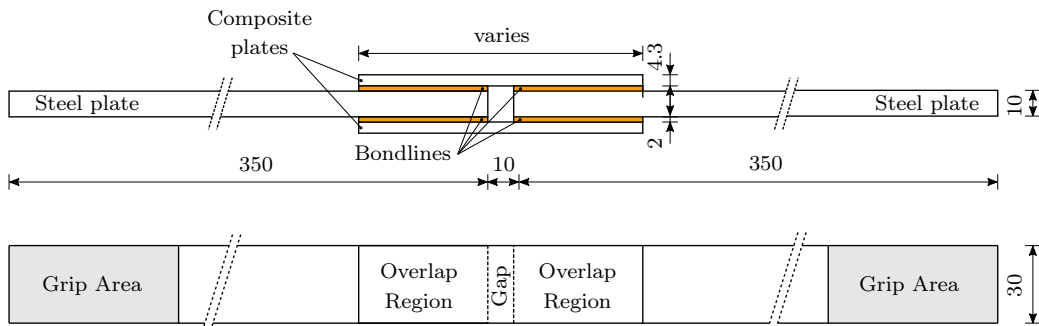


Figure 5.1: Dimensions of Double Lap Shear Joint.

5.2 Materials and Methods

5.2.1 Steel adherends

The metallic parts of the joint are laser-cut plates made of standard grade S355J2 steel. According to the code ISO 6892-1, we performed the material characterization tests on three samples. Table 5.1 shows the test results, where b and h are the sample transversal section height and width, R_{eH} is the upper yield strength, R_m is the tensile strength, A is the percentage elongation after fracture and E is the modulus of elasticity. Table 5.2 reports the average values of the measured properties.

Table 5.1: Results of tensile test, according to ISO 6892-1:2009.

Sample	h (mm)	b (mm)	R_{eH} (MPa)	R_m (MPa)	A (%)	E (GPa)
01	10.02	24.95	428.4	575.0	27.0	202.86
02	10.01	24.95	426.0	575.9	26.5	206.51
03	10.02	24.95	429.4	578.2	27.5	195.50

Table 5.2: Average properties of S355J2 steel.

Property	Unit	Value
Yield strength	MPa	428.0
Tensile strength	MPa	576.4
Elongation after fracture	%	27.0
Modulus of elasticity	GPa	201.6

We degreased all the steel parts using first an alkaline solution and then acetone. To keep the overlap regions chemically active, we sandblasted with 80-mesh red-brown corundum, wipe cleaned and accurately re-degreased with acetone these surfaces, just before the joints assembly.

5.2.2 Composite adherends

The composite adherends consist of ATLAC 580 ACT resin reinforced with four layers of E-Glass multiaxial fabric from SÖNMEZ Textiles Ad-

vanced. ATLAC 580 ACT is a pre-accelerated thixotropic, high-grade bisphenol A vinyl ester urethane resin. A single E-Glass fabric layer contains five types of fibres, CSM/45/90/-45/0, stitched with textured polyester yarn. The specimens has been provided by courtesy of Carbon Compositi Srl¹. At the company laboratory, the operator used methyl ethyl ketone peroxide (MEKP) as initiator mixed 1.5 % by volume with the resin. The multiaxial stitch-bonded reinforcement fabric was impregnated with resin and rolled, stacking four fabric sheets one above the other, by hand lay-up technique. Just after the lamination, the whole laminate was compressed at a constant pressure of 0.03 MPa using a pneumatic press, until the resin has fully cured. A single laminated plate of 0.80 m x 0.80 m x 0.0043 m was obtained. The laminate has the following stacking sequence:

$$[(CSM^{225}/ + 45^{234}/90^{165}/ - 45^{234}/0^{165})_2]_s.$$

With the adopted procedure, we were confident in obtaining a fibre mass fraction value, M_f , as close as possible to typical values of filament wound laminates employed in the tank industry that are 60 % to 75 %). After the curing phase, the specimens were cut out from the laminated panel. Figure 5.2 details the dimensions of samples. Each of the named group of specimens in Figure 5.2 corresponds to a specific test, more specifically:

- A.x, tensile test and determination of the laminate elastic modulus in x direction, E_x ;
- A.y, tensile test and determination of the laminate elastic modulus in y direction, E_y ;
- B, loss on ignition test;
- C, tensile test on double-shear lap-splice joint (adhesive length 50 mm);
- D, tensile test on double-shear lap-splice joint (adhesive length 100 mm);
- E, inter-laminar shear strength of laminate.

Test on groups A.x, A.y, B and E are needed to characterize the joint's composite components mechanically. According to the code EN 13121:2016 (par. D.5-D.6), we performed the tensile test on A.x and A.y samples. Figure 5.3.a

¹Carbon Compositi S.r.l., Via Zanon n.14/16, 33031 Basiliano (UD), Italy

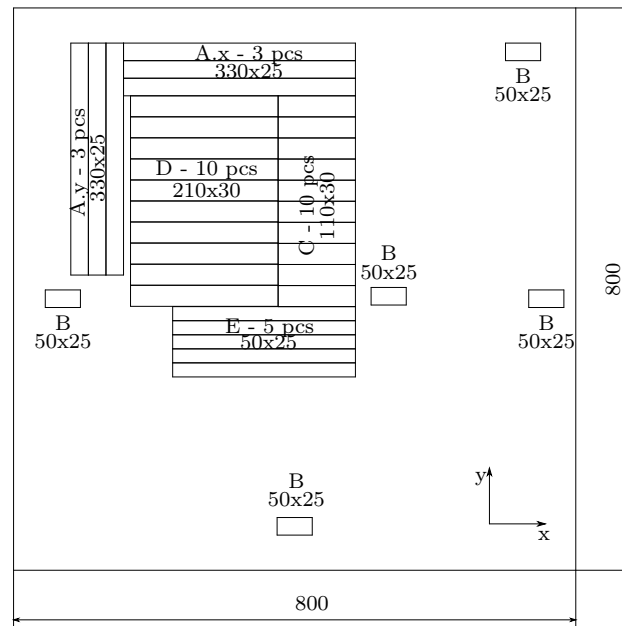
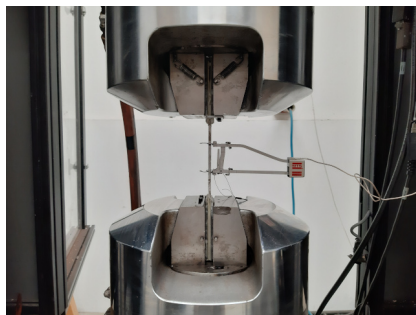


Figure 5.2: Test specimen panel cut layout.

shows the tensile test's experimental setup with the extensometer mounted on the sample Ax.1. The extensometer is needed to measure the longitudinal strain and must be unmounted before the sample break. Figure 5.3.b shows the sample Ax.2 at the end of the test.



(a) Sample Ax.1 during tensile test



(b) Broken Ax.2 sample

Figure 5.3: Tensile tests on composite parts.

Table 5.3 reports the test results, where h and b are the sample transversal section height and width, σ_t is the ultimate tensile strength, and E is the tensile modulus.

Table 5.3: Results of tensile test, according to EN 13121:2016.

Sample	h (mm)	b (mm)	σ_t (MPa)	E (GPa)
Ax.1	3.90	25.29	241.1	15.87
Ax.2	3.95	25.13	245.7	16.09
Ax.3	3.99	23.76	262.6	15.58
Ay.1	3.95	25.34	276.9	16.07
Ay.2	3.74	25.40	255.1	17.35
Ay.3	4.32	25.86	225.6	14.83

To assess the average textile-glass content of the specimen panel, the loss on ignition test was performed on the group of samples B. Figure 5.4 shows samples B cut-out from the specimen panel, before and after calcination. Table 5.4 exposes the test results, b , l and h are the specimen's width, length and height, m_1 is the initial mass of the dried specimen, ρ_c is the composite density, m_2 is the final mass of the residue after calcination and M_f is the fibre mass fraction. The fibre mass fraction is expressed as a percentage of the composite's initial mass using the equation $M_f = m_2/m_1 \cdot 100$.



(a) Laminate samples.



(b) After calcination at 600 °C

Figure 5.4: Loss on ignition test of composite adherend samples (group B).

Table 5.5 reports the average values for the measured properties of composite plates used in the joint making. The obtained fibre mass fraction for the specimens, $M_f = 0.575$, is slightly lesser than the minimum value, $M_{f,min} = 0.600$ of the typical range filament wound laminates. However, this can be considered acceptable for the research. Given the mechanical prop-

Table 5.4: Results of loss on ignition test, according to EN 13121:2016.

Sample	b (mm)	l (mm)	h (mm)	m_1 ($\text{kg}\cdot 10^{-3}$)	ρ_c (kg m^{-3})	m_2 ($\text{kg}\cdot 10^{-3}$)	M_f
B.1	25.32	50.15	4.11	8.565	1642	5.045	0.589
B.2	25.39	50.21	4.19	8.745	1636	5.160	0.590
B.3	25.29	50.27	4.53	9.010	1563	5.025	0.558
B.4	24.92	50.23	4.40	8.970	1624	5.140	0.573
B.5	25.32	50.29	4.26	8.830	1626	4.975	0.563

erties of the resin and the glass fibre, the stacking sequence, and the fibre mass fraction, the value of the elastic modulus, calculated with the module *cmplam* results in $E_x = E_y = 13\,982$ MPa. This value is still similar to the experimental ones. It is worth noting that the fibre mass fraction refers to the laminate as a whole. Therefore it is the averaged value of fibre mass fraction of the singular lamina. The lamina's fibre mass fraction depends on the fibre degree of impregnation strictly correlated to the single-layer fibre form. For example, a laminate hand lay-up made of CSM layers can reach a maximum glass content by mass of about 35 %, whereas a WR laminate can lead to a glass content by mass of 55 %. In the theoretical calculation of elastic modulus, M_f 's average value was assigned to both unidirectional and CSM layers, explaining the difference with the experiment values.

Table 5.5: Average properties of the laminated adherends.

Property	Unit	Value
ρ_c	kg m^{-3}	1619
M_f	-	0.575
$\sigma_{t,x}$	MPa	250
E_x	GPa	15.85
$\sigma_{t,y}$	MPa	253
E_y	GPa	16.09

Items C and D of the specimens (Figure 5.2) refer to composite adhered parts of the steel-GFRP joint samples. Before joining the composite parts to the steel, we abraded the composite plate's bond-side with medium sand-

paper, then the surfaces were wipe cleaned and finally wiped with acetone.

5.2.3 Adhesives and bonding procedure

We planned to use the two selected adhesives ADH1 and ADH2 characterized in Chapter 4. The steel plates were aligned longitudinally using a custom-designed template. We applied the adhesive to both the steel and composite surfaces. Then the composite plates were joined to the steel plates. PLA 3D printed spacers were positioned between the adherends to ensure a consistent bondline thickness. The template held the constructed joints in place for the minimum required setting time of the adhesive.

5.3 Test procedure

We deferred to future work the execution of the tests because the preparation of the samples involved a great effort and we are currently investigating which measures to carry out to get as much data as possible from each single test. We will use the multipurpose servo-hydraulic testing system MTS 810 with a constant cross-head movement rate for a tensile test. The rate will be adjusted to achieve a shear strain deformation rate in the bondline of joint as close as possible to the shear strain deformation rate used in bulk adhesive testing.

Chapter 6

Modelling of adhesively bonded joints

6.1 Introduction

The end goal of finite element analysis with adhesively bonded joints is to employ the resulting characterization of simple experimental tests on the materials and to make predictions of the adhesive performance in complex joints. In this research stage, we aimed at determining a modelling method that gives reasonably accurate predictions of the stiffness and stresses of a Double Shear Lap Splice joint. This chapter briefly presents our modelling strategy adopted to define a fully parametric model of a DSLS joint. We illustrate the developed model's application with a static load simulation of the joint prepared for testing in the future research programme. Modelling input requires the bulk properties of the metal, adhesive and composite of the test specimens used. We provided the bulk properties of metal and adhesive from the experimental test we performed, whereas we calculated the properties of GFRP laminates using our custom developed module `cmplamy`. Finally, we compared the simulation results with the analytical solution proposed by Tsai, Oplinger and Morton in [50].

6.2 Modelling strategy

Our modelling approach's critical aspects were to obtain an entirely parametric geometry joint definition and retain the laminated nature of the com-

posite adherends by modelling each lamina separately. The former feature permits the rapid development of different joint geometry for parametric studies without model manipulation but merely changing the desired parameter. The latter allows the calculation of layer stresses and the application of specific failure criteria to the composite materials for future investigations. The laminae in laminated GFRP parts of the joint (Figure 6.1) may have different orientations. Therefore the joint has not any symmetry and requires the whole geometry to be modelled.

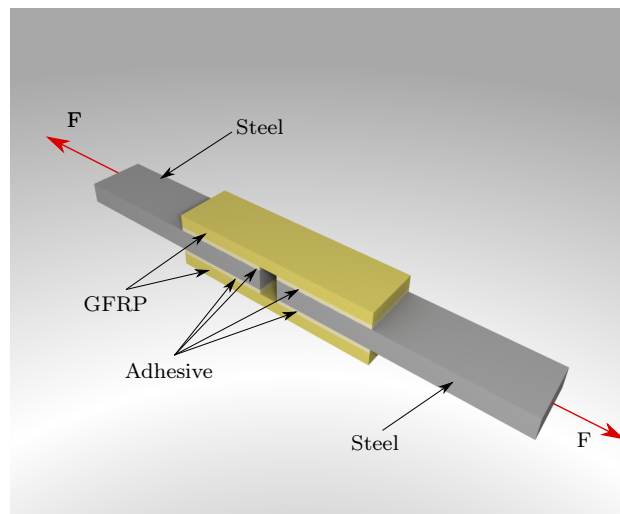


Figure 6.1: Double-shear lap-splice joint.

The open-source general finite element package, `code_aster` [68] and the open-source 3-D finite element grid generator `Gmsh` [69], were used to develop a three-dimensional finite element, linear model of the parametric double-shear lap-splice joint. Figure 6.2 shows the free parameters of the geometry, where:

- b is the joint width;
- l_a is the overlap (bondline) length;
- t_a is the adhesive thickness;
- l_s is the steel plate length;
- t_s is the steel plate thickness;

- d is the gap length;
- n_l is the number of unidirectional composite layers.

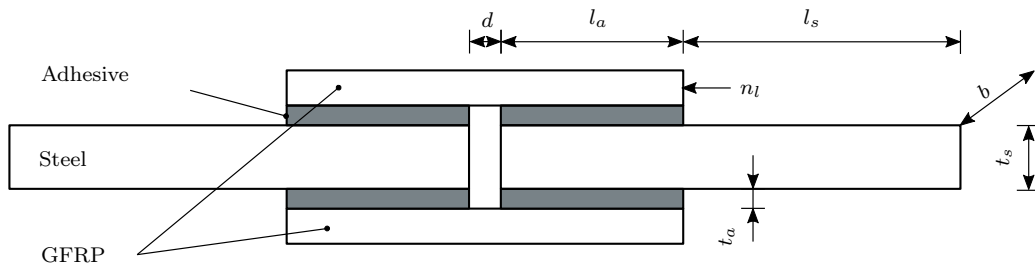


Figure 6.2: Model dimensions described by free parameters.

Each unidirectional composite layer requires the elastic constants properties in material coordinates and the layer orientation related to the laminate coordinates system.

The obtained parametric model has a structured mesh and permits the selection of the hexahedron (MECA_HEX8) finite elements' characteristic length for its various portions. We wrote more than five hundred lines of python code, gmsh script language code and code_aster commands to develop the parametric model.

6.3 Finite element analysis of the Double-Shear Lap-Splice Joint

Considering a bondline length of 50 mm and an adhesive thickness of 2 mm, we modelled the geometry of the joint shown in Figure 5.1. In the steel portions away from the adhesively bonded part, the stress and strain values are relatively uniform. Therefore, in the model, we shortened both the steel ends to 200 mm. Figure 6.3 illustrates the 3D model of the joint to be meshed. The visualization highlights five different materials involved in the model. Steel parts are blue coloured; light blue represents the adhesive layer; the layers of composite, MAT ply (225 g m^{-2} , 0.291 mm thick), unidirectional ply of 234 g m^{-2} , 0.232 mm thick and unidirectional ply of 165 g m^{-2} , 0.163 mm thick, are represented in light green, orange and dark brown, respectively.

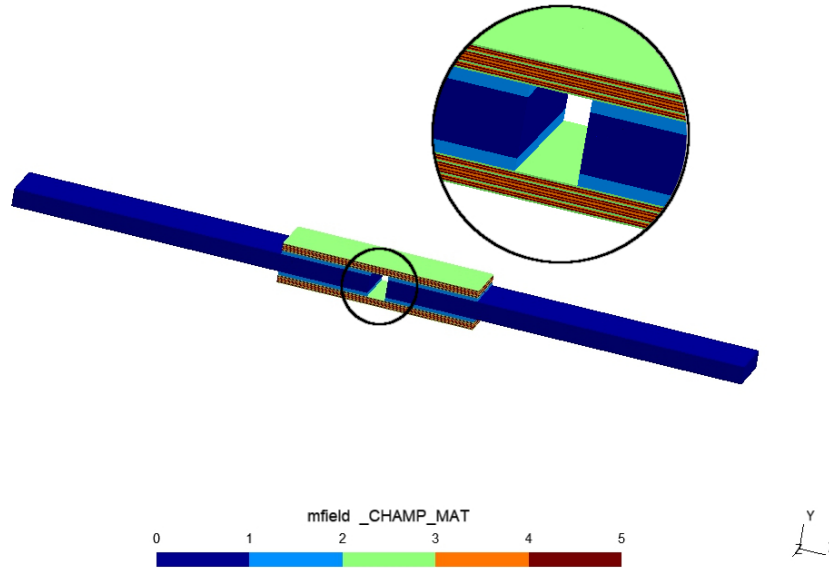


Figure 6.3: Material fields as assigned in code_aster, the detail shows the laminae of composite.

Since the experimental data on the GFRP laminates, together with those on the Double-Shear Lap-Splice joints, would be available in the next research stage, assuming the mass volume fraction $M_f = 60\%$ for unidirectional lamina and $M_f = 50\%$ for the MAT lamina, we used our custom module `cmplamy` to compute the elastic properties of the laminated parts of the joint. Table 6.1 reports the computed values of the elastic constants and the thickness for each lamina type.

We owned the average properties for the steel on the S355J2 plates employed for the joints manufacture, experimentally determined and reported in Table 5.2. In addition for the adhesive ADH1, we adopted the experimental results obtained with the bulk adhesive tests summarized in Table 4.8.

After setting the free parameters' values, we assigned to the material groups, their properties and produced the meshed geometry. Figure 6.4 illustrates the finite element model.

We imposed null displacement to the nodes belonging to the transversal surface on the left-hand side of the model. We decided to perform the anal-

Table 6.1: Material parameters for modelling composite adherends, as introduced in code_aster.

Lamina property	Lamina type		
	0^{165} & 90^{165}	45^{234} & -45^{234}	CSM^{225}
E_L (GPa)	30.230	30.230	13.457
E_T (GPa)	8.834	8.834	13.457
E_N (GPa)	8.834	8.834	13.457
G_{LT} (GPa)	2.672	2.672	4.784
G_{TN} (GPa)	3.142	3.142	4.784
G_{LN} (GPa)	2.672	2.672	4.784
ν_{LT}	0.318	0.318	0.407
ν_{TN}	0.406	0.406	0.407
ν_{LN}	0.318	0.318	0.407
Thickness (mm)	0.163	0.232	0.291

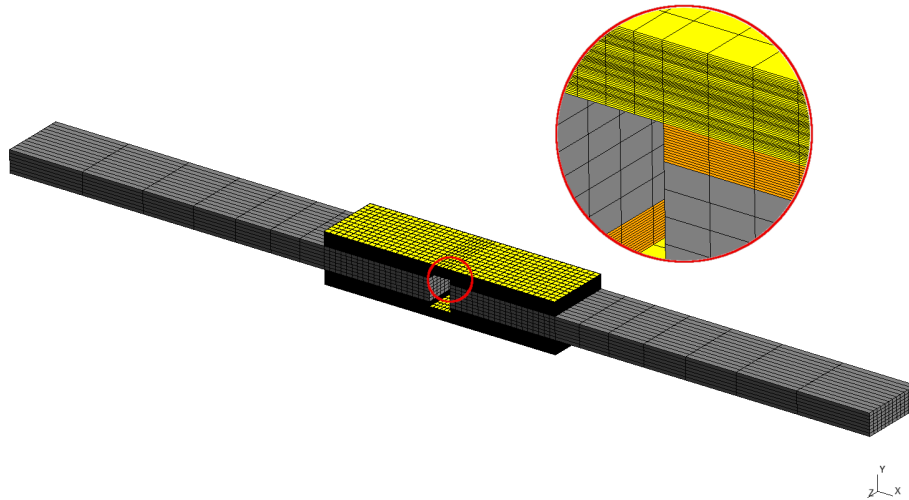


Figure 6.4: Geometry meshed with Gmsh. The detail shows the GFRP laminae and adhesive local refinements.

ysis applying a tensile load that produces an average value of shear stress in the joint, equal to half of the measured strength of the adhesive ADH1. The load results in $T = 2 \cdot \tau_{max}/2 \cdot b \cdot l_a = 2 \cdot 11.6/2 \cdot 30 \cdot 50 = 17.4 \text{ kN}$. This load was distributed over the steel surface opposite to the restrained one.

Figure 6.5 shows the displacement magnitude on the amplified deformed

geometry. Figure 6.6 highlights the shear deformation of the joint's adhesive upper right bondline.

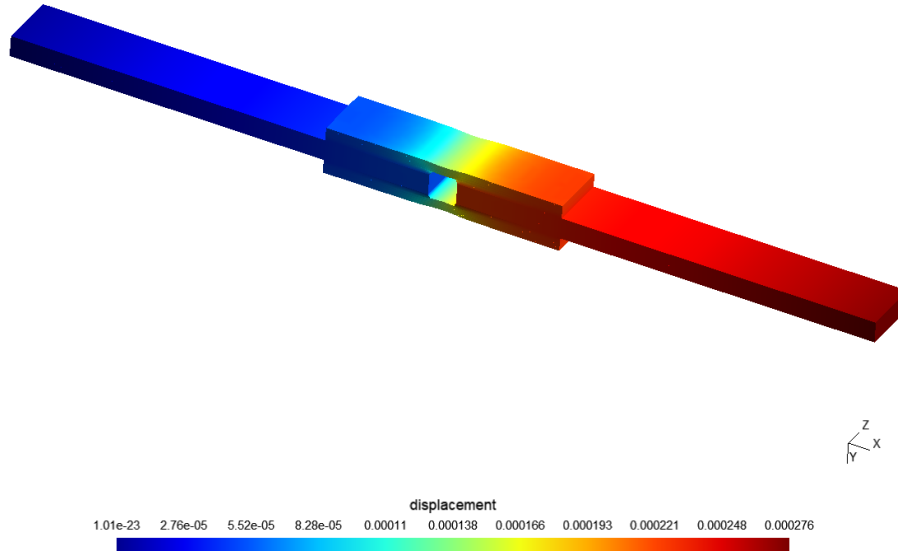


Figure 6.5: Colour map of the displacements magnitude.

Concerning the shear stresses distribution, we compared the achieved numerical values of the component of the tensor stress τ_{xy} with the results obtained implementing the Tsai, Oplinger and Morton analytical model (TOM) proposed in [50]. This analytical model considers the adherend shear deformation assuming a linear shear stress distribution through the adherend thickness. We extracted the stresses τ_{xy} from the finite element model by defining a longitudinal control line lying on the adhesive layer top surface. This surface is in contact with the GFRP plate of the joint. In the FE model,

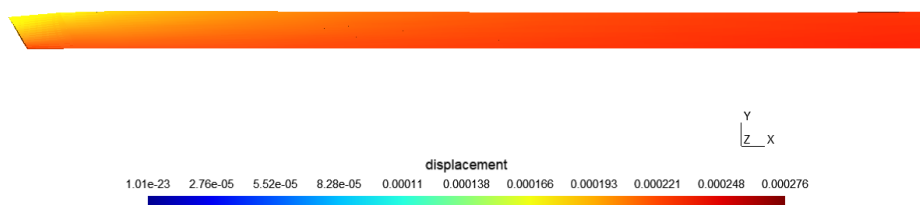


Figure 6.6: Detail of the shear deformation of the adhesive.

the adhesive layer lies in the interval $0.005 \leq x \leq 0.055$, whereas the analytical model refers to a monodimensional coordinate system with the origin centred on the adhesive length. Therefore we mapped the model interval to the dimensionless interval $-1 \leq x \leq 1$.

Figure 6.7 shows that the numerical model results are in good agreement with the analytical ones. Therefore the finite element model can be considered validated regards the comparison with theoretical models. Further validation will be performed in the future using the results of planned experimental tests.

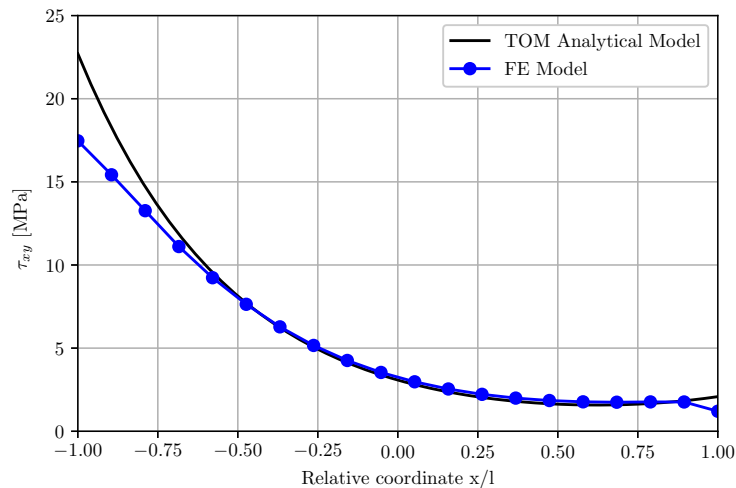


Figure 6.7: Comparison between the finite element model and the Tsai, Oplinger and Morton model.

As mentioned before, the composite plies have different stiffnesses due to the different fibre orientations and mass fraction value. Therefore, the normal stress in the lamina plane is highest for the 0° layers (fibre oriented to the model x-direction) and lowest for the 90° layers (fibres oriented in y-direction). Focusing on the normal stresses, σ_{xx} , in the GFRP portion of the joint, it is worth noting (Figure 6.8) that the model clearly exhibits its laminated nature. The red coloured layers correspond to the 0° fibre orientation.

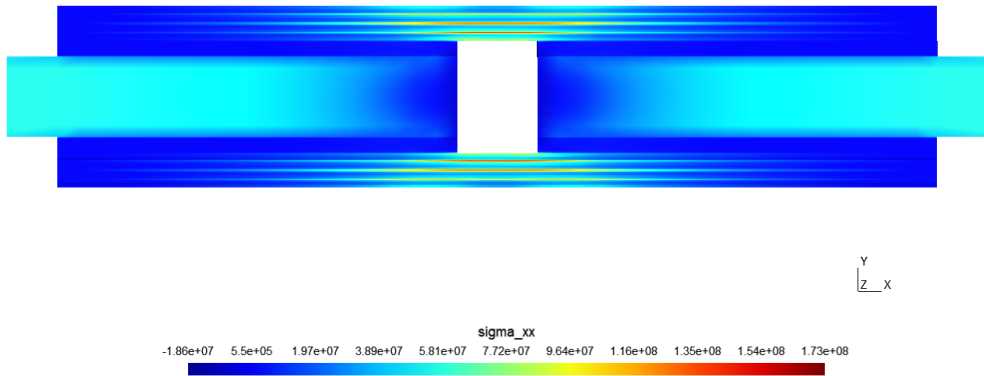


Figure 6.8: Lateral view of the color map of σ_{xx} .

6.4 Conclusion

Our modelling strategy demonstrated that it is possible to model adhesively bonded composite joints using a fully 3D model which retains the laminated nature of the composite adherends. This approach offers the possibility of accurately modelling real joints. In future studies, we plan to extend and validate our promising results to different joints geometries. Furthermore, these studies will address the choice and the application of suitable failure criteria involving both the adhesives and the composites parts of the joint to predict the whole joint performance.

Chapter 7

Design overview of a selected case study

7.1 Introduction

A tank needs to be anchored at its foundation base to withstand horizontal actions induced by earthquakes. Large uplifts or horizontal displacements out of the tank mounting position are responsible for pipeline and flanges ruptures. Therefore, an appropriate anchorage prevents tank sliding, uplifting and overturning. Moreover, proper anchorage design represents the crucial problem for satisfying safety and economic requirements of liquid storage structures. This section gives an overview of a case study research on a slender GFRP tank's anchorage. The case study first presents the selected tank structure's geometric and mechanical properties. It then illustrates the seismic induced load calculation method, based on the response spectrum, and proposes an installation technique for the anchorage apparatus. In particular, the installation technique concerns the joint between the hold-down apparatus and the tank wall. Finally, the section ends with a Finite Element Analysis of the proposed joint.

7.2 Case study description

From three Italian manufacturers, we collected the geometric and mechanical characteristics of thirty fibreglass flat bottom tanks. For each tank, Table 7.1, reports the nominal diameter D , the overall height H_T , the thick-

ness t and Young's modulus E of the wall, the liquid level H , the slenderness ratio H/R , the nominal volume V , the nature of the content and its density and, finally, the location (site) of installation. Figure 7.1 shows a histogram

Table 7.1: Tanks collected for the case study selection.

N	D (m)	H_T (m)	t (mm)	H (m)	H/R	Volume (m ³)	Content	Density (kg m ⁻³)	Location
1	3.0	5.6	4.0	4.5	3.0	31.8	HCl 33%	1100	Italy (RO)
2	2.5	5.3	7.0	4.0	3.2	19.6	H ₂ SO ₄ 70%	1600	Italy (MO)
3	2.5	5.7	7.0	4.5	3.6	22.1	H ₂ SO ₄ 70%	1400	Italy (MO)
4	3.0	6.6	4.0	5.6	3.7	39.4	FF water	1000	Italy (PO)
5	4.0	8.5	10.0	7.5	3.8	94.2	DM water	1000	Italy (MO)
6	3.0	6.6	7.0	6.0	4.0	42.4	Kymene 920	1060	Italy (MI)
7	3.0	6.6	7.0	6.0	4.0	42.4	Kymene 920 plus	1200	Italy (MI)
8	4.0	9.0	8.0	8.0	4.0	100.5	Waste water	1026	Italy (CB)
9	2.4	5.5	5.0	4.8	4.1	21.2	NaClO	1100	-
10	4.0	9.2	16.0	8.4	4.2	105.4	NaClO 20%	1220	Italy (UD)
11	4.0	10.0	19.0	9.1	4.5	114.2	DM water	1000	Italy (UD)
12	4.0	9.4	12.0	9.4	4.7	117.4	HCl 33%	1160	Italy (UD)
13	2.4	6.4	3.0	5.6	4.8	24.4	Osmotized water	1000	Italy (VR)
14	2.5	7.1	7.0	6.0	4.8	29.4	FeCl ₃ 38%	1400	Kuwait
15	3.5	8.8	16.0	8.6	4.9	82.7	NaOH 30%	1336	Italy (UD)
16	4.0	7.5	10.0	9.8	4.9	123.6	NaOH 20%	1260	Panama
17	3.0	7.9	8.0	7.4	4.9	52.3	NaOH 30%	1500	-
18	3.0	8.0	12.0	7.5	5.0	53.0	NaOH 20%	1100	Italy (VI)
19	4.0	12.8	10.0	10.0	5.0	125.6	NaOH 20%	1200	Italy (SA)
20	4.0	10.3	7.0	10.0	5.0	125.6	Liquid fertilizers	1200	Italy (RO)
21	2.0	5.7	3.0	5.2	5.2	16.3	NaClO sol.	1030	UAE
22	2.5	7.1	6.0	6.5	5.2	31.9	NH ₄ OH 25%	1200	CZE
23	3.0	8.8	18.0	8.0	5.3	56.6	NaAlO ₂	1300	Italy (RA)
24	1.4	8.4	7.0	3.9	5.6	6.0	Water	1000	USA
25	2.0	6.3	3.0	5.7	5.7	18.0	Osmotized water	1000	Italy (VR)
26	2.5	8.1	7.0	7.3	5.9	35.9	NaOH 20%	1100	Italy (FR)
27	3.0	10.2	9.0	9.3	6.2	65.8	NaClO ₂ sol.	1260	QATAR
28	2.5	8.0	9.0	7.8	6.2	38.3	NaOH 20%	1100	Italy (VI)
29	2.2	8.4	13.0	7.5	6.8	28.5	Chemicals	1800	Italy (BO)
30	2.5	10.3	12.0	9.5	7.6	46.6	NaOH 20%	1200	Spain

of the number of tanks for each slenderness interval. In the most populated

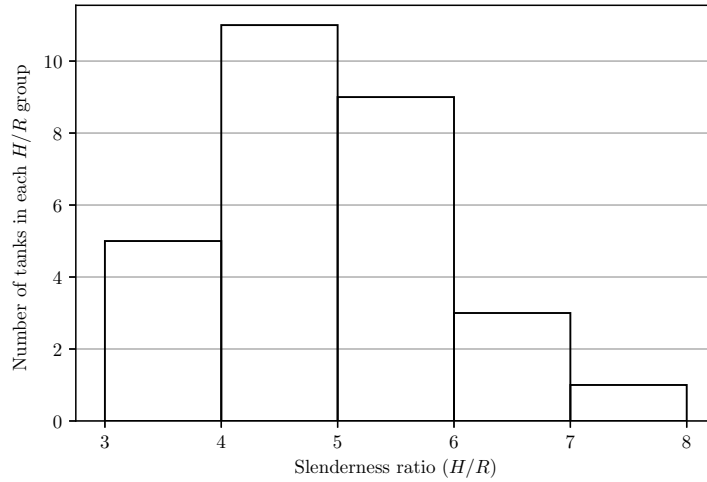


Figure 7.1: Number of tanks for each slenderness interval.

slenderness interval, $4 \leq H/R < 5$, we select the tank number 11, designed for a Class III chemical plant (as per NTC 2018 sect. 2.4.2) and having significant volume.

Overall height and diameter of the tank are 10.0 m and 4.0 m, respectively. Sixteen anchors bolts hold the GFRP tank to a reinforced concrete hexagonal foundational pedestal. The filling liquid is demineralized water with a density of 1000 kg m^{-3} . The maximum liquid freeboard level, corresponding to the height of the overflow protection, is 9.1 m. The maximum liquid level and the radius of the tank give the slenderness ratio, $H/R = 4.55$.

The top head, the stepped cylindrical wall, and the tank's flat bottom are made of a Synolite 0266-N-4 resin and E-glass fibre laminated composite. The laminates composition of each tank portion are:

- $[CSM^{450}]_{10}/WR^{500}/CSM^{450}]_{10}$ - flat bottom;
- $[(CSM^{300})_3/(67^{1140}/ - 67^{1140}/90^{1140})_8/90^{1140}]$ - wall segment 1, from 0.0 m to 2.4 m;
- $[(CSM^{300})_3/(67^{1140}/ - 67^{1140}/90^{1140})_6/(90^{1140})_2]$ - wall segment 2, from 2.4 m to 5.9 m;
- $[(CSM^{300})_3/(67^{1140}/ - 67^{1140}/90^{1140})_5]$ - wall segment 3, from 5.9 m to 9.1 m;

- $[CSM^{450}]_{20}$ - top head.

Superscript indicates the fibre's specific mass in the layer, in g m^{-2} . Table 7.2 summarize the geometric and mechanical properties of the tank's components, calculated using our custom module `cmplamy`. From now on the subscripts, x and ϕ refer to the axial and circumferential direction for the wall tank laminate.

Table 7.2: Properties of the laminates composing the tank.

Item	E_x (GPa)	E_ϕ (GPa)	$G_{x\phi}$ (GPa)	$\nu_{x\phi}$ (-)	t (mm)	δ_c (kg m^{-3})
Flat bottom	10.81	10.81	3.75	0.40	18.5	1441
Wall seg. 1	12.48	30.05	6.25	0.20	23.4	1845
Wall seg. 2	12.48	29.74	6.06	0.19	19.1	1838
Wall seg. 3	12.36	28.42	6.21	0.21	14.8	1825
Top head	10.53	10.53	3.78	0.39	17.9	1434

According to the Italian code NTC2018, we refer to the acceleration response spectrum method, for the seismic input definition. NTC2018 classifies the national territory with a micro zonation. Given the reference period for the seismic action, under a specific site horizontal rigid soil conditions, the code provides the spectral parameters, a_g , F_0 and T_c^* . Adopting in the case study the following design conditions:

- Nominal expected life of structure, $V_N = 50$ years;
- Importance class III;
- Importance factor $C_u = 1.5$;
- Reference period for seismic action $V_r = 75$ years;

the seismic hazard parameters results: $a_g/g = 0.132$, $F_0 = 2.533$ and $T_c^* = 0.368$ sec.

Identified the soil type C, the topographic class T1, the stratigraphic amplification factor $S_S = 1.5$ and known the seismic hazard parameters, we determine the values of the control periods of the elastic response spectrum,

- $T_B = 0.179$ s (eq. 3.2.5 NTC2018);

- $T_C = 0.537 \text{ s}$ (eq. 3.2.6 NTC2018);
- $T_D = 2.128 \text{ s}$ (eq. 3.2.7 NTC2018).

The damping factor completes the parameters set that define the elastic response spectra ultimately. As it will be shown in the next section, the pressure components computation requires different design spectra for each pressure component because of their different damping properties. The spectrum definition takes into account the damping through the damping correction factor:

$$\eta = \sqrt{10/(5 + \xi)} \geq 0.55 \quad (7.1)$$

where ξ is the viscous damping ratio expressed as a percentage of critical damping. We assume the following values for the viscous damping ratio:

- $\xi_c = 0.5 \%$;
- $\xi_i = 5.0 \%$;
- $\xi_f = 2.5 \%$.

for the convective, the impulsive and the impulsive flexible component, respectively.

7.3 Dynamic response of liquid storage tanks

Seismic analysis of liquid-containing tanks requires a particular study because the fluid inside of tanks exerts hydrodynamic pressures on the tank's wall and base. Moreover, the tank structure stresses and the base shear and overturning moment depend on these pressures distributions. Several mechanical models provide the hydrodynamic pressures concerning ground supported tanks subjected to a horizontal acceleration of its base. Housner [53] derived the expressions for base shear and overturning moment on a rigid wall tank due to lateral base excitation. He replaced the fluid by an *impulsive mass*, rigidly attached to the tank container wall, and *the convective masses*, connected to the wall through springs. Veletsos and Yang [55], and Haroun [56] further obtained the distribution of hydrodynamic pressure on the rigid and flexible wall. Models involving flexible wall tanks need to consider fluid-structure interaction. Different ways to investigate fluid-structure interaction problems use the finite-element method: the added mass approach, the

Eulerian approach, the Lagrangian approach, and the Eulerian-Lagrangian approach, [70]. All these approaches, but the added mass method, requires special software that includes fluid elements or a sophisticated formulation. The added mass approach adds, to the structural mass at the fluid-structure interface, a mass obtained by different techniques. Therefore, to consider the fluid effect, the mass matrix increase, whereas stiffness and damping matrices do not change. For the calculation of flexible tanks, the Eurocode 1998-4 suggest the added-mass method. However, this method requires an iterative procedure to determine the tank and the liquid fundamental joint natural bending mode shape, necessary to compute the so-called flexible impulsive pressure. In this case study, we consider the bending shape function proposed by Cornelissen [71] avoiding the iteration method.

It is worthwhile noting that the Eurocode 1998-4 also provided a simplified method for calculating total base shear and the overturning moment. This method uses the tabulated coefficients depending on the H/R ratio lying in the interval of $0.3 \leq H/R \leq 3$. For our purposes, unfortunately, all the tanks in Table 7.1 have slenderness ratio out of the valid range of application of the proposed method.

The model we adopt takes into account hydrodynamic pressure conveniently subdivided into three components:

- the impulsive rigid pressure;
- the convective pressure;
- the impulsive flexible pressure.

In the next sections, we report the equations used in calculating the three components of hydrodynamic pressures. These equations refer to a cylindrical tank, anchored and ground supported, of radius R , height H_T , and wall thickness s . The tank is filled up with liquid to the height of H and excited horizontally by the seismic ground acceleration $a(t)$. Figure 7.2 shows the reference system in dimensionless cylindrical coordinates, ($\xi = r/R, \theta, \zeta = z/H$). According to the potential flow theory hypothesis, the fluid is incompressible and inviscid, the flow is irrotational, and all structural and liquid motions remain within the linear elastic range of response.

The vertical component of seismic action induces an axisymmetric hydrodynamic pressure distribution. This pressure distribution does not produce

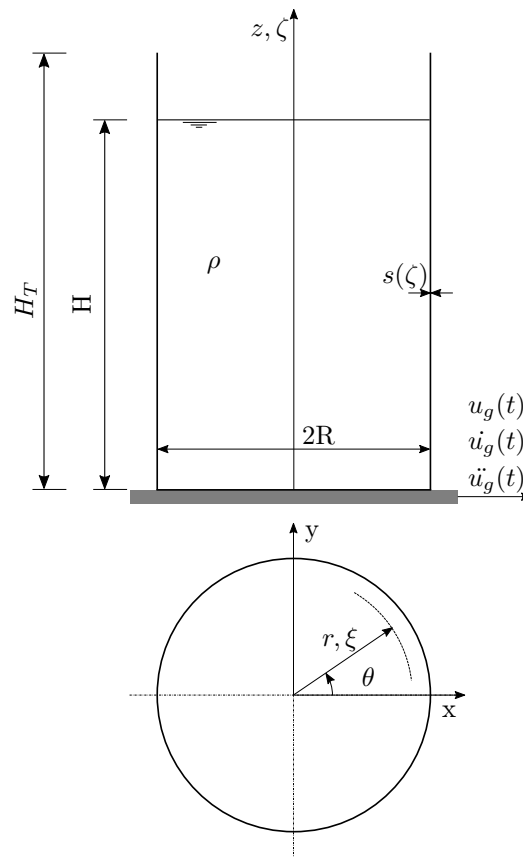


Figure 7.2: Tank reference system in cylindrical coordinates

a shear force or moment resultant at any horizontal level of the tank, or immediately above or below the base. Therefore, in the following, we neglect both the seismic action's vertical component and the hydrostatic component, because we are interested only in determining loads induced in the anchorage system.

7.3.1 Convective pressure

For the tank subjected to seismic action, the hypothesis underlying the calculation of convective pressure distribution p_k are:

- rigid walls;
- anchored tank;
- no soil-interaction;

- seismic action affects only waves generation (sloshing).

The following equation defines the convective pressure distribution:

$$p_k(\xi, \theta, \zeta, t) = \sum_{n=0}^{\infty} \frac{2 R \rho}{\lambda_n^2 - 1} \left[\frac{J_1(\lambda_n \xi)}{J_1(\lambda_n)} \right] \left[\frac{\cosh(\lambda_n \gamma \zeta)}{\cosh(\lambda_n \gamma)} \right] \cos(\theta) a_{kn}(t) \Gamma_{kn} \quad (7.2)$$

where:

- ρ is the fluid density;
- $J_1()$ is the first order Bessel function;
- $\lambda_n \forall n = 1, 2, \dots$ are the roots of the derivative of the Bessel function;
- $a_{kn}(t)$ is the horizontal response acceleration time history of the equivalent SDOF harmonic oscillator with the period T_{kn} of the n-th sloshing natural mode;

and Γ_{kn} is the participation factor of the convective pressure component corresponding to sloshing mode n ,

$$\Gamma_{kn} = \frac{2 \sinh(\lambda_n \gamma) [\cosh(\lambda_n \gamma) - 1]}{\sinh(\lambda_n \gamma) \cosh(\lambda_n \gamma) - \lambda_n \gamma} \quad (7.3)$$

The oscillations period for the n-th sloshing mode is given by:

$$T_{kn} = \frac{2\pi}{\sqrt{\frac{g \lambda_n \tanh(\lambda_n \gamma)}{R}}} \quad (7.4)$$

Generally, it is sufficient to consider only the fundamental period, and Equation 7.2 becomes:

$$p_k(\xi, \theta, \zeta, t) = R \rho C_k(\xi, \zeta, \gamma) \cos(\theta) a_{k1}(t) \Gamma_{k1} \quad (7.5)$$

where,

$$C_k(\xi, \zeta, \gamma) = \frac{2}{\lambda_1^2 - 1} \left[\frac{J_1(\lambda_1 \xi)}{J_1(\lambda_1)} \right] \left[\frac{\cosh(\lambda_1 \gamma \zeta)}{\cosh(\lambda_1 \gamma)} \right] \quad (7.6)$$

$C_k(\xi, \theta, \zeta)$ represents the normalized convective pressure component. For the case study tank ($\gamma = 4.55$), considering the pressure distribution limited to the tank shell $\xi = 1$, Figure 7.3 shows the curve of normalized convective pressure component at $\theta = 0$. The pressure from its the maximum value at the liquid level, $\zeta = 1$, drops down to 75% just at $\zeta = 0.8$. Therefore sloshing pressures influences only the upper portion of the tank walls.

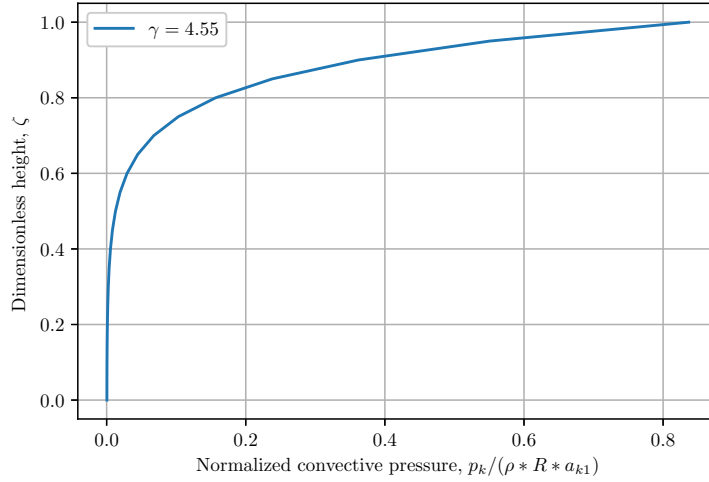


Figure 7.3: Pressure distribution of the convective component.

7.3.2 Impulsive rigid pressure

The hypothesis for computation of impulsive rigid pressures are:

- rigid walls moves together with the liquid;
- anchored tank;
- no soil-interaction;
- the sloshing mode does not occur.

The following equation defines the rigid impulsive pressure distribution:

$$p_{ir}(\xi, \theta, \zeta, t) = \sum_{n=0}^{\infty} \frac{2R\gamma\rho(-1)^n}{v_n^2} \left[\frac{I_1(v_n\xi/\gamma)}{I_1'(v_n/\gamma)} \right] \cos(v_n\zeta) \cos(\theta) a_{ir}(t) \Gamma_{ir} \quad (7.7)$$

where:

- ρ is the fluid density;
- $v_n = \frac{2n+1}{2}\pi$;
- $I_1(v_n\xi/\gamma)$ is the modified first order Bessel function;
- $I_1'(v_n/\gamma)$ is the derivative of the previous Bessel function;

- $a_{ir}(t)$ is the horizontal acceleration time history for rigid movement;
- Γ_{ir} is the participation factor for impulsive rigid pressure component, $\Gamma_{ir} = 1$.

We can write the equation 7.7 as:

$$p_{ir}(\xi, \theta, \zeta, t) = R \rho C_i(\xi, \zeta, \gamma, n) \cos(\theta) a_{ir}(t) \Gamma_{ir} \quad (7.8)$$

where:

$$C_i(\xi, \zeta, \gamma, n) = \sum_{n=0}^{\infty} \frac{\gamma (-1)^n}{v_n^2} \left[\frac{I_1(v_n \xi / \gamma)}{I_1'(v_n / \gamma)} \right] \cos(v_n \zeta) \quad (7.9)$$

$C_i(\xi, \theta, \zeta, n)$ represents the normalized rigid impulsive pressure component. As for the convective pressure, considering the pressure distribution limited to the tank shell $\xi = 1$, Figure 7.4 shows the curve of normalized rigid impulsive pressure component at $\theta = 0$.

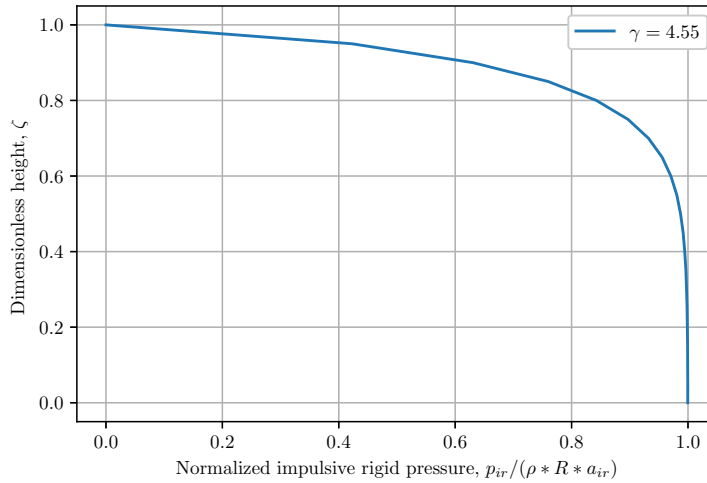


Figure 7.4: Pressure distribution of the rigid impulsive component.

7.3.3 Impulsive flexible pressure

The impulsive flexible pressure component represents the combined (joint) vibration of the deformable tank shell with the liquid. The hypothesis for the computation of this pressure are:

- flexible walls moves together with the liquid;
- anchored tank;
- no soil-interaction;
- the sloshing mode does not occur.

The impulsive flexible pressure distribution follows the equation:

$$p_{if}(\xi, \theta, \zeta, t) = \sum_{n=0}^{\infty} 2 R \rho \left[\frac{I_1(v_n \xi / \gamma)}{I_1'(v_n / \gamma)} \right] \left[\cos(v_n \zeta) \int_0^1 f(\zeta) \cos(v_n \zeta) d\zeta \right] \cos(\theta) a_{if}(t) \Gamma_{if} \quad (7.10)$$

where:

- ρ is the fluid density;
- $I_1(v_n \xi / \gamma)$ is the modified first order Bessel function;
- $I_1'(v_n / \gamma)$ is the derivative of the previous Bessel function;
- $v_n = \frac{2n+1}{2} \pi$;
- $f(\zeta)$ is the bending curve of the first joint (anti-symmetric) vibration of tank and liquid;
- $a_{if}(t)$ is the horizontal relative acceleration time history of equivalent SDOF harmonic oscillator of the joint bending vibration of tank and fluid;
- Γ_{if} is the participation factor for impulsive flexible pressure component.

Fischer and Rammerstorfer in [72] proposed the following expressions for the participation factor:

$$\Gamma_{if} = \frac{\int_0^1 \frac{p_{if}(\zeta)}{s(\zeta)} d\zeta}{\int_0^1 \frac{f(\zeta)}{s(\zeta)} p_{if}(\zeta) d\zeta} \quad \text{for variable wall thickness } s(\zeta) \quad (7.11)$$

$$\Gamma_{if} = \frac{\int_0^1 p_{if}(\zeta) d\zeta}{\int_0^1 f(\zeta) p_{if}(\zeta) d\zeta} \quad \text{for constant wall thickness } s(\zeta) \quad (7.12)$$

The equations 7.10, 7.11 and 7.12 involve the bending curve of the first joint vibration of tank and liquid, that is not known. This mode shape must be determined iteratively, Eurocode 1998-4 suggests an iterative process that uses the added mass method. As detailed in [57], first, calculating the impulsive flexible pressure, with an approximated function for the bending mode, one applies the added mass to the tank wall proportionally to the pressure distribution. The second step calculates the eigenmodes of the self density/mass modified tank. The third step re-calculates the pressure impulsive flexible pressure and a new mass distribution using the fundamental modal shape. This iterative process continues until the new bending mode shape no longer exhibits any relevant changes compared to the previous iteration step. For our purposes we adopt the bending shape function proposed by Cornelissen [71]. The author with a comprehensive parameter studies shown that the bending form of any tank can be described by using a parameterized sine wave which can be mapped correctly to the natural frequencies for all common geometric and material configurations [73]. The Cornelissen's function takes the form:

$$f(\zeta) = a \sin\left(\frac{\pi}{2}(\zeta - b)c\right) + d \quad (7.13)$$

where a, b, c, d are free parameters. In [57], Table 5.12 reports the parameters' values function of tank slenderness γ .

In the Eurocode 1998-4, the fundamental natural period $T_{if,1}$ of common vibration of tank and fluid is given by:

$$T_{if,1} = 2 F(\gamma) \sqrt{\frac{W_L}{\pi g E s(\zeta = 1/3)}} = 2 R F(\gamma) \sqrt{\frac{H \rho}{E s(\zeta = 1/3)}} \quad (7.14)$$

where:

- $W_L = \pi R^2 H \rho g$ is the total weight of the liquid mass;
- $F(\gamma) = 0.1567\gamma^2 + \gamma + 1.49$ is a statistically determined correction factor;
- E is the wall modulus of elasticity.

Concerning GFRP tanks, the vibration period for an anchored liquid filled vertical tank, EN 13121-3 in section 9.2.3 Seismic load propose a similar equation (17) as:

$$T = \sqrt{\frac{\rho h}{E_e s_{1/2}}} D \left[0.628 \left(\frac{h}{D}\right)^2 + \frac{2h}{D} + 1.49 \right] \quad (7.15)$$

where:

- $D = 2R$;
- $a_{1/2}$ is the wall thickness at $\zeta = 1/2$;
- E_e is the wall modulus of elasticity.

Since the GFRP tank wall is orthotropic, the code EN 13121 suggests for the modulus of elasticity the following equation:

$$E_e = 1.5 \sqrt{E_{\phi,b} E_x} \quad (7.16)$$

where $E_{\phi,b}$ and E_x are wall laminate's circumferential bending modulus and the axial modulus, respectively.

Equation 7.10 may be written as

$$p_{if}(\xi, \theta, \zeta, t) = R \rho C_f(\xi, \zeta, \gamma, n) \cos(\theta) a_{if}(t) \Gamma_{if} \quad (7.17)$$

where $C_f(\xi, \theta, \zeta, n)$ represents the normalized flexible impulsive pressure component and can be expressed as follows:

$$C_f(\xi, \zeta, \gamma, n) = \sum_{n=0}^{\infty} 2 R \rho \left[\frac{I_1(v_n \xi / \gamma)}{I_1'(v_n / \gamma)} \right] \left[\cos(v_n \zeta) \int_0^1 f(\zeta) \cos(v_n \zeta) d\zeta \right] \quad (7.18)$$

Considering the pressure distribution limited to the tank shell $\xi = 1$, Figure 7.5 shows the curve of normalized flexible impulsive pressure component at $\theta = 0$ and obtained with 50 summed terms. The curve of impulsive flexible pressure differs from those of the rigid impulsive and convective pressures. Furthermore, Figure 7.6 illustrates that the greater the slenderness, the greater the maximum value of the impulsive flexible pressure curve.

7.3.4 Base shear and overturning moment

Given the components of hydrodynamic pressure distribution (equation (7.5), (7.8) and (7.17)), we calculate the base shear corresponding to each component, by integration at tank shell, $\xi = 1$, over the dimensionless height and along the circumference. If p_m is the generic component we have:

$$V_m = \int_{\zeta=0}^1 2 \int_{\theta=-\pi/2}^{\pi/2} p_m(\xi = 1, \theta, \zeta, t) \cos(\theta) R d\theta H d\zeta \quad (7.19)$$

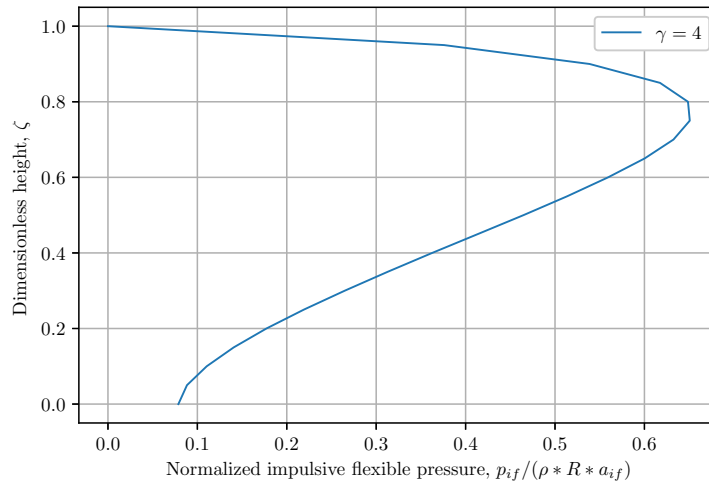


Figure 7.5: Pressure distribution of the flexible impulsive component.

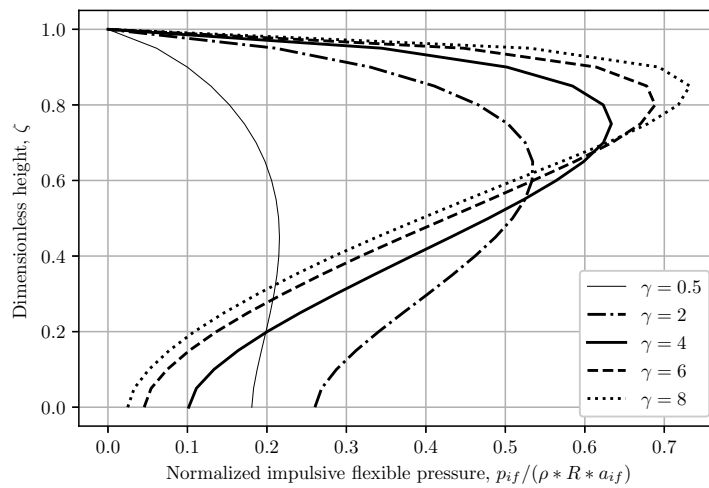


Figure 7.6: Pressure flexible impulsive component with different tank slenderness.

The overturning moment has two terms; the first originates from the horizontal pressure component multiplied by the distance from the tank base,

the second from the hydrodynamic pressures over the tank's bottom,

$$M_m = \int_{\zeta=0}^1 2 \int_{\theta=-\pi/2}^{\pi/2} H \zeta p_m(\xi = 1, \theta, \zeta, t) \cos(\theta) R d\theta H d\zeta + \int_{\xi=0}^1 2 \int_{\theta=-\pi/2}^{\pi/2} (R \xi)^2 p_m(\xi, \theta, \zeta = 0, t) \cos(\theta) R d\theta R d\xi \quad (7.20)$$

with $m = k1, ir, if$. The calculation of the integral (7.19) gives:

$$V_m = m_l \cdot a_m(t) \cdot \Gamma_m \cdot C_{m,v}^* \quad (7.21)$$

where, m_l is the total mass of the liquid. Integrating (7.20) and splitting the result into two terms, $M_{m,w}$ and $M_{m,b}$, we have:

$$M_{m,w} = \pi \cdot R^2 \cdot H^2 \cdot \rho \cdot a_m(t) \cdot \Gamma_m \cdot C_{m,w}^* \quad (7.22)$$

$$M_{m,b} = \pi \cdot R^4 \cdot \rho \cdot a_m(t) \cdot \Gamma_m \cdot C_{m,b}^* \quad (7.23)$$

7.4 Actions on the anchorage system

Given the period control values of the elastic spectrum and the viscous damping ratio (Section 7.2) the response spectrum method's application needs the fundamental natural period of each pressure component. The fundamental convective natural period (Equation 7.4) results in $T_{k1} = 2.09$ s. For the impulsive rigid pressure component, we assume the period corresponding to $T_{ir} = 0$ s. Regarding the flexible impulsive component we obtain the elastic modulus of the tank wall with Equation 7.16, that results in $E_e = 28.69$ GPa. The moduli, introduced in (7.16) are the average values of segments moduli in Table 7.2, and result equal to $E_{x,av} = 12.44$ GPa and $E_{\phi,av} = 29.40$ GPa. With this modulus we calculate the first natural period with Equation 7.14 that results in $T_{if,1} = 0.15$ s.

We assume a constant tank wall thickness as the weighted average of the thicknesses over each segment's length, obtaining $s = 18.7$ mm. Table 7.3 reports the data used to calculate the total base shear, Equation 7.21 and the overturning moment (Equations (7.22) and (7.23)). Using the SRSS rule for the superposition of the convective, rigid impulsive and flexible impulsive load components, the total base shear results in 614 kN and the overturning moment in 2285 kN m. In the computation of the loads acting on the

Table 7.3: Data used for calculate the base shear and overturning moment

Component	η (-)	T (s)	a_g (m s ⁻²)	Γ (-)	C_v^* (-)	C_w^* (-)	C_b^* (-)
Convective	1.348	2.09	1.705	2.000	0.104	0.092	0.000
Imp. Rigid	1.000	0.00	1.942	1.000	0.895	0.407	0.250
Imp. Flexib.	1.155	0.15	5.071	1.663	0.389	0.238	0.022

anchorage system, we can not consider the liquid's weight's stabilizing effect because the tank's flat bottom is not sufficiently stiff. Therefore the hold-down system should be designed for the total base moment.

The tensile action in the single anchor bolt, neglecting the self-weight of the laminated tank structure, is given by:

$$N_t = \frac{4M}{n_b D_{pc}} \quad (7.24)$$

where:

- M is the overturning moment;
- n_b is the number of anchorage bolts;
- D_{pc} is the pitch circle diameter of anchorage bolts;

and results in $N_t = 134$ kN.

7.5 The proposed solution

This section presents a first attempt of joining solution between a steel hold-down lug and a GFRP tank wall. Figure 7.7 briefly illustrates the steps of the proposed procedure. On the portion of wall tank where the adhesive will be applied, the first step, Figure 7.7(a), removes the resin's surface with the care not to exposing fibres. Secondly, Figure 7.7(b), the adhesive is spread onto the prepared surface in the first step. Third, the hold-down plate's rear surface, previously degreased, sandblasted and wipe cleaned, adhesively join the tank wall, Figure 7.7(c). Finally, Figure 7.7(d), the fibreglass overlay applies.

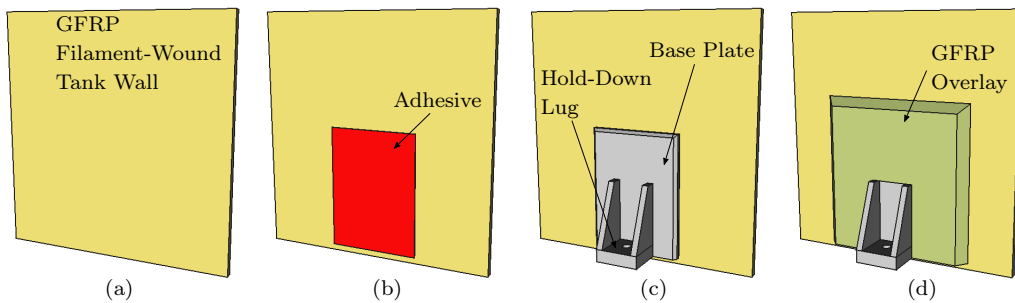


Figure 7.7: Hold-down bonding procedure, (a) Tank wall; (b) Applied adhesive; (c) Joined hold-down (d) Applied overlay.

7.5.1 Numerical analysis

Since the tank has sixteen anchorages, we performed a finite elements analysis on a simplified model of 1/16 of the tank circumference, containing one anchorage. The model geometry consists of a 0.79 m x 0.79 m x 0.023 m planar tank wall portion, appropriately constrained as specified in the following, and an adhesively bonded steel hold-down lug, covered by a composite overlay (Model A). The hold-down backplate is 0.30 m x 0.40 m x 0.15 m, the vertical gussets are 0.015 m thick, and the bottom plate is 0.10 m x 0.14 m x 0.03 m. Figure 7.8 details the geometry we meshed using Gmsh, an open-source 3D finite element mesh generator.

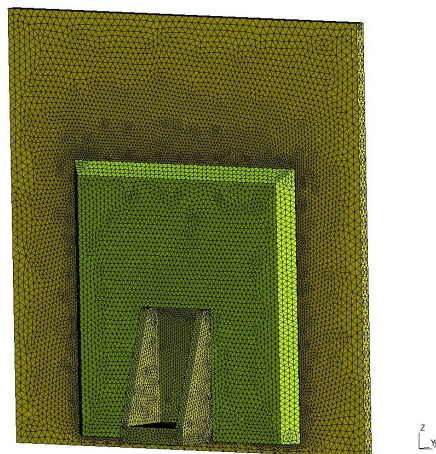


Figure 7.8: Mesh for the 3D model.

Figure 7.9 illustrates the position of the following applied boundary conditions:

- BC1, $FZ = 7.37 \times 10^6 \text{ kN m}^{-2}$;
- BC2, $DX = 0$;
- BC3, $DX = 0, DY = 0$;
- BC4, $DX = 0, DY = 0, DZ = 0$.

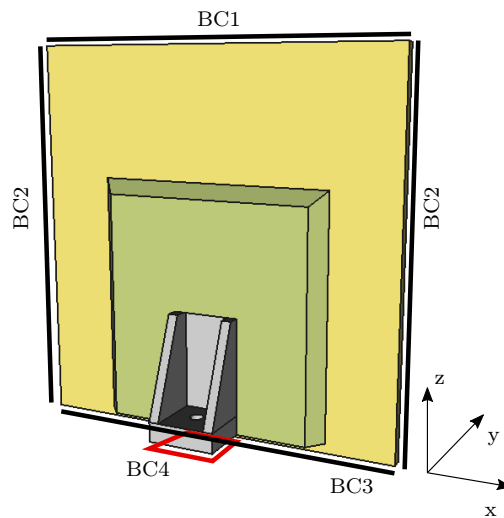


Figure 7.9: Boundary conditions applied to the fem model.

We assume for the material a linear elastic behaviour. Table 7.4 and Table 7.5 list the material parameters.

Table 7.4: Material parameters for modelling steel, adhesive ADH1 and resin.

Material	E (GPa)	ν (-)
Steel	200.00	0.30
ADH1	2.33	0.33
Resin	4.00	0.34

It is worth noting that the overlay laminate is manufactured directly onto the hold-down back plate's surface by wet hand lay-up. This process leads to a thin layer with a lower fibre fraction than in the laminate. For example, in typical marine laminates, this layer will indeed be very thin compared

Table 7.5: Material parameters for modelling GFRP as introduced in code_aster.

Elastic constant	Tank wall	Overlay
E_L (GPa)	12.483	10.529
E_T (GPa)	30.050	10.529
E_N (GPa)	12.483	10.529
G_{LT} (GPa)	6.255	3.776
G_{TN} (GPa)	3.373	3.776
G_{LN} (GPa)	3.741	3.776
ν_{LT}	0.200	0.394
ν_{TN}	0.300	0.394
ν_{LN}	0.200	0.394

to the individual plies' thickness, [74]. Therefore we applied in the model a 0.5 mm layer of pure resin between the steel and the composite overlay. Given the meshed geometry, assigned the material elastic properties and applied the boundary conditions, we performed a linear elastic analysis with the open-source software code_aster 2019 using the finite element MECA TETRA4.

To assess whether the proposed solution works or not, we focused our attention on the joint's critical components, the adhesive layer and the overlay. Regarding the adhesive layer, Spaggiari et al. in [75] proposed a simple stress-based failure criterion that uses only material properties obtainable from simple experimental tests. The aim was to provide a simple tool for an industrial designer to estimate and predict bonded joints' failure load under multiaxial stresses. The criterion states that the adhesive failure does not occur when the following inequality holds:

$$\tau^2 + A\sigma \leq \tau_{cr} \quad (7.25)$$

where:

- τ is the applied shear stress;
- σ is the applied normal stress;
- A is a parameter calculated from the experimental tests;

- τ_{cr} is the average critical failure shear stress obtained experimentally.

The parameter A was calculated as:

$$A = \frac{\tau_{cr}}{\sigma_{av}} \quad (7.26)$$

where τ_{cr} and σ_{av} are the average values of the failure shear stress and pure tensile stress, obtained experimentally on tubular specimens butt-joined using a thin film of adhesive. Spaggiari et al. validated their failure criterion by performing the tests on tubular joints for load conditions that involved pure tensile, pure shear, and six configurations of mixed loading in tension and compression. Besides, they validated the proposed criterion working on literature data from other authors. In particular, they observed a good failure prediction for the data reported in [76] where adhesive properties were provided from bulk test specimens.

In this work, the bulk adhesive tests as described in Chapter 4 are performed. Therefore the average failure values of tensile, compressive and shear stress for the selected adhesives are available (Table 4.5, Table 4.6 and Table 4.7) and, for adhesive ADH1 are summarized in Table 7.6. Using the stresses τ_{yz} , σ_{yy} gained from the finite element model over two rectilinear paths, SHD and GTW (Figure 7.10), and the parameter $A = 8.255$ MPa, the Spaggiari et al. criterion was applied.

Table 7.6: AHD1 average strength properties.

Property	Unit	Value	St.Dev
Tensile strength	MPa	16.3	0.63
Compressive strength	MPa	56.7	0.85
Shear strenght	MPa	11.6	2.20

Figure 7.11 and Figure 7.12 exhibits the equivalent stress $\tau_{eq,SPA}$ curve, normalised by the failure shear stress τ_{cr} , over the rectilinear path SHD and GTW, respectively. The curves show that the adhesive's normalised equivalent stresses, at most equal to 0.09 on the GFRP tank wall adhesive side and most equal to 0.15 on the steel hold-down lug adhesive side, are far from the critical, equal to 1.0.

In [75], the authors highlighted that the Stassi d'Alia criterion [77] also fits the experimental data of their work very well. This criterion is suitable

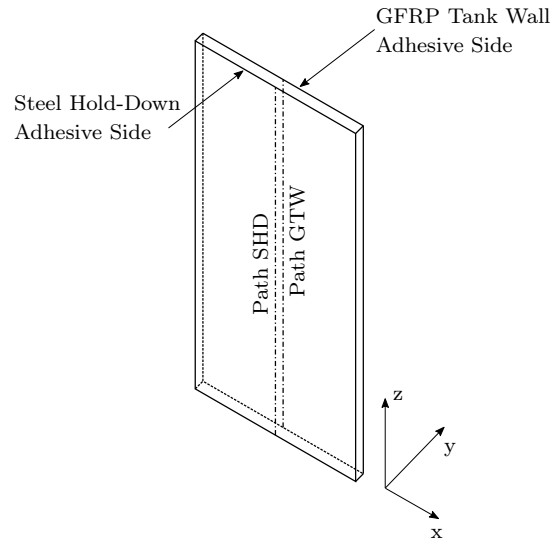


Figure 7.10: Position of paths on adhesive surfaces.

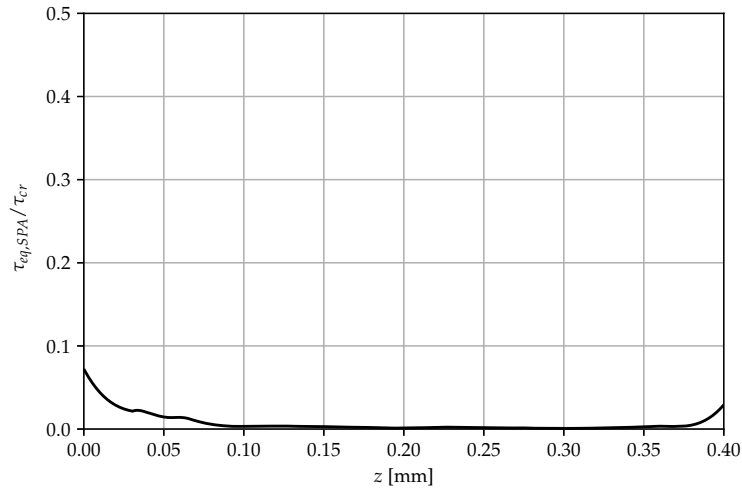


Figure 7.11: Normalised equivalent stress curve on GTW path.

for adhesives' failure prediction due to the asymmetry of tensile and compressive mechanical behaviour of polymers and can be conveniently expressed as follows:

$$\rho\sigma_{eq,SDA}^2 - 3(\rho - 1)\bar{\sigma}\sigma_{eq,SDA} - \sigma_{eq,VM}^2 = 0 \quad (7.27)$$

where:

- ρ is the ratio between the tensile and compressive yields strength of

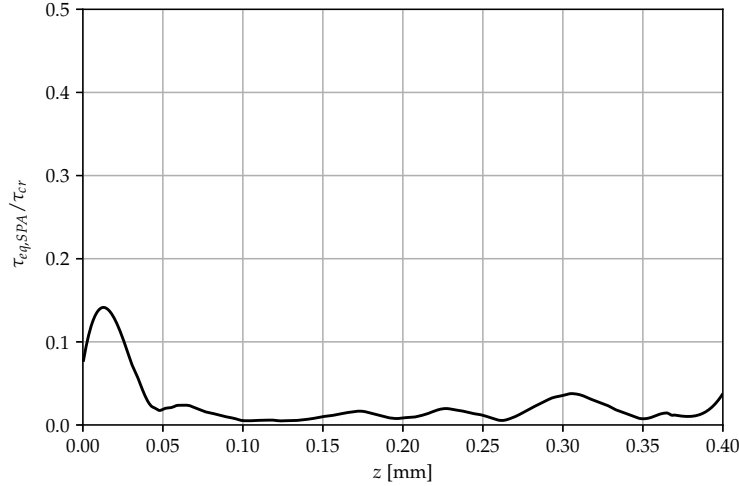


Figure 7.12: Normalised equivalent stress curve on SHD path.

material, $\rho = \sigma'_0/\sigma_0$;

- $\sigma_{eq,SDA}$ is the Stassi d'Alia equivalent stress;
- $\bar{\sigma} = (\sigma_1 + \sigma_2 + \sigma_3)/3$, (σ_1 , σ_2 and σ_3 are the principal stresses);
- $\sigma_{eq,VM}^2 = 1/2((\sigma_1 - \sigma_2)^2 + (\sigma_2 - \sigma_3)^2 + (\sigma_3 - \sigma_1)^2)$

As mentioned before, tensile and compressive strength data are available for the selected adhesives. After calculating for the adhesive AHD1 the parameter $\rho = 3.48$ MPa, the Stassi d'Alia criterion was applied to the principal stresses in the adhesive ADH1 over the rectilinear previously described path (Figure 7.10) of the finite element model. The equivalent stresses $\sigma_{eq,SDA}$ calculated point by point along with the selected paths as the roots of the Equation 7.27 are showed in Figure 7.13 and Figure 7.14. The solid blue and red curves represent the tensile and compressive strength values (critical) of the adhesive ADH1 (Table 7.6). The tensile and compressive equivalent stresses are far from those corresponding to the pure tensile or compressive strength, respectively. Therefore the adhesive used in the simplified finite element model that represents the proposed joining solution works properly.

The adhesive application's effect on the fibreglass overlay (Figure 7.7d) stress was qualitatively investigated. The von Mises equivalent stress induced

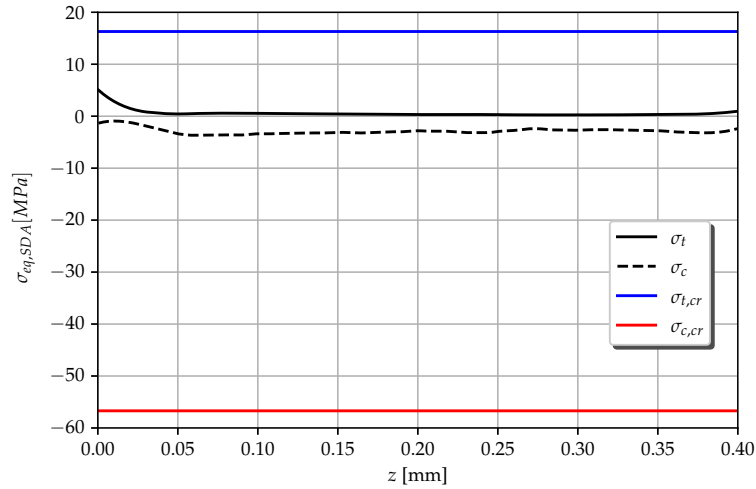


Figure 7.13: Stassi d'Alia equivalent stresses on GTW path.

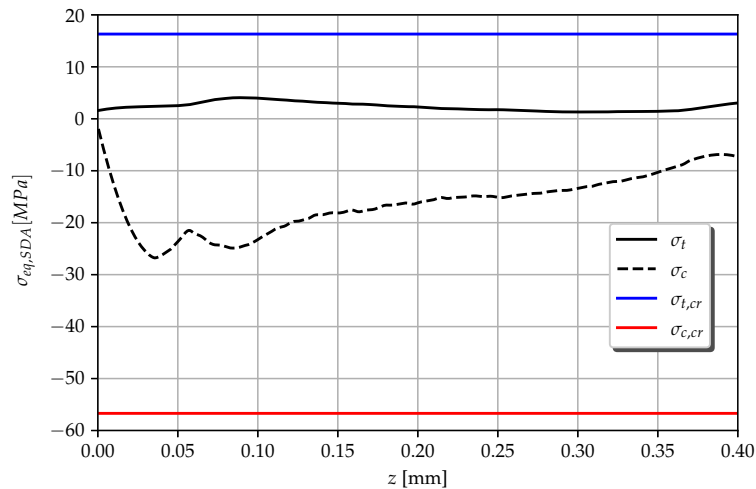


Figure 7.14: Stassi d'Alia equivalent stresses on SHD path.

in the overlay of the simplified finite element model (Model A) was compared with the equivalent stress of a further finite element model (Model B), in which the adhesive layer had an elastic module five orders of magnitude lesser than the actual value for AHD1. Figure 7.15 and Figure 7.16 highlights the positive impact on the equivalent stress distribution magnitude in the overlay when the joint applies the adhesive. The colour maps show that the

presence of the adhesive layer (Figure 7.15) leads to a maximum equivalent stress of 9.7 MPa, whereas the similar joint without the adhesive exhibits a different equivalent stress distribution that gives maximum equivalent stress of 21.3 MPa (Figure 7.16).

7.6 Conclusion

In GFRP tank anchoring, the transfer of tensile forces from different materials, the steel hold-down lug and the fibreglass tank wall, play an important role. The proposed joining technique between the steel hold-down lug and the GFRP tank wall uses an adhesive and a fibreglass overlay. For the tank investigated in the case study, a finite element analysis on a simplified model of the suggested adhesively bonded joint was performed. To estimate if the selected adhesive ADH1 supported the tensile force transfer, two failure criteria were applied to analyse the adhesive stress state. Both the criteria showed equivalent stresses less than the failure stress of the adhesive. In the overlay, the adhesive effect (Model A) leads to a different equivalent stress distribution with maximum values up to 50% less than that in the model where the adhesive effect can be neglected (Model B). The obtained results are encouraging. However, this topic needs future investigations on modelling techniques and selecting a suitable failure criterion involving the composite component to predict the joint strength. Anyway, this research could serve as a base for future studies on this joining technique.

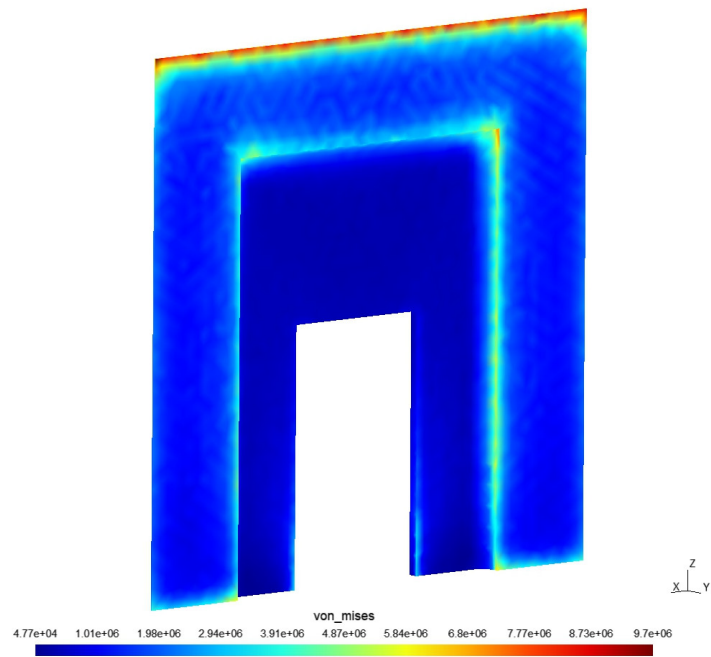


Figure 7.15: Model A - Von Mises stress values in the overlay (proposed joining technique).

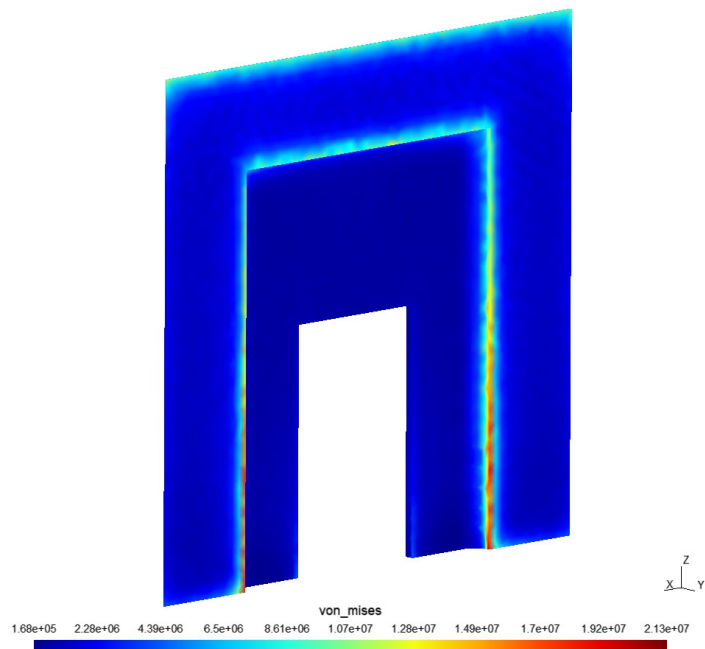


Figure 7.16: Model B - Von Mises stress values in the overlay (without the application of the adhesive).

Chapter 8

Conclusions

The study of steel - Glass Fibre-Reinforced Polymer (GFRP) bonded joints for the design of anchorage systems for flat bottom GFRP tanks, subjected to seismic actions, has involved several different topics. In the extensive literature review, we have summarized the leading references on the analysis of composite materials, adhesion and adhesives, adhesively bonded joints, and seismic analysis of liquid storage tanks.

Regarding composite materials, the knowledge of elastic constants for the single lamina and the equivalent homogenised elastic constants of the laminate is of primary importance for the preliminary design of the experimental test and to define analytical or numerical models required for interpreting the experimental results. We developed a general numerical tool for the stiffness prediction of glass-fibre reinforced polymer laminates, starting from the mechanical properties of constituents (resin and fibre). The comparison of the results obtained by this tool with the experimental outcomes showed a good agreement as it can be seen in section 3.8.

Standard test methods consider the adhesive in its *in-situ* or *thin-film* form. Therefore, the required mechanical properties for stress analysis purposes when the adhesive needs to be modelled, e.g. using the finite element method, are not provided. An approach allowing to determine these properties uses bulk adhesive tests. An experimental campaign was performed on two selected adhesives, referred to as ADH1 and ADH2, to determine their bulk mechanical properties. Adhesive ADH1, developed by the manufacturer to join GFRP pipes with GFRP fittings, has a vinyl-ester based formulation with fillers and thixotropic agents. Adhesive ADH2 is an epoxy-type adhesive designed for structural bonds. A typical application for this

product is the structural reinforcement of concrete beams by bonding carbon fibre composite plates. In particular, for the tensile and shear tests, novel techniques were proposed for specimens preparation. Shapes of specimens were 3D modelled, 3D printed using PLA filament and fixed in a plastic container. The container was then appropriately filled with silicone rubber with low shrink characteristics. After curing, silicone moulds with high dimensional accuracy, were obtained. Silicone mould prevents the adhesive from adhering to the mould surface. In this manner, no release agent was applied to the mould components' surface, avoiding any contamination of the adhesive, and no machining of specimens was required. Besides, we designed and fabricated new grips for tensile tests (Figure 4.8) and a new interestingly setup to perform shear tests (Figure 4.13). Since the shear test showed a more ductile behaviour of the adhesives than the tensile test, to further our research, we have planned to investigate if the tensile specimen manufacturing may cause this difference. Finally, we compared the elastic shear modulus, G , provided by the shear test with those calculated given the tensile modulus, E , and Poisson's ratio, ν , obtained from the tensile and compression tests (Table 4.8). For ADH1, the differences between the elastic shear modulus provided by the shear test and shear moduli estimated from tensile and compression data were of -5% and -6% , respectively. The good agreement between the two test results demonstrated that the proposed test setups provide uniform uniaxial and pure shear stress states.

At the time of writing, the joint components' mechanical characterisation, the steel and the composite laminate, was performed. Regarding the composite laminate, the hand lay-up method followed by laminate compression under the pneumatic press has led to good results. The obtained fibre mass fraction, $M_f = 0.575$ for the specimens, assessed with the loss on ignition test, was close to the typical range for filament wound laminates. Following the procedures suggested by many authors, we prepared steel-GFRP adhesively bonded double shear lap splice joints using the characterised adhesives. We deferred to future work the execution of the tests because the samples' preparation involved a great effort and delays due to Covid-19 Pandemic, and we are currently investigating which measurements to carry out to get as much data as possible from every single test.

Concerning the double shear lap splice joint, we developed a 3D finite element model (6.4). This model is characterized by a parametric geometry definition that allows, without any model manipulation, setting the joint

width, the overlap (bondline) length, the adhesive thickness, the steel plate length and thickness, the gap length and the number of unidirectional layers in the composite adherends. Furthermore, by modelling each lamina of the laminated adherend separately, we retained the laminated nature of composite that permits the calculation of stress and the application of specific failure criteria for future investigations. We performed a static load simulation of the joint prepared to be tested in the future research programme, obtaining a good agreement with the analytical solution proposed by Tsai, Oplinger and Morton [50]. Therefore the developed finite element framework offers the possibility of modelling accurately actual double shear lap splice joints and can be used to conduct parametric studies fast and reliably. It is worth noting that for meshing, finite element analysis and post-processing, we adopted open-source numerical tools alternatives to commercial packages with favourable results.

Finally, investigating a case study, we presented an original technique that uses adhesive bonding combined with the classic overlay method to join the steel hold-down lug to the GFRP tank wall. A finite element analysis on a simplified model of the suggested adhesively bonded joint was performed for the tank studied. To estimate if the selected adhesive ADH1 supported the tensile force transfer, two failure criteria were applied to analyse the adhesive stress state. Both the criteria showed equivalent stresses less than the failure stress of the adhesive. In the overlay, the adhesive effect leads to a different equivalent stress distribution with maximum values up to 50 % less than that in the model where the adhesive effect can be neglected. The obtained results are encouraging. We believe that the present research will serve as a base for future studies on the proposed joining technique, finding application in the fabrication of new GFRP tanks and rehabilitation of the existing GFRP tank structures. However, future investigations are planned on modelling techniques and selecting a suitable failure criterion involving the composite component to obtain a reliable prediction of the joint strength.

Appendix A

Appendix

Proof of Equation 3.21 in Section 3.5

Equation (3.4) defines the general constitutive equation for a linear elastic material. Assuming the material to be *hyperelastic*, Equation (3.7) holds, and the number of coefficients that characterize the material reduces to 21. Moreover, if we assume the material to be *isotropic*, the number of such coefficients can be dropped to 2: the *Lamé constants*. These constants are known as μ and λ . For an isotropic material, the elastic strain energy is:

$$w = \mu(\varepsilon_{11}^2 + \varepsilon_{22}^2 + \varepsilon_{33}^2 + 2(\gamma_{12}/2)^2 + 2(\gamma_{23}/2)^2 + 2(\gamma_{13}/2)^2) + \frac{1}{2}\lambda(\varepsilon_{11} + \varepsilon_{22} + \varepsilon_{33})^2$$

Performing the (3.6) derivatives, we can compute the components of the stress tensor:

$$\begin{aligned}\sigma_{11} &= \frac{\partial w}{\partial \varepsilon_{11}} = 2\mu\varepsilon_{11} + \lambda(\varepsilon_{11} + \varepsilon_{22} + \varepsilon_{33}) \\ \sigma_{22} &= \frac{\partial w}{\partial \varepsilon_{22}} = 2\mu\varepsilon_{22} + \lambda(\varepsilon_{11} + \varepsilon_{22} + \varepsilon_{33}) \\ \sigma_{33} &= \frac{\partial w}{\partial \varepsilon_{33}} = 2\mu\varepsilon_{33} + \lambda(\varepsilon_{11} + \varepsilon_{22} + \varepsilon_{33}) \\ \sigma_{12} &= \frac{\partial w}{\partial \gamma_{12}} = \mu\gamma_{12} \\ \sigma_{23} &= \frac{\partial w}{\partial \gamma_{23}} = \mu\gamma_{23} \\ \sigma_{13} &= \frac{\partial w}{\partial \gamma_{13}} = \mu\gamma_{13}\end{aligned}$$

The symbolic tensor notation provides a more compact expression:

$$\mathbf{T} = \mathbb{C}\mathbf{E} = 2\mu\mathbf{E} + \lambda(\text{tr}\mathbf{E})\mathbf{1} \quad (\text{A.1})$$

where:

- $\text{tr}\mathbf{E}$ is the *trace* of the strain tensor \mathbf{E} namely, $\text{tr}\mathbf{E} = \varepsilon_{ii}$;
- $\mathbf{1}$ is the unitary tensor.

Equation (A.1) can be easily inverted by performing the trace of its both sides:

$$\text{tr}\mathbf{T} = 2\mu(\text{tr}\mathbf{E}) + \lambda(\text{tr}\mathbf{E})(\text{tr}\mathbf{1}) \quad (\text{A.2})$$

from which:

$$\text{tr}\mathbf{E} = \frac{\text{tr}\mathbf{T}}{2\mu + 3\lambda} \quad (\text{A.3})$$

Substituting (A.3) in (A.1) gives the stress tensor:

$$\mathbf{T} = 2\mu\mathbf{E} + (\text{tr}\mathbf{T})\frac{\lambda}{2\mu + 3\lambda}\mathbf{1}$$

and the strain tensor:

$$\mathbf{E} = \frac{1}{2\mu}\mathbf{T} - \frac{\lambda}{2\mu(2\mu + 3\lambda)}(\text{tr}\mathbf{T})\mathbf{1}$$

If we define:

$$\frac{1 + \nu}{E} = \frac{1}{2\mu}$$

$$\frac{\nu}{E} = \frac{\lambda}{2\mu(2\mu + 3\lambda)}$$

where ν is the Poisson's ratio and E is the Young's modulus, we obtain the inverse form of the isotropic constitutive equation,

$$\mathbf{E} = \frac{1 + \nu}{E} \mathbf{T} - \frac{\nu}{E} (\text{tr} \mathbf{T}) \mathbf{1} \quad (\text{A.4})$$

that in components gives:

$$\varepsilon_{11} = \frac{1}{E} (\sigma_{11} - \nu \sigma_{22} - \nu \sigma_{33})$$

$$\varepsilon_{22} = \frac{1}{E} (\sigma_{22} - \nu \sigma_{11} - \nu \sigma_{33})$$

$$\varepsilon_{33} = \frac{1}{E} (\sigma_{33} - \nu \sigma_{11} - \nu \sigma_{22})$$

$$\gamma_{12} = \frac{\sigma_{12}}{G}$$

$$\gamma_{23} = \frac{\sigma_{23}}{G}$$

$$\gamma_{13} = \frac{\sigma_{13}}{G}$$

Finally, by the suitable combination of E and ν , we may define another additional constant of importance in engineering elasticity: the shear modulus, or modulus of rigidity G as:

$$G = \mu = \frac{E}{2(1 + \nu)} \quad (\text{A.5})$$

which, as noted, is identical to the Lamé constant μ . For isotropic elastic materials, any two elastic constants completely define the material's response. In addition to that, any elastic constant can be determined in terms of any two other constants.

Bibliography

- [1] World Health Organization. Office of Library and Health Literature Services. *Chemical releases caused by natural hazard events and disasters - information for public health authorities*. 2018.
- [2] Valeria Casson Moreno et al. “Analysis of Past Accidents Triggered by Natural Events in the Chemical and Process Industry”. In: *Chemical Engineering Transactions* 74 (May 2019), pp. 1405–1410. DOI: [10.3303/CET1974235](https://doi.org/10.3303/CET1974235). URL: <https://www.cetjournal.it/index.php/cet/article/view/CET1974235>.
- [3] EV Au, AF Walker, and WJ Lomax. “Wine industry implementation of the NZSEE guidance on the seismic design of liquid storage tanks”. In: ed. by NZSEE Annual Conference. 2015.
- [4] K Bandyopadhyay et al. “Seismic design and evaluation guidelines for the Department of Energy high-level waste storage tanks and appurtenances”. In: (Jan. 1993). DOI: [10.2172/6548045](https://doi.org/10.2172/6548045). URL: <https://www.osti.gov/biblio/6548045>.
- [5] A. Baldan. “Adhesion phenomena in bonded joints”. In: *International Journal of Adhesion and Adhesives* 38 (2012), pp. 95–116. ISSN: 0143-7496. DOI: <https://doi.org/10.1016/j.ijadhadh.2012.04.007>. URL: <http://www.sciencedirect.com/science/article/pii/S0143749612000668>.
- [6] R.M. Christensen. *Mechanics of Composite Materials*. Dover Civil and Mechanical Engineering. Dover Publications, 2012. ISBN: 9780486136660. URL: <https://books.google.it/books?id=ean0lydtVc4C>.
- [7] Ever J. Barbero. *Introduction to composite materials design*. Boca Raton, Florida London, England New York: CRC Press, 2011. ISBN: 9780429109478.

- [8] I.M. Daniel and O. Ishai. *Engineering Mechanics of Composite Materials*. Engineering mechanics of composite materials v. 13. Oxford University Press, 2006. ISBN: 9780195150971.
- [9] G.C. Eckold. “A design method for filament wound GRP vessels and pipework”. In: *Composites* 16.1 (1985), pp. 41–47. ISSN: 0010-4361. DOI: [https://doi.org/10.1016/0010-4361\(85\)90657-3](https://doi.org/10.1016/0010-4361(85)90657-3). URL: <http://www.sciencedirect.com/science/article/pii/0010436185906573>.
- [10] Leif Carlsson. *Experimental characterization of advanced composite materials*. Boca Raton, Florida: CRC Press, 2014. ISBN: 978-1-4398-4859-3.
- [11] R. Slaminko. “Strain Gages on Composites—Gage-Selection Criteria”. In: *Manual on Experimental Methods for Mechanical Testing of Composites*. Ed. by Richard L. Pendleton and Mark E. Tuttle. Dordrecht: Springer Netherlands, 1989, pp. 27–29. ISBN: 978-94-009-1129-1. DOI: [10.1007/978-94-009-1129-1_5](https://doi.org/10.1007/978-94-009-1129-1_5). URL: https://doi.org/10.1007/978-94-009-1129-1_5.
- [12] A.V. Pocius and D.A. Dillard. *Adhesion Science and Engineering: Surfaces, Chemistry and Applications*. Annals of Discrete Mathematics. Elsevier Science, 2002. ISBN: 9780080525983. URL: <https://books.google.it/books?id=QZcbSr8MW98C>.
- [13] Elena Dinte and Bianca Sylvester. “Adhesives: Applications and Recent Advances”. In: *Applied Adhesive Bonding in Science and Technology*. Ed. by Halil Özer. Rijeka: IntechOpen, 2018. Chap. 8. DOI: [10.5772/intechopen.71854](https://doi.org/10.5772/intechopen.71854). URL: <https://doi.org/10.5772/intechopen.71854>.
- [14] L.F.M. da Silva. *Modeling of Adhesively Bonded Joints*. Modeling of Adhesively Bonded Joints. Springer Berlin Heidelberg, 2008. ISBN: 9783540790563. URL: <https://books.google.it/books?id=Z48m4Fru8m0C>.
- [15] R.D. Adams and W.C. Wake. *Structural Adhesive Joints in Engineering*. Elsevier Science, 1987. ISBN: 9789401089777. DOI: [10.1007/978-94-009-5616-2](https://doi.org/10.1007/978-94-009-5616-2).
- [16] A. Baldan. “Adhesively-bonded joints and repairs in metallic alloys, polymers and composite materials: Adhesives, adhesion theories and surface pretreatment”. In: *Journal of Materials Science* 39.1 (Jan. 2004),

- pp. 1–49. ISSN: 1573-4803. DOI: [10.1023/B:JMSE.0000007726.58758.e4](https://doi.org/10.1023/B:JMSE.0000007726.58758.e4). URL: <https://doi.org/10.1023/B:JMSE.0000007726.58758.e4>.
- [17] A. J. Kinloch. *Adhesion and Adhesives : Science and Technology*. Dordrecht: Springer Netherlands, 1987. ISBN: 978-90-481-4003-9.
- [18] M. D. Banea and L. F. M. da Silva. “Adhesively bonded joints in composite materials: An overview”. In: *Proceedings of the Institution of Mechanical Engineers, Part L: Journal of Materials: Design and Applications* 223.1 (2009), pp. 1–18. DOI: [10.1243/14644207JMDA219](https://doi.org/10.1243/14644207JMDA219). eprint: <https://doi.org/10.1243/14644207JMDA219>. URL: <https://doi.org/10.1243/14644207JMDA219>.
- [19] Xiacong He. “A review of finite element analysis of adhesively bonded joints”. In: *International Journal of Adhesion and Adhesives - INT J ADHES ADHES* 31 (June 2011), pp. 248–264. DOI: [10.1016/j.ijadhadh.2011.01.006](https://doi.org/10.1016/j.ijadhadh.2011.01.006).
- [20] J. G. Teng et al. *FRP: Strengthened RC Structures*. Wiley, 2002. ISBN: 9780471487067. URL: <https://books.google.it/books?id=PNFRAAAAMAJ>.
- [21] Huy Binh Pham and Riadh Saleh Hassan Al-Mahaidi. “Modelling of CFRP-concrete shear-lap tests”. English. In: *Construction and Building Materials* 21.4 (2007), pp. 727–735. ISSN: 0950-0618.
- [22] J. F. Chen and J. G. Teng. “Anchorage Strength Models for FRP and Steel Plates Bonded to Concrete”. In: *Journal of Structural Engineering* 127.7 (2001), pp. 784–791. DOI: [10.1061/\(ASCE\)0733-9445\(2001\)127:7\(784\)](https://doi.org/10.1061/(ASCE)0733-9445(2001)127:7(784)). eprint: <https://ascelibrary.org/doi/pdf/10.1061/%28ASCE%290733-9445%282001%29127%3A7%28784%29>. URL: <https://ascelibrary.org/doi/abs/10.1061/%28ASCE%290733-9445%282001%29127%3A7%28784%29>.
- [23] Ramin Rameshni, Stefano Arcovio, and Mark Green. “Experimental and numerical study of adhesively bonded glass fibre-reinforced polymer - to-steel double-shear lap splices”. In: *Canadian Journal of Civil Engineering* 40 (Nov. 2013). DOI: [10.1139/cjce-2012-0508](https://doi.org/10.1139/cjce-2012-0508).
- [24] Xiao Ling Zhao and Lei Zhang. “State-of-the-art review on FRP strengthened steel structures”. English. In: *Engineering Structures* 29.8 (2007), pp. 1808–1823. ISSN: 0141-0296.

- [25] J.Q. Yang, Scott T. Smith, and Peng Feng. “Effect of FRP-to-steel bonded joint configuration on interfacial stresses: Finite element investigation”. English. In: *Thin-Walled Structures* 62.Complete (2013), pp. 215–228. DOI: [10.1016/j.tws.2012.07.020](https://doi.org/10.1016/j.tws.2012.07.020).
- [26] Xinran (Sharon) Xiao, Peter.H. Foss, and Jessica.A. Schroeder. “Stiffness prediction of the double lap shear joint. Part1: Analytical solution”. In: *International Journal of Adhesion and Adhesives* 24.3 (2004), pp. 229–237. ISSN: 0143-7496. DOI: <https://doi.org/10.1016/j.ijadhadh.2003.10.003>. URL: <http://www.sciencedirect.com/science/article/pii/S0143749603001428>.
- [27] Xinran (Sharon) Xiao, Peter H. Foss, and Jessica A. Schroeder. “Stiffness prediction of the double lap shear joint. Part 2: Finite element modeling”. In: *International Journal of Adhesion and Adhesives* 24.3 (2004), pp. 239–246. ISSN: 0143-7496. DOI: <https://doi.org/10.1016/j.ijadhadh.2003.10.004>. URL: <http://www.sciencedirect.com/science/article/pii/S014374960300143X>.
- [28] David R. Speth, Yu Ping Yang, and George W. Ritter. “Qualification of adhesives for marine composite-to-steel applications”. In: *International Journal of Adhesion and Adhesives* 30.2 (2010), pp. 55–62. ISSN: 0143-7496. DOI: <https://doi.org/10.1016/j.ijadhadh.2009.08.004>. URL: <http://www.sciencedirect.com/science/article/pii/S0143749609000815>.
- [29] Alaa Al-Mosawe, Riadh Al-Mahaidi, and Xiao-Ling Zhao. “Effect of CFRP properties, on the bond characteristics between steel and CFRP laminate under quasi-static loading”. In: *Construction and Building Materials* 98 (2015), pp. 489–501. ISSN: 0950-0618. DOI: <https://doi.org/10.1016/j.conbuildmat.2015.08.130>. URL: <http://www.sciencedirect.com/science/article/pii/S0950061815303470>.
- [30] Karim Osouli-Bostanabad, Abolfazl Tutunchi, and Mehdi Eskandarzade. “The influence of pre-bond surface treatment over the reliability of steel epoxy/glass composites bonded joints”. In: *International Journal of Adhesion and Adhesives* 75 (2017), pp. 145–154. ISSN: 0143-7496. DOI: <https://doi.org/10.1016/j.ijadhadh.2017.03.006>. URL: <http://www.sciencedirect.com/science/article/pii/S0143749617300568>.

- [31] S. Budhe et al. “An updated review of adhesively bonded joints in composite materials”. In: *International Journal of Adhesion and Adhesives* 72 (2017), pp. 30–42. ISSN: 0143-7496. DOI: <https://doi.org/10.1016/j.ijadhadh.2016.10.010>. URL: <http://www.sciencedirect.com/science/article/pii/S0143749616302068>.
- [32] L C Hollaway and J Cadei. “Progress in the technique of upgrading metallic structures with advanced polymer composites”. In: *Progress in Structural Engineering and Materials* 4.2 (2002), pp. 131–148. DOI: [10.1002/pse.112](https://doi.org/10.1002/pse.112). eprint: <https://onlinelibrary.wiley.com/doi/pdf/10.1002/pse.112>. URL: <https://onlinelibrary.wiley.com/doi/abs/10.1002/pse.112>.
- [33] H. Jiao and X.-L. Zhao. “CFRP strengthened butt-welded very high strength (VHS) circular steel tubes”. In: *Thin-Walled Structures* 42.7 (2004), pp. 963–978. ISSN: 0263-8231. DOI: <https://doi.org/10.1016/j.tws.2004.03.003>. URL: <http://www.sciencedirect.com/science/article/pii/S0263823104000485>.
- [34] Shaohua Xia and J.G. Teng. “Behaviour of FRP-to-steel bonded joints”. In: *Proceedings of the International Symposium on Bond Behaviour of FRP in Structures*. Jan. 2005.
- [35] Lucas F. M. da Silva et al. “Effect of Adhesive Type and Thickness on the Lap Shear Strength”. In: *The Journal of Adhesion* 82.11 (2006), pp. 1091–1115. DOI: [10.1080/00218460600948511](https://doi.org/10.1080/00218460600948511). eprint: <https://doi.org/10.1080/00218460600948511>. URL: <https://doi.org/10.1080/00218460600948511>.
- [36] S. Fawzia et al. “Strengthening of circular hollow steel tubular sections using high modulus CFRP sheets”. In: *Construction and Building Materials* 21.4 (2007). Composites in Civil Engineering, pp. 839–845. ISSN: 0950-0618. DOI: <https://doi.org/10.1016/j.conbuildmat.2006.06.014>. URL: <http://www.sciencedirect.com/science/article/pii/S0950061806001255>.
- [37] J.D. Melograna and J.L. Grenestedt. “Adhesion of stainless steel to fiber reinforced vinyl ester composite”. In: 24 (Oct. 2002), pp. 254–260.

- [38] Kai Wei et al. “Strength and Failure Mechanism of Composite-Steel Adhesive Bond Single Lap Joints”. In: *Advances in Materials Science and Engineering* 2018 (Mar. 2018). ISSN: 1687-8434. DOI: [10.1155/2018/5810180](https://doi.org/10.1155/2018/5810180). URL: <https://doi.org/10.1155/2018/5810180>.
- [39] Maged Youssef, Mostafa Abushagur, and Ashraf El Damatty. “Experimental and Analytical Investigation of Steel Beams Rehabilitated Using GFRP Sheets”. In: *Steel and Composite Structures* 3 (Dec. 2003), pp. 421–438. DOI: [10.12989/scs.2003.3.6.421](https://doi.org/10.12989/scs.2003.3.6.421).
- [40] A. A. El Damatty, M. Abushagur, and M. A. Youssef. “Rehabilitation of Composite Steel Bridges Using GFRP Plates”. In: *Applied Composite Materials* 12.5 (Sept. 2005), pp. 309–325. ISSN: 1573-4897. DOI: [10.1007/s10443-005-2730-x](https://doi.org/10.1007/s10443-005-2730-x). URL: <https://doi.org/10.1007/s10443-005-2730-x>.
- [41] Abdelaziz A. Taib et al. “Bonded joints with composite adherends. Part I. Effect of specimen configuration, adhesive thickness, spew fillet and adherend stiffness on fracture”. In: *International Journal of Adhesion and Adhesives* 26.4 (2006), pp. 226–236. ISSN: 0143-7496. DOI: <https://doi.org/10.1016/j.ijadhadh.2005.03.015>. URL: <http://www.sciencedirect.com/science/article/pii/S0143749605000539>.
- [42] J. M. C Cadei et al. *Strengthening metallic structures using externally bonded fibre-reinforced polymers*. English. CIRIA. CIRIA, 2004. ISBN: 9780860175957.
- [43] Till Vallée, João R. Correia, and Thomas Keller. “Probabilistic strength prediction for double lap joints composed of pultruded GFRP profiles part I: Experimental and numerical investigations”. In: *Composites Science and Technology* 66.13 (2006), pp. 1903–1914. ISSN: 0266-3538. DOI: <https://doi.org/10.1016/j.compscitech.2006.04.007>. URL: <http://www.sciencedirect.com/science/article/pii/S0266353806001333>.
- [44] T. Yu et al. “Experimental study on CFRP-to-steel bonded interfaces”. In: *Composites Part B: Engineering* 43.5 (2012), pp. 2279–2289. ISSN: 1359-8368. DOI: <https://doi.org/10.1016/j.compositesb.2012.01.024>. URL: <http://www.sciencedirect.com/science/article/pii/S1359836812000303>.

- [45] S Sugiman et al. “Effect of adhesive thickness on the strength of steel-composite joints aged in wet environment”. In: *IOP Conference Series: Materials Science and Engineering* 532 (June 2019), p. 012007. DOI: [10.1088/1757-899x/532/1/012007](https://doi.org/10.1088/1757-899x/532/1/012007). URL: <https://doi.org/10.1088/1757-899x/532/1/012007>.
- [46] Volkersen O. “Die Niekraftverteilung in Zugbeanspruchten mit Konstanten Laschenquerschnitten”. In: *Luftfahrtforschung* 15 (1938), pp. 41–47.
- [47] *Strength Prediction of Adhesively-Bonded Joints*. CRC PRESS, 2017. ISBN: 9780367782412. DOI: <https://doi.org/10.1201/9781315370835>.
- [48] Lucas F.M. da Silva et al. “Analytical models of adhesively bonded joints-Part I: Literature survey”. In: *International Journal of Adhesion and Adhesives* 29.3 (2009), pp. 319–330. ISSN: 0143-7496. DOI: <https://doi.org/10.1016/j.ijadhadh.2008.06.005>. URL: <http://www.sciencedirect.com/science/article/pii/S0143749608000730>.
- [49] Lucas F.M. da Silva et al. “Analytical models of adhesively bonded joints-Part II: Comparative study”. In: *International Journal of Adhesion and Adhesives* 29.3 (2009), pp. 331–341. ISSN: 0143-7496. DOI: <https://doi.org/10.1016/j.ijadhadh.2008.06.007>. URL: <http://www.sciencedirect.com/science/article/pii/S0143749608000742>.
- [50] M.Y. Tsai, D.W. Oplinger, and J. Morton. “Improved theoretical solutions for adhesive lap joints”. In: *International Journal of Solids and Structures* 35.12 (1998), pp. 1163–1185. ISSN: 0020-7683. DOI: [https://doi.org/10.1016/S0020-7683\(97\)00097-8](https://doi.org/10.1016/S0020-7683(97)00097-8). URL: <http://www.sciencedirect.com/science/article/pii/S0020768397000978>.
- [51] M.Y. Tsai and J. Morton. “An investigation into the stresses in double-lap adhesive joints with laminated composite adherends”. In: *International Journal of Solids and Structures* 47.24 (2010), pp. 3317–3325. ISSN: 0020-7683. DOI: <https://doi.org/10.1016/j.ijsolstr.2010.08.011>. URL: <http://www.sciencedirect.com/science/article/pii/S0020768310002908>.
- [52] Xu Jiang et al. “Analysis on Adhesively-Bonded Joints of FRP-steel Composite Bridge under Combined Loading: Arcan Test Study and Numerical Modeling”. In: *Polymers* 8 (Jan. 2016), p. 18. DOI: [10.3390/polym8010018](https://doi.org/10.3390/polym8010018).

- [53] George W. Housner. “Dynamic pressure on accelerated fluid container”. In: *Bulletin of the Seismological Society of America* (1957), pp. 15–35.
- [54] Maria Vathi and Spyros Karamanos. “Liquid Storage Tanks: Seismic Analysis”. In: Jan. 2014, pp. 1–27. ISBN: 978-3-642-36197-5. DOI: [10.1007/978-3-642-36197-5_144-1](https://doi.org/10.1007/978-3-642-36197-5_144-1).
- [55] Yang JY Veletsos AS. “Earthquake response of liquid storage tanks”. In: ed. by 2nd engineering mechanics conference. 1977.
- [56] Medhat A. Haroun. “Vibration studies and tests of liquid storage tanks”. In: *Earthquake Engineering & Structural Dynamics* 11.2 (1983), pp. 179–206.
- [57] Konstantin Meskouris et al. *Structural Dynamics with Applications in Earthquake and Wind Engineering*. Jan. 2019. ISBN: 978-3-662-57548-2.
- [58] Andreas Kandelbauer et al. “6 - Unsaturated Polyesters and Vinyl Esters”. In: *Handbook of Thermoset Plastics (Third Edition)*. Ed. by Hanna Dodiuk and Sidney H. Goodman. Third Edition. Boston: William Andrew Publishing, 2014, pp. 111–172. ISBN: 978-1-4557-3107-7.
- [59] S. T. Peters. *Composite filament winding*. Materials Park, Ohio: ASM International, 2011. ISBN: 978-1-61503-722-3.
- [60] Quanjin Ma et al. “Filament winding technique, experiment and simulation analysis on tubular structure”. In: *IOP Conference Series: Materials Science and Engineering* 342 (Apr. 2018), p. 012029. DOI: [10.1088/1757-899X/342/1/012029](https://doi.org/10.1088/1757-899X/342/1/012029).
- [61] I.S. Sokolnikoff and R.D. Specht. *Mathematical Theory of Elasticity*. McGraw-Hill, 1946.
- [62] Mark Lutz. *Learning Python*. Sebastopol, CA: O’Reilly, 2013. ISBN: 978-1-449-35573-9.
- [63] P. Maćkowiak, D. Płaczek, and M. Kotyk. “Determination of design mechanical properties of adhesives in a tensile and compression test”. In: *IOP Conference Series: Materials Science and Engineering* 393 (Aug. 2018), pp. 012–027. DOI: [10.1088/1757-899x/393/1/012027](https://doi.org/10.1088/1757-899x/393/1/012027). URL: <https://doi.org/10.1088/1757-899x/393/1/012027>.

- [64] B. Duncan G. Dean. *Measurement Good Practice Guide No.17; Preparation and Testing of Bulk Specimens of Adhesives*. Tech. rep. Teddington, Middlesex, UK: National Physical Laboratory, July 1998, p. 32.
- [65] I. De Baere, W. Van Paepegem, and J. Degrieck Fdyn. “Design of a modified three-rail shear test for shear fatigue of composites”. In: *Polymer Testing* 27.3 (2008), pp. 346–359. ISSN: 0142-9418. DOI: <https://doi.org/10.1016/j.polymeresting.2007.12.006>. URL: <http://www.sciencedirect.com/science/article/pii/S0142941807001869>.
- [66] I. De Baere, W. Van Paepegem, and J. Degrieck. “Comparison of the modified three-rail shear test and the $[(+45^\circ, -45^\circ)]_{ns}$ tensile test for pure shear fatigue loading of carbon fabric thermoplastics”. In: *Fatigue & Fracture of Engineering Materials & Structures* 31.6 (2008), pp. 414–427. DOI: <https://doi.org/10.1111/j.1460-2695.2008.01231.x>. URL: <https://onlinelibrary.wiley.com/doi/abs/10.1111/j.1460-2695.2008.01231.x>.
- [67] S.M. Mohseni Shakib and S. Li. “Modified three rail shear fixture (ASTM D 4255/D 4255M) and an experimental study of nonlinear in-plane shear behaviour of FRC”. In: *Composites Science and Technology* 69.11 (2009). Experimental Techniques and Design in Composite Materials (ETDCM8) with Regular Papers, pp. 1854–1866. ISSN: 0266-3538. DOI: <https://doi.org/10.1016/j.compscitech.2009.04.003>. URL: <http://www.sciencedirect.com/science/article/pii/S0266353809001365>.
- [68] Electricité de France. *Finite element code_aster, Analysis of Structures and Thermomechanics for Studies and Research*. Open source on www.code-aster.org. 1989–2020.
- [69] Christophe Geuzaine and Jean-François Remacle. “Gmsh: A 3-D finite element mesh generator with built-in pre- and post-processing facilities”. In: *International Journal for Numerical Methods in Engineering* 79.11 (2009), pp. 1309–1331. DOI: <https://doi.org/10.1002/nme.2579>. eprint: <https://onlinelibrary.wiley.com/doi/pdf/10.1002/nme.2579>. URL: <https://onlinelibrary.wiley.com/doi/abs/10.1002/nme.2579>.

- [70] R. Livaoglu and A. Dogangun. “Simplified seismic analysis procedures for elevated tanks considering fluid-structure-soil interaction”. In: *Journal of Fluids and Structures* 22.3 (2006), pp. 421–439. ISSN: 0889-9746. DOI: <https://doi.org/10.1016/j.jfluidstructs.2005.12.004>.
- [71] P. Cornelissen. “Erarbeitung eines vereinfachten impulsiv-flexiblen Lastansatzes für die Berechnung von Tankbauwerken unter Erdbebenlast”. Diplomarbeit. RWTH Aachen, 2010.
- [72] D. F. Fischer and F. G. Rammerstorfer. “The Stability of Liquid-Filled Cylindrical Shells Under Dynamic Loading”. In: *Buckling of Shells*. Ed. by E. Ramm. Berlin, Heidelberg: Springer Berlin Heidelberg, 1982, pp. 569–597. ISBN: 978-3-642-49334-8.
- [73] K. Meskouris et al. In: ed. by Archaeology International Workshop on Active Tectonics Earthquake Geology and Greece Engineering Corinth. 2011.
- [74] Harald Osnes and Dag McGeorge. “Analysis of overlaminated double-lap joints”. In: *Composites Part B: Engineering* 36.6 (2005), pp. 544–558. ISSN: 1359-8368. DOI: <https://doi.org/10.1016/j.compositesb.2005.01.002>. URL: <http://www.sciencedirect.com/science/article/pii/S1359836805000168>.
- [75] A. Spaggiari, D. Castagnetti, and E. Dragoni. “A design oriented multi-axial stress-based criterion for the strength assessment of adhesive layers”. In: *Composites Part B: Engineering* 157 (2019), pp. 66–75. ISSN: 1359-8368. DOI: <https://doi.org/10.1016/j.compositesb.2018.08.085>. URL: <https://www.sciencedirect.com/science/article/pii/S1359836818316767>.
- [76] Dimitrios Zarouchas and Rogier Nijssen. “Mechanical behaviour of thick structural adhesives in wind turbine blades under multi-axial loading”. In: *Journal of Adhesion Science and Technology* 30.13 (2016), pp. 1413–1429. DOI: [10.1080/01694243.2016.1146392](https://doi.org/10.1080/01694243.2016.1146392). URL: <https://doi.org/10.1080/01694243.2016.1146392>.
- [77] Ferdinando Stassi-D’Alia. “Flow and fracture of materials according to a new limiting condition of yielding”. In: *Meccanica* 2.3 (Sept. 1967), pp. 178–195. ISSN: 1572-9648. DOI: [10.1007/BF02128173](https://doi.org/10.1007/BF02128173). URL: <https://doi.org/10.1007/BF02128173>.